Characterization of single-mode laser and tunable laser array based on etched high order surface gratings

Thesis

By

Azat Abdullayev

A thesis submitted to the *University of Dublin*

for the degree of

Doctor of Philosophy

School of Physics,

University of Dublin,

Trinity College Dublin.

February 2015

Declaration

This thesis has not been submitted as an exercise for a degree in this or any other university. The work described in this thesis is entirely my own, with exception of assistance recognized in the acknowledgements and the collaborative work noted in the publications. I agree that Trinity College library may lend or copy this thesis on request.

Azat Abdullayev

Summary

Wavelength tunable single-mode semiconductor lasers play an essential role in modern optical communication systems. They are also rapidly replacing fixed-wavelength light sources in dense wavelength-division-multiplexing (DWDM) systems, which will significantly reduce the system size and cost. The optical communication industry demands light sources with relatively small volume, low inventory cost and high manufacturing yield process. Therefore, laser diodes along with high power, stable operation and narrow linewidth should have simple fabrication process and high yield.

Up to now conventional distributed feedback (DFB) and distributed Bragg reflector (DBR) lasers achieved great success in terms of stable operation, high power and wide tuning range. However, these lasers require complex fabrication steps and high resolution processing by using e-beam lithography which is time consuming and an expensive process. Previously it was demonstrated that single-mode operation can be achieved in Fabry-Perot lasers by introducing reflective defects (slots) at particular locations along the cavity. But in these lasers it is extremely hard to integrate them with other photonic components in one chip due to cleavage of both facets. This work presents cost effective and integrable a new single-mode laser design. These lasers based on etched high order gratings (slots) on one side of the laser cavity to provide enough reflection for lasing to occur. Therefore, no regrowth is needed. This work describes the slotted single-mode laser platform from design to fabrication to experimental characterization.

The thesis is organized as follows:

First, a brief explanation of WDM and coherent communications is introduced. Here it is explained what requirements laser diodes should meet in these communication systems. The theoretical part consists of the basics of laser characterization, the theory of the laser linewidth and different types of wavelength tuning mechanisms. To realize single-mode laser a grating structure is needed. To understand the theory of the gratings a brief illustration of the scattering matrix method (SMM) and the transmission matrix method (TMM) is described. Also the working principle of DBR laser and DFB laser is presented, and how single-mode operation is achieved in those lasers.

Theoretical and experimental characterizations of a FP laser were carried out by amplified spontaneous emission (ASE) using Fourier series expansion (FSE) method. From

this method different parameters are extracted to characterize the basic FP laser including a waveguide loss.

Further, the concept of slotted single-mode laser is developed. It is demonstrated that the single-mode operation can be achieved by etching high order surface gratings on top of the ridge of the laser without any regrowth of additional material. These gratings or slots can be can be done by standard photolithography. The integration of these lasers with an semiconductor amplifier (SOA) and an electro-absorption (EA) modulator is also presented. Fabricated devices exhibit a threshold current of around 30 mA and slope efficiency of around 0.12 mW/mA. The laser performance is improved by applying high reflection and antireflection coatings so the threshold current decreased to 19 mA and the slope efficiency increased to 0.17 mW/mA. The spectral characteristics show stable single-mode operation with side-mode suppression ratio (SMSR) around 50 dB. The linewidth is measured using the delayed self-heterodyne (DS-H) method. The laser linewidth is measured to be around 2-4 MHz for short cavity lasers and the linewidth follows the theoretical 1/P trend. It is also demonstrated that longer lasers exhibit a narrower linewidth and for a laser with an effective cavity length of 450 μm the minimum intrinsic linewidth is estimated to be 720 kHz.

The concept of the slotted single-mode laser is developed further by making wavelength tunable slotted single-mode laser array. First, a 10-channel slotted laser array is presented with channel spacing of 400 GHz. All lasers in the array have a threshold current between 19 and 21 mA. The wavelength tuning of 31 nm is achieved with SMSR more than 35 dB for all channels. To extend the tuning range and improve the SMSR, a 12-channel slotted laser array with non-periodically spaced slots is developed. The tuning range extended to 37 nm which covers the full C-band. The SMSR for all channels increased up to 50 dB. The typical linewidth for all lasers in the array is estimated to be around 2-4 MHz as for single-mode lasers. The linewidth is improved by making the cavity length longer. For 1 mm laser, the linewidth for all channels is less than 500 kHz. Finally, the thermal properties of slotted lasers are presented. The thermal crosstalk effect is investigated along with the thermal impedance of slotted lasers. This laser platform has strong potential for applications in optical communications systems in the future.

Acknowledgements

First, I would like to thank my supervisor Prof. John Donegan for his excellent supervision and for all his help during my PhD. I would like to express my sincere appreciation and thanks to John for all his advices, guidance and support all these years. I'm very grateful for the opportunity to work under this project in semiconductor photonics group here in Trinity College Dublin.

I would like to express my special thanks to Dr. Qiaoyin Lu for all her help in the lab and in theoretical model of this work. I appreciate her advices and never ending support. It would be really hard to work on this project without her help. Thank you.

Special thanks to my colleague and friend Marta Nawrocka for help in the lab and discussions. I'm really thankful that we worked on this project together. I also would like to thank Dr. Frank Bello for discussions in theoretical modeling of the linewidth and for his advices. Thanks also to Michael for helping with the measurements in the lab and analyzing the results. Thanks to Ian for help in the thermal measurements. Thanks to guys in the office Vas, Xia, Graham, John, Sam and thanks to the rest of the photonics group here in Trinity College for help and encouragement during my PhD.

I would especially like to thank the former members of photonics group. First of all, thanks to Dr. Wei-Hua Guo who actually started working on the concept of slotted lasers. Thanks, to Mick Lynch and Vincent Weldon. Many thanks to my friends from the office Rob, Ciaran, Ed, Diarmuid and Pablo. Lads thank you very much for your help and advice in the beginning of my PhD and thanks for creating a warm and fun atmosphere in the office and in the lab.

Also, I would like to thank my friends from Kazakhstan Oral, Olzat, Askar and Ozhet with whom I arrived to Ireland four years ago and started doing PhD here in Trinity. Thank you guys for your encouragement and assistance.

Special thanks to my dear friend Saken who introduced us to Ireland and encouraged us to study here. Thanks also to Prof. Igor Shevts who came to Kazakhstan and introduced Trinity College and who also invited us here. Without both of you probably I would miss the opportunity of coming here.

Also I would like to thank our governmental scholarship "Bolashak" for the opportunity to study abroad. Thanks for the members of JSC "CIP" for their financial support and also many thanks to the former president of "CIP" Sayasat Nurbek for his help and advices.

Finally, I would like to express a great thanks to my family. Thanks to my sisters Lyazzat, Zhannat and my brother Bolat for their love and support. And of course many thanks to my parents Ergebai and Salima for their huge love, care and emotional support. Thank you for believing in me and inspiring me all the time.

List of publications and presentations

Papers

[1] Q. Lu, W. H. Guo, M. Nawrocka, A. Abdullaev, C. Daunt, J. O'Callaghan, M. Lynch, V. Weldon, F. Peters, and J. F. Donegan, "Single mode lasers based on slots suitable for photonic integration," *Optics express* Vol. 19, no. 26, pp. B140-B145, 2011.

[2] W. H. Guo, Q. Lu, M. Nawrocka, A. Abdullaev, J. O'Callaghan, M. Lynch, V. Weldon, and J. F. Donegan, "Integrable slotted single-mode lasers," *Photonics Technology Letters, IEEE,* Vol. 24, no. 8, pp. 634-636, 2012.

[3] Q. Lu, W. H. Guo , A. Abdullaev , M. Nawrocka, T. N. Huynh, J. O'Callaghan, M. Lynch, V. Weldon, L. P. Barry, and J. F. Donegan, "Two-section singlemode lasers based on slots suitable for photonic integration," *Electronics Letters*, Vol. 48, no. 15, pp. 945-946, 2012.

[4] W. H. Guo, Q. Lu, M. Nawrocka, A. Abdullaev, J. O'Callaghan, and J. F. Donegan, "Nine-channel wavelength tunable single mode laser array based on slots," *Optics express,* Vol. 21, no. 8, pp. 10215-10221, 2013.

[5] Q. Lu, A. Abdullaev, M. Nawrocka, W. H. Guo, J. O'Callaghan, and J. F. Donegan, "Slotted single mode lasers integrated with a semiconductor optical amplifier," *IEEE Photonics Technology Letters,* Vol. 25, no. 6, pp. 564-567, 2013.

[6] M. Nawrocka, Q. Lu, W. H. Guo, A. Abdullaev, F. Bello, J. O'Callaghan, T. Cathcart, and J. F. Donegan, "Widely tunable six-section semiconductor laser based on etched slots," *Optics Express,* Vol. 22, no. 16, pp. 18949-18957, 2014.

[7] F. Bello, Q. Lu, A. Abdullaev, M. Nawrocka, and J. F. Donegan, "Linewidth and noise characterization for a partially-slotted, single mode laser," *IEEE Journal of Quantum Electronics*, vol. 50, no. 9, pp. 755-759, 2014.

[8] A. Abdullaev, Q. Lu, W. H. Guo, M. Nawrocka, F. Bello, J. O'Callaghan, and J. F. Donegan, "Linewidth characterization of integrable slotted single mode lasers," *IEEE Photonics Technology letters*, 2014.

Conference presentations:

[1] Q. Lu, W. H. Guo, M. Nawrocka, A. Abdullaev, M. Lynch, V. Weldon, and J. F. Donegan, "Slotted single-mode lasers for monolithic photonic integration." *European Conference and Exposition on Optical Communications,* pp. We-10. Optical Society of America, 2011.

[2] Q. Lu, W. H. Guo, A. Abdullaev, M. Nawrocka, J. O'Callaghan, M. Lynch, V. Weldon, and J. F. Donegan, "Integrable single mode lasers based on slots," *Semiconductor Laser Conference (ISLC), 2012 23rd IEEE International*, pp. 102-103. IEEE, 2012.

[3] Q. Lu, W. H. Guo, A. Abdullaev, M. Nawrocka, J. O'Callaghan, M. Lynch, V. Weldon, and John F. Donegan. "High-yield two-section single mode lasers based on a 37^{th} order surface grating," *CLEO: Science and Innovations*, pp. CTu3N-4. Optical Society of America, 2012.

[4] Q. Lu, W. H. Guo, A. Abdullaev, M. Nawrocka, J. O'Callaghan, M. Lynch, V. Weldon, and J. F. Donegan, "Tunable single mode laser array based on slots," *Optical Fiber Communication Conference*, pp. OTh3I-5. Optical Society of America, 2013.

[5] F. Bello, Q. Lu, A. Abdullaev, M. Nawrocka, and J. F. Donegan, "Linewidth and threshold calculations for a slotted, Fabry-Perot semiconductor laser," *Numerical Simulation of Optoelectronic Devices (NUSOD), 2013 13th International Conference on*, pp. 93-94. IEEE, 2013.

[6] A. Abdullaev, Q. Lu, M. Nawrocka, F. Bello, W. H. Guo, J. O' Callaghan, and J. F. Donegan, "Improved performance of slotted single-mode lasers," *Lasers and Electro-Optics Europe (CLEO EUROPE/IQEC), 2013 Conference on and International Quantum Electronics Conference*, pp. 1-1. IEEE, 2013.

[7] A. Abdullaev, Q. Lu, W. H. Guo, M. Nawrocka, F. Bello, J. O'Callaghan, and J. F. Donegan, "Linewidth characterization of slotted single-mode lasers," *Photonics Ireland 2013,* Belfast, 2013.

[8] Q. Lu, W. H. Guo, A. Abdullaev, M. Nawrocka, J. O'Callaghan, and J. F. Donegan, "31 nm Quasi-continuous tuning single mode laser array based on slots," *CLEO: Applications and Technology*, pp. JW2A-77. Optical Society of America, 2014.

Table of Contents

Abbreviations

ASE	Amplified spontaneous emission
AR	Anti-reflection
CW	Continuous wave
CWDM	Coarse wavelength division multiplexing
DS-H	Delayed self-heterodyne
DBR	Distributed Bragg reflector
DFB	Distributed feedback
DWDM	Dense wavelength division multiplexing
EA	Electro absorption
ECL	External cavity laser
ESA	Electrical spectral analyzer
FP	Fabry-Perot
FSE	Fourier series expansion
FSR	Free spectral range
FWHM	Full width at half maximum
HR	High reflection
ICP	Inductively coupled plasma
ITU-T	International Telecommunication Union
MMI	Multimode interference
ODMUX	Optical demultiplexer
OMUX	Optical multiplexer
OSA	Optical spectrum analyzer
PECVD	Plasma enhanced chemical vapor deposition

PSK	Phase shift keying
QAM	Quadrature amplitude modulation
QPSK	Quadrature phase shift keying
QSCE	Quantum confined Stark effect
SG-DBR	Sampled grating distributed Bragg reflector
SMM	Scattering matrix method
SMSR	Side mode suppression ratio
SOA	Semiconductor optical amplifier
SSG-DBR	Super structure grating distributed Bragg reflector
TEC	Thermo-electrical cooler
TMM	Transmission matrix method
VCSEL	Vertical-cavity surface-emitting laser
WDM	Wavelength division multiplexing

Chapter 1 – Introduction

The research and development in optical fiber communication systems started in 1970s after the groundbreaking discovery in fiber-optics by Charles Kao [1] who is known as the "father of fiber optic communications". Before this breakthrough, glass fiber were not considered as a good transmitter for light due to large signal loss from the light scattering at defects in the glass. Kao realized that, by carefully purifying the glass, it is possible to transmit the information over long distances with low loss via fibers. Accidentally, light was used in communications in earlier days. In ancient times, reflected sunlight was used as a part of communication network in the era of Darius the Great in 500 BC. In the 19th and early 20th century, an optical telegraph or a heliograph was invented where visual signal transmission was used. In 1880 Alexander Bell invented the photophone which allowed transmitting speech via a beam of light. Interest in optical communications has rapidly increased after the invention of the laser in 1960s. Now optical fiber communications is the main technology in transmitting the data, voice and video information in short-distance and long-haul communications. The demand in the transmission capacity is growing strongly year by year.

The introduction of wavelength-division multiplexing (WDM) systems in 1990s has significantly increased the information capacity, in which multiple signals (channels) are transmitted through the same fiber. In WDM systems light sources of different wavelengths are used, and the signal is modulated by an intensity modulator. The overall system is shown in Fig. 1.1. The modulated signals are mixed into the optical fiber and sent to an optical multiplexer (OMUX). Then the received signal is demultiplexed (ODMUX) and separated into different wavelengths. The separated wavelengths are then directed to corresponding detectors.

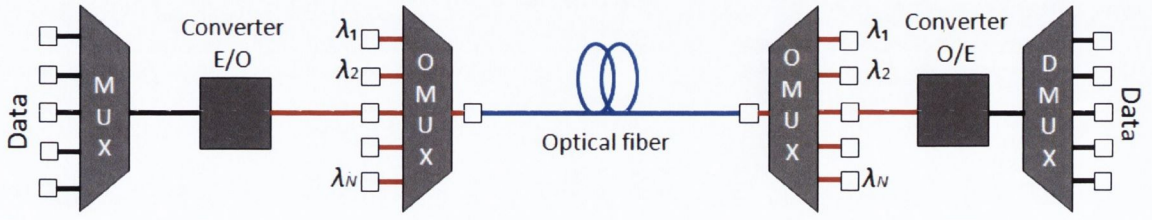

Fig. 1.1 WDM schematic.

The WDM systems are divided into two categories: Coarse WDM and Dense WDM. Coarse WDM (CDWM) systems use only a few channels with widely spaced wavelengths. The typical wavelength spacing is about 20 nm and more. CWDM is usually used in cable television networks and in metropolitan networks. Dense WDM (DWDM) systems in contrast, use a large number of channels with closely spaced wavelengths. The wavelength spacing is around 1.6 nm and below, which corresponds to 200 GHz channel spacing. Modern DWDM systems have a much closer spacing of 50 GHz which makes them high level communication systems, therefore, they are used as the basis of the Internet.

Early DWDM systems used fixed-wavelength laser diodes, which created lots of transceivers in the system. This wasn't reliable in terms of size and inventory cost. With the introduction of tunable lasers, it has been possible to reduce the inventory cost and reduce the size of the systems. The main requirements for tunable lasers are stable operation and exact wavelength emission recommended by ITU-T standards [2]. These standardized wavelengths are shown in Table. 1.1.

Frequency (THz)	Center wavelength (nm)		Frequency (THz)	Center wavelength (nm)		Frequency (THz)	Center wavelength (nm)
195.9	1530.33		194.5	1541.35		193.1	1552.52
195.8	1531.12		194.4	1542.14		193.0	1553.33
195.7	1531.90		194.3	1542.94		192.9	1554.13
195.6	1532.68		194.2	1543.73		192.8	1554.94
195.5	1533.47		194.1	1544.53		192.7	1555.75
195.4	1534.25		194.0	1545.32		192.6	1556.55
195.3	1535.04		193.9	1546.12		192.5	1557.36
195.2	1535.82		193.8	1546.92		192.4	1558.17
195.1	1536.61		193.7	1547.72		192.3	1558.98
195.0	1537.40		193.6	1548.51		192.2	1559.79
194.9	1538.19		193.5	1549.32		192.1	1560.61
194.8	1538.98		193.4	1550.12		192.0	1561.42
194.7	1539.77		193.3	1550.92		192.9	1562.23
194.6	1540.56		193.2	1551.72		192.8	1563.05

Table 1.1 DWDM wavelengths according to ITU-T standards [2].

The fastest data rate per channel in modern communication systems is 40 Gbit/s and the next generation will be 100 Gbit/s. Current deployed optical communication systems use on-off keying (OOK) detection or direct detection techniques. The future detection techniques are expected to be advanced modulation techniques, where phase and

frequency modulations are used instead of intensity modulation. Thereby, these communication systems are called coherent communication systems.

The main advantages of coherent communications is the high signal sensitivity, in other words signals with very low intensities can be detected. In theory, only a few photons are required to detect a one bit signal. This can be done by using heterodyne detection as shown in Fig. 1.2. The transmitted signal is mixed with a coherent reference signal (local oscillator) using an optical directional coupler. Then the mixed signal is detected by a photodetector and it will contain information about the amplitude and the phase of the signal. The main requirements for light sources are single-mode operation and low phase noise fluctuations.

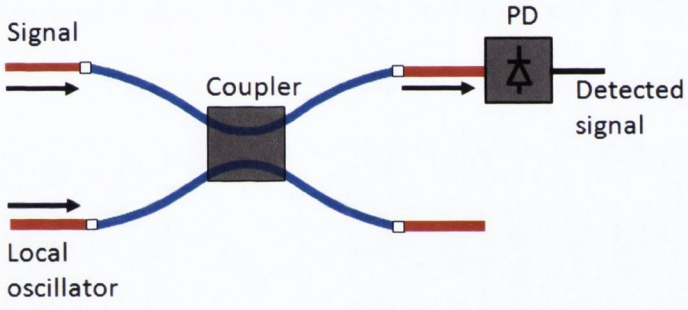

Fig. 1.2 Schematic diagram of optical heterodyne detection [3].

In coherent communications, the signal is modulated by amplitude, phase and frequency changes. The most widely used technique is phase modulation or phase shift keying (PSK) modulation where the phase of the light is used as information. Therefore, the phase noise of a light source is critical which means that the spectral linewidth of a light source should be narrow. Table 1.2 shows the laser linewidth requirements for various types of modulation techniques for 40 Gbit/s link [4]. The linewidth should be below 500 kHz for coherent communications.

Modulation format	Linewidth per laser at 40Gbit/s
QPSK	10MHz
8PSK	1.6MHz
16PSK	240kHz
Star 16QAM	1.6MHz
Square 16QAM	120kHz
Square 64QAM	1.2kHz

Table 1.2 Linewidth requirements for different modulation formats for 40 Gbit/s link [4].

By taking into account the specifications and requirements described above, the basic requirements for a laser source in WDM and coherent communications can be summarized as follows:

- High output power, so the signal can be detected.
- Modulation speed should be high.
- Narrow linewidth to prevent chromatic dispersion in the fibers and to minimize phase noise.
- Stable operation without mode hopping.
- Feasibility, simple fabrication and low cost.

The last requirements always have been important ones. Telecommunication companies and system makers seek a tunable laser than can work in any desirable wavelength range and with low inventory cost.

Table 1.3 shows the chronological development of tunable laser diodes over the past 20 years. Here, the most widely used lasers such as distributed Bragg reflector (DBR) and distributed feedback (DFB) lasers are considered. Also, the so-called slotted lasers developed in our group are included in the list.

The first wavelength tunable DBR laser was demonstrated by Tohmori and Suematsu, *et al*, [5] in 1983. They demonstrated a monolithic integration of the laser part with a phase tuning section using Butt-joint coupling. The continuous tuning of 0.4 nm was achieved. 10 years later Tohmori and Yoshikuni, *et al.* have modified the grating structure and demonstrated a super-structure grating (SSG) DBR laser [6], where the structure is based on linearly chirped gratings. Such gratings provide high reflection and a wide tuning range

which is over 100 nm including multimode regions [6]. Quasi-continuous tuning of the SSG-DBR laser was demonstrated by Ishii *et al,* with the tuning range of 34 nm [7].

In the same year with the first demonstration of the SSG-DBR laser, Jayaraman *et al.* from Coldren's group first proposed the sampled grating DBR (SG-DBR) laser where conventional gratings are divided into several interrupted grating sections [8]. A tuning range of 57 nm with SMSR more than 30 dB was achieved in these lasers. Later on, the tuning range and the mode stability were improved exhibiting high SMSR more than 45 dB and the linewidth below 5 MHz [9]. Typical linewidth of the SSG-DBR and SG-DBR lasers is more than 10 MHz. However, the group from Agilent Communications has demonstrated an SG-DBR laser integrated with EA modulator with a narrow spectral linewidth of 2 MHz over the tuning range of 40 nm and modulation speed of 2.5 Gbit/s [10]. Recently, the group from University of California, Santa Barbara (UCSB) showed a linewidth reduction in the tunable SG-DBR laser using a frequency lock technique [11]. The linewidth of the laser was improved by a factor of 27.

The wavelength tunability of DFB lasers were developed at the same time with DBR lasers. A continuous tuning of 2 nm was obtained in 1986 [12]. In 1995, a 6-channel DFB laser array was demonstrated in [13]. Later the group from NEC [14], presented an 8-channel DFB laser array combined with multi-mode interference (MMI) coupler. They successfully demonstrated the wavelength coverage over the entire S, C and L bands. Similar work was carried out by researchers from NTT [15], [16], [17] and Furukawa [18]. These groups demonstrated 12-channel DFB laser arrays with a tuning range of more than 40 nm and ultra-narrow linewidth below 200 kHz for all channels [19], [20].

The lasers presented above are based on low order gratings (with grating pitch of about~200 nm), which means that high-resolution techniques are needed to define them such as electron beam lithography which is an expensive and slow process. Also, lasers such as phase-shifted DFB lasers need an additional two or more epitaxial growth steps. These requirements will lead to high manufacturing cost. To overcome this problem, it has been proposed to etch high order gratings (slots) on top of the laser ridge so no re-growth is needed. It has been shown that by carefully positioning these slots along the ridge, it is possible to obtain a tunable laser [21], [22]. These types of lasers were developed in our group [21], [23]. Recently, we have demonstrated a slotted tunable laser with a wide tuning range of 55 nm with SMSR more than 30 dB [23].

Author	Year	λ_{tune}, (nm)	P, (mW)	SMSR, (dB)	$\Delta\nu$, (MHz)	Type of laser	Institution
Tohmori [6]	1993	50-100	-	>35	-	SSG-DBR	NTT
Jayaraman [8]	1993	57		>35	-	SG-DBR	UCSB
Young [13]	1995	-	3	>30	-	6 channel DFB laser array	AT&T Bell Labs
Ishii [7]	1996	34	>10	>35	>10	SSG-DBR	NTT
Mason [24]	2000	>50	2-6	>35	>10	SG-DBR	Agility Com.
Kudo [25]	2000	15.3	>6.9	>40	-	8 channel DFB laser array	NEC
Oohashi [26]	2001	46.9	>20	>40	-	16 channel DFB laser array	NTT
Hatakeyama [14]	2003	>15	>20	>42	-	8 channel DFB laser array	NEC
Coldren [9]	2004	>50	>20	>45	~5	SG-DBR	UCSB
Ishii [15]	2005	>27nm	>30	>45	-	8 channel DFB laser array	NTT
Ishii [16]	2007	38	40	>45	<6	12 channel DFB laser array	NTT
Ishii [17]	2009	~40	~40	>50	0.58	12 channel DFB laser array	NTT
Horikawa [18]	2009	~35	~40	>40	2-4	12 channel DFB laser array	Furukawa
Byrne [21]	2009	>30	>30	>35	>10	Slotted tunable laser	Trinity College Dublin
Ishii [19]	2010	>40	~40	>50	<0.16	12 channel DFB laser array	NTT
Yu [22]	2012	~38	>10	>40	-	Slotted tunable laser	Zhejiang University
Kimoto [20]	2013	~35	~40	>40	<0.21	12 channel DFB laser array	Furukawa
Nawrocka [23]	2014	~55	-	>30	>10	Slotted tunable laser	Trinity College Dublin
Guo [27]	2013	~27	>37	>50	2-4	9 channel slotted laser array	Trinity College Dublin
Lu, Abdullaev [28]	2014	~31	>35	>40	2-4	10 channel slotted laser array	Trinity College Dublin
Abdullaev	2014	~36	>35	>50	~0.4	12 channel slotted laser array	Trinity College Dublin

Table 1.3 Chronological development of different types wavelength tunable laser diodes.

In the past four years the concept of slotted single-mode laser has been developed and experimentally demonstrated [29], [30] in our group. The main idea is to develop the lasers with similar specifications as commercial devices, but with a simpler fabrication process and high yield. By taking into account these requirements, it was proposed to form a tunable laser array based on slotted single-mode lasers suitable for WDM and coherent communications systems. The last three works in Table 1.3 are considered to be one of the main results of this thesis.

References

[1] K. C. Kao and G. A. Hockham, "Dielectric fiber surface waveguide for optical frequency," *Proceeding of IEEE,* vol. 113, no. 7, pp. 1151-1154, 1966.

[2] ITU-T, "G.692: Optical interfaces for multichannel systems with optical amplifiers," 10 1998. [Online]. Available: http://www.itu.int/rec/T-REC-G.692-199810-I/en. [Accessed 04 02 1999].

[3] B. E. Saleh and M. C. Teich, Fundamentals of photonics, Hoboken, New Jersey: John Wiles & Sons, Inc., 2007.

[4] M. Seimetz, "Laser linewidth limitations for optical systems with high-order modulation employing feed forward digital carrier phase estimation," in *Optical Fiber communication/National Fiber Optic Engineers Conference*, San Diego, CA, 2008.

[5] Y. Tohmori, Y. Suematsu, H. Tsushima and S. Arai, "Wavelength tuning of GaInAsP/InP integrated laser with butt-jointed built-in distributed Bragg reflector," *Electronics Letters,* vol. 19, no. 17, pp. 656-657, 1983.

[6] Y. Tohmori, Y. Yoshikuni, H. Ishii, F. Kano, T. Tamamura, Y. Kondo and M. Yamamoto, "Broad-range wavelength-tunable superstructure grating (SSG) DBR lasers," *IEEE Journal of Quantum Electronics,* vol. 29, no. 6, pp. 1817-1823, 1993.

[7] H. Ishii, H. Tanobe, F. Kano, Y. Tohmori, Y. Kondo and Y. Yoshikuni, "Quasicontinuous wavelength tuning in super-structure-grating (SSG) DBR lasers," *IEEE Journal of Quantum Electronics,* vol. 32, no. 3, pp. 433-441, 1996.

[8] V. Jayaraman, A. Mathur, L. A. Coldren and P. D. Dapkus, "Theory, design, and performance of extended tuning range in sampled grating DBR lasers," *IEEE Journal of Quantum Electronics,* vol. 29, no. 6, pp. 1824-1834, 1993.

[9] L. A. Coldren, G. A. Fish, Y. Akulova, J. S. Barton, L. Johansson and C. W. Coldren, "Tunable semiconductor lasers: a tutorial," *Journal of Lightwave Technology* , vol. 22, no. 1, pp. 193-202, 2004.

[10] Y. A. Akulova, G. A. Fish, P. C. Koh, C. L. Schow, P. Kozodoy, A. P. Dahl, S. Nakagawa, M. C. Larson, M. P. Mack, T. A. Strand, C. W. Coldren, E. Hegblom, S. K. Penniman, T. Wipiejewski and L. A. Coldren, "Widely tunable electroabsorption-modulated sampled-grating DBR laser transmitter," *IEEE Journal of Selected Topics in Quantum Electronics,* vol. 8, no. 6, pp. 1349-

1357, 2002.

[11] A. Sivananthan, H. C. Park, M. Lu, J. S. Parker, E. Bloch, L. A. Johansson, M. J. Rodwell and L. A. Coldren, "Monolithic linewidth narrowing of a tunable SG-DBR laser," in *Optics Fiber Communication Conference* , Anaheim, CA, 2013.

[12] Y. Yoshikuni, K. Oe, G. Motosugi and T. Matsuoka, "Broad wavelength tuning under single-mode oscillation with a multielectrode distributed feedback laser," *Electronics Letters,* vol. 22, no. 22, pp. 1153-1154, 1986.

[13] M. G. Young, U. Koren, B. I. Miller, M. Chien, T. L. Koch, D. M. Tennant, K. Feder, K. Dreyer and G. Raybon, "Six wavelength laser array with integrated amplifier and modulator," *Electronics Letters,* vol. 31, no. 21, pp. 1835-1836, 1995.

[14] H. Hatakeyama, K. Naniwae, K. Kudo, N. Suzuki, S. Sudo, S. Ae, Y. Muroya, K. Yashiki, K. Satoh, T. Morimoto, K. Mori and T. Sasaki, "Wavelength-selectable microarray light sources for S-, C-, and L-Band WDM systems," *IEEE Photonics Technology Letters* , vol. 15, no. 7, pp. 903-905, 2003.

[15] H. Ishii, H. Oohashi, K. Kasaya, K. Tsuzuki and Y. Tohmori, "High-power (40mW) L-band tunable DFB laser array module using current tuning," in *Optic Fiber Communication Conference*, Anaheim, CA, 2005.

[16] H. Ishii, K. Kasaya, H. Oohashi, Y. Shibata, H. Yasaka and K. Okamoto, "Widely wavelength tunable DFB laser array integrated with funnel combiner," *IEEE Journal of Selected Topics in Quantum Electronics,* vol. 13, no. 5, pp. 1089-1094, 2007.

[17] H. Ishii, K. Kasaya and H. Oohashi, "Spectral linewidth reduction in widely wavelength tunable DFB laser array," *IEEE Journal of Selected Topics in Quantum Electronics,* vol. 15, no. 3, pp. 514-520, 2009.

[18] K. Horikawa, A. Yamomoto, T. Osada, H. Koshi, Y. Yafuso and T. Kurobe, "Development of ITLA using a full-band tunable laser," *Furukawa Review,* vol. 35, 2009.

[19] H. Ishii, K. Kasaya and H. Oohashi, "Narrow spectral linewidth operation (<160kHz) in widely tunable distributed feedback laser array," *Electronics Letters,* vol. 46, no. 10, pp. 714-715, 2010.

[20] T. Kimoto, G. Kobayashi, T. Kurobe, T. Mukaihara and S. Ralph, "Narrow linewidth tunable DFB laser array for PDM-16QAM transmission," in *OptoElectronics and Communications Conference* , Kyoto, 2013.

[21] D. Byrne, J. P. Engelstaedter, W. H. Guo, Q. Lu, B. Corbett, B. Roycroft, J. O'Callaghan, F. H. Peters and J. F. Donegan, "Discretely tunable semiconductor lasers suitable for photonic integration," *IEEE Journal of Selected Topics in Quantum Electronics,* vol. 15, no. 3, pp. 482-487, 2009.

[22] T. Yu, L. Zou, L. Wang and J. J. He, "Single-mode and wavelength tunable lasers based on deep-submicron slots fabricated by standard UV-lithography," *Optics Express,* vol. 20, no. 15, pp. 16291-16298, 2012.

[23] M. Nawrocka, Q. Lu, W. H. Guo, A. Abdullaev, F. Bello, J. O'Callaghan, T. Catchcart and J. F. Donegan, "Widely tunable six-section semiconductor laser based on etched slots," *Optics*

Express, vol. 22, no. 16, pp. 18949-18957, 2014.

[24] B. Mason, J. Barton, G. A. Fish, L. A. Coldren and S. P. Denbaars, "Design of sampled grating DBR lasers with integrated semiconudctor optical amplifiers," *IEEE Photonics Technology Letters* , vol. 12, no. 7, pp. 762-764, 2000.

[25] K. Kudo, K. Yashiki, T. Sasaki, Y. Yokoyama, K. Hamamoto, T. Morimoto and M. Yamaguchi, "1.55-μm wavelength-selectable microarray DFB-LDs with monolithically integrated MMI combiner, SOA, and EA modulator," *IEEE Photonics Technology Letters,* vol. 12, no. 3, pp. 242-244, 2000.

[26] H. Oohashi, Y. Shibata, H. Ishii, Y. Kawaguchi, Y. Kondo, Y. Yoshikuni and Y. Tohmori, "46.9nm Wavelength-selectable arrayed DFB lasers with integrated MMI coupler and SOA," in *International Conference on Induim Phosphide and Related Materials*, Nara, Japan, 2001.

[27] W. H. Guo, Q. Lu, M. Nawrocka, A. Abdullaev, J. O'Callaghan and J. F. Donegan, "Nine-channel wavelength tunable single mode laser array based on slots," *Optics Express,* vol. 21, no. 8, pp. 10215-10221, 2013.

[28] Q. Lu, W. H. Guo, A. Abdullaev, M. Nawrocka, J. O'Callaghan and J. F. Donegan, "31nm Quasi-continuous tuning single mode laser array based on slots," in *CLEO*, San Jose, CA, 2014.

[29] Q. Lu, W. H. Guo, D. Byrne and J. F. Donegan, "Design of slotted single-mode lasers suitable for photonic integration," *IEEE Photonics Technology Letters,* vol. 22, no. 11, pp. 787-789, 2010.

[30] W. H. Guo, Q. Lu, M. Nawrocka, A. Abdullaev, J. O'Callaghan, M. Lynch, V. Weldon and J. F. Donegan, "Integrable slotted single-mode lasers," *IEEE Photonics Technology Letters,* vol. 24, no. 8, pp. 634-636, 2012.

Chapter 2 – Semiconductor lasers

The first effort in the development of lasers was achieved by Albert Einstein in 1917 [1] when he introduced the concept of stimulated emission. However, it took about 40 years before stimulated emission has been demonstrated at microwave frequencies. In 1958, Schawlow and Townes presented the concept of an optical maser [2]. A few years later, the first laser, the ruby laser, was demonstrated by Maiman [3] in 1960. The first semiconductor laser was realized simultaneously and separately by Hall [4], Quist [5], and Nathan [6]. These lasers were homo-junction systems based on GaAs material. In the same year, Holonyak [7] demonstrated the first visible laser diode on a GaP substrate. In 1960s, the laser was considered as a "solution looking for a problem". But today, lasers have found a variety of applications in many fields including medicine, optical fiber communications, data storage, printers, sensors, metrology, atomic clocks, optical information processing and many others. The significance of lasers have been increasing since their invention and they keep opening up new areas of applications [8]. In 2010, the 50^{th} anniversary of the laser was celebrated and the laser was acknowledged as a milestone invention of the mid-20^{th} century in the same group as the transistor and the computer.

2.1. Fundamentals of laser diodes

Semiconductor lasers have unique properties such as compact size, high efficiency, high speed direct modulation, long lifetime, low power consumption and low loss. Therefore, these devices are the key components in photonics, particularly in optical communications. In this chapter we will give the basic concepts of semiconductor laser operation. We will introduce optical gain in semiconductors, heterostructures, spectral characteristics, the linewidth and tunability.

2.1.1. Spontaneous and stimulated emissions

Fig. 2.1 shows the basic types of radiative transition. The solid circles are the electrons and the open circles are the holes. The first transition is a spontaneous recombination where an electron-hole pair recombines spontaneously to emit a photon. The emitted photon has a random phase and direction. If the number of such emissions will be large, then it will result in incoherent emission. An example of a device working on spontaneous emission is the light emitting diode (LED) where photon feedback is not provided. The second transition is the stimulated carrier generation. In this transition the electron is initially in the lower energy level and the photon absorption will excite the electron to the higher level in the conduction band (E_c) while leaving the hole in the valence band (E_v). The third transition is the stimulated emission. Here an incident photon excites the system to produce electron-hole recombination and at the same time a new photon is generated. The generated photon has the same phase, frequency and direction as the incident photon. Therefore, a large number of such processes will result in coherent emission. This process underlies the operation of laser diodes and laser amplifiers.

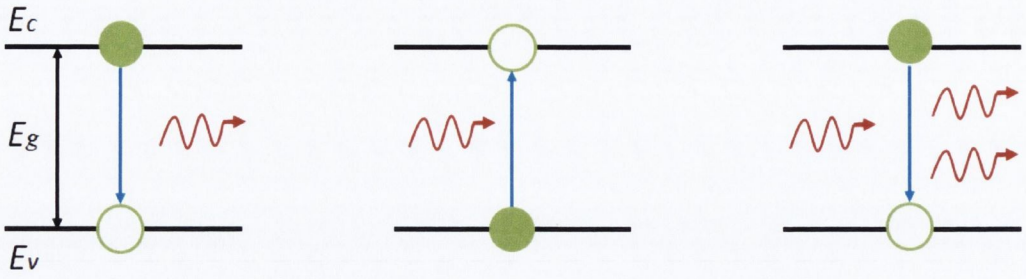

Fig. 2.1 Electronic transition between the conduction and valence bands. Solid circles correspond to filled states (electrons). Open circles correspond to unfilled states (holes). (left) Spontaneous recombination. (center) Stimulated carrier generation. (right) Stimulated recombination.

The processes described above relate to radiative transitions where the energy is released as a photon. There is another type of transition, non-radiative process. In non-radiative processes, the electron-hole pair recombines without emitting a photon. Instead of this, the energy can be dissipated as heat and generate phonons or it can be given to electron or hole in the form of kinetic energy. The latter process is called Auger recombination. Non-radiative recombination may also occur due to imperfections and defects in the active region of the laser.

2.1.2. Optical gain

Several conditions should be satisfied to realize laser diode [9]:

- an optical gain to provide amplification
- an optical waveguide to confine the photons
- an optical resonator to provide a feedback

The optical gain in semiconductor lasers can be achieved when the stimulated emission in a strongly pumped region is larger than the optical losses. In semiconductor lasers, the active region acts as a gain medium where the optical field propagates. If we consider a plane wave, we can characterize the propagation of this wave in the medium through the complex propagation constant

$$\beta = k_0 n = k_0(n' + jn''), \tag{2.1}$$

where k_0 is the free-space propagation, n' and n'' are the real and imaginary parts of the complex refractive index. From [10], the intensity of the plane wave varies exponentially

$$I = \frac{c\varepsilon_0}{2} n' |E_0|^2 \exp(2k_0 n'' z), \tag{2.2}$$

where E_0 is the amplitude of the electric field. The corresponding gain is a negative value of the loss and can be defined as

$$g = -\alpha = \frac{1}{I}\frac{\mathrm{d}I}{\mathrm{d}z} = 2k_0 n''. \tag{2.3}$$

The important property of laser diodes is that the gain is very large, which is order of magnitude larger than any other types of lasers [11]. Therefore, diode lasers can be very small but have high power. Additional feature of laser diodes is that the gain curve is wide (~10 nm), which is due to optical transition between a pair of energy bands, rather than well-defined atom-like states. Another feature is that the relationship between the gain and the carrier density can be approximated as a linear function [12]

$$g = a(N - N_0), \tag{2.4}$$

where a is a differential gain and N_0 is a transparency value of the carrier density. The linear approximation in (2.4) is invalid for quantum well lasers. The description of quantum well lasers will be given in the following sections.

2.1.3. Heterostructures

The basic structure of the semiconductor lasers include an active region (undoped) sandwiched between two wide-bandgap materials, one n-doped and second p-doped forming p-n junction. Such type of structure is known as a double-heterostructure. The concept of the double-heterostructure laser was introduced by Alferov [13] and Kroemer [14] in 1963. The first continuous-wave (CW) operation of these lasers was demonstrated in 1970 [15], [16]. A band diagram of a forward-biased double-heterostructure is shown in Fig. 2.2. Under forward bias condition, electrons from the n-doped region and holes from the p-doped region are injected into the active region. Due to the high-bandgap energy from the both sides of the active region, the injected electrons and holes cannot escape the active region. Therefore, the carriers are confined in this region and forced to recombine to generate photons. Moreover, the active region also confines the photons because the

refractive index of the active region is higher than the refractive indices of the carrier confinement layers. Thus, the active layer will serve as an optical waveguide. For efficient recombination, direct bandgap semiconductor materials should be used. Typically, these are compound materials and well known III-V materials, including GaAs, InP, InGaAs and InGaAsP materials.

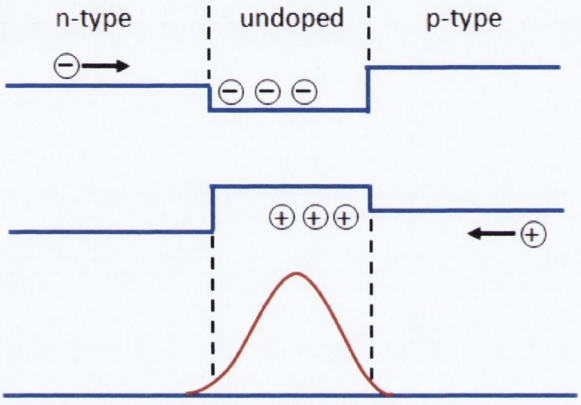

Fig. 2.2 Simplified band diagram of double-heterostructure under forward-bias condition. The bottom plot shows the guided waveguide mode.

The thickness d of the active region of typical bulk material is around 100 nm. With the development of advanced epitaxial growth techniques, such as molecular beam epitaxy (MBE) and metal-organic vapor-phase epitaxy (MOVPE) it is possible to make the thickness of the active region only a few nanometers (d~10 nm). This value is smaller than the de Broglie wavelength of the carriers, which is around 15 nm. In these dimensions, a quantization effects of the confined carriers occur and the density of states of the quantum well lasers take a steplike behavior as shown in Fig. 2.3. Due to the small sizes of the active region, quantum wells exhibit a low threshold current and large material gain.

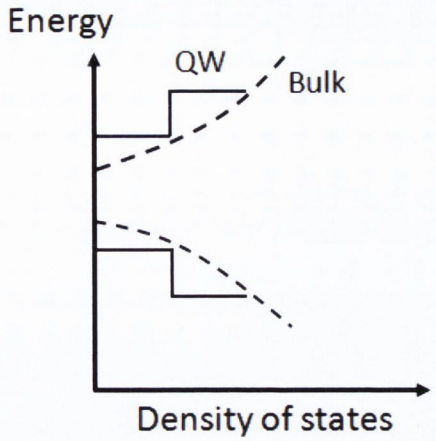

Fig. 2.3 Density of states of quantum well (solid line) and bulk semiconductor (dashed curve).

Although, the carrier confinement is very strong in quantum wells, the optical confinement is weak due to the small thickness of the active region. To increase the optical confinement, an additional optical waveguide around the quantum well is needed. Such structures are called separate confinement heterostructure quantum well (SCH-QW) structures. If the waveguide consists of a graded composition, then the corresponding structure will be a graded refractive index SCH-QW structure (GRINSCH-QW structure). More details about quantum well structures and physics can be found in [17], [18]. Due to their unique optical and electronic properties, quantum well structures are used in almost all modern laser diodes.

2.1.4. Optical resonator

As was mentioned above, to get the laser to work optical feedback is required. The feedback is generated by placing an active medium in an optical resonator, where the light is reflected between two mirrors. Usually in laser diodes, the feedback is provided by simply cleaving the facets forming two parallel mirrors. In the previous section, we described double-heterostructures where the active region acts as a dielectric waveguide due to higher refractive index than the confinement layers. The dielectric waveguide consists of one or more guided transverse modes, which are polarized either transverse electric (TE) or transverse magnetic (TM). Since the active layer acts as a dielectric waveguide, these modes can spread into the cladding layers. The strength of the mode confinement in the active

layer is defined by the confinement factor Γ, which is the fraction of the mode power confined in the active layer. If we will consider a symmetric dielectric waveguide with thickness d, and refractive index n_1 as shown in Fig. 2.4, then we can define Γ as follows:

$$\Gamma = \frac{\int_{-d/2}^{d/2} |E_y|^2 \, dx}{\int_{-\infty}^{\infty} |E_y|^2 \, dx}, \tag{2.5}$$

where $|E_y|$ is the amplitude of electric field (with assumption that TE mode is dominant). The Γ factor is dependent on refractive index difference and the active layer thickness. The wavelength dependent modal gain, is given by this Γ factor and the active layer gain g_a and written as

$$g_{eff} = \Gamma g_a. \tag{2.6}$$

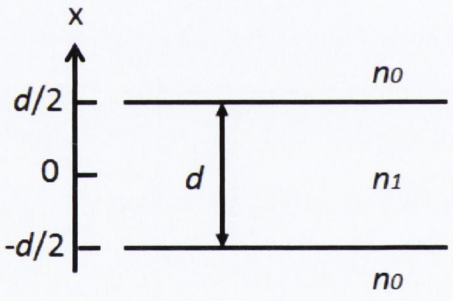

Fig. 2.4 Schematic cross-section of a dielectric waveguide with thickness d. n_1 is the refractive index of active layer, and n_0 is refractive index of confinement layers [10].

The simplest type of a laser is a Fabry-Perot laser which typically consists of two cleaved facets with mirror reflectivity R_1 and R_2 as depicted in Fig. 2.5. The backward-going and forward-going waves are defined by a propagation constant β as in (2.1)

$$\beta = k_0 n'_{eff} + j\frac{g_{net}}{2}, \tag{2.7}$$

$$g_{net} = g_{eff} - \alpha_i, \tag{2.8}$$

where g_{net} is the net modal gain and α_i is the optical losses.

Fig. 2.5 Schematic view of Fabry-Perot laser with length L and mirror reflectivities R_1 and R_2.

To satisfy a steady-state oscillation condition, the round-trip gain of the cavity must be equal to 1 and can be expressed as

$$r_1 r_2 e^{-2j\beta L} = 1, \tag{2.9}$$

where r_1 and r_2 are the amplitude reflectivities. The imaginary and real parts of equation (2.9) give two different conditions, one is for the amplitude and the other is for the phase condition. From the phase condition, the round-trip phase is equal to an integer multiple of 2π. This will lead to the resonance condition of the cavity and a standing wave occurs between two mirrors. This will form a set of longitudinal modes with wavelength

$$\lambda = \frac{2n'_{eff}L}{m}, \tag{2.10}$$

and mode spacing

$$\Delta\lambda_{FP} = \lambda_m - \lambda_{m+1} = \frac{\lambda_m^2}{2n_{g,eff}L}, \tag{2.11}$$

where $n_{g,eff}$ is the group refractive index.

The spectrum of a Fabry-Perot laser is multi-mode as it is shown in Fig. 2.6. The multi-mode spectrum has negative consequences in long-haul fiber-optic communications due to the dispersion in the fibers which can limit the achievable data transmission rate. For this purpose, a single-mode laser is required. The ways to achieve a single-mode operation will be discussed in the following sections.

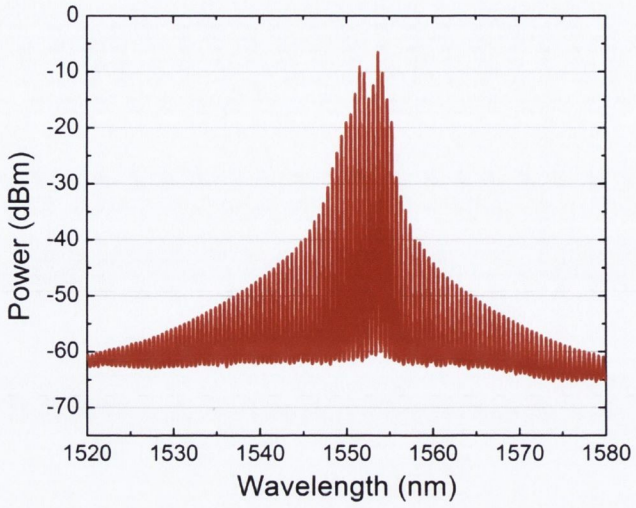

Fig. 2.6 Optical spectrum of a Fabry-Perot laser with emission peak at 1550 nm. The individual lines are the longitudinal modes of the laser.

2.2. Laser diode characteristics

2.2.1. The rate equations

The simplest way to describe the behavior of laser diodes is to use the rate equations. These equations express the balance of carriers and photons in the system. The rate equations for the carrier density N and the average photon density N_{ph} in the active region can be written as [10], [19]

$$\frac{\mathrm{d}N}{\mathrm{d}t} = \frac{I}{qV_a} - v_g g_{eff} N_{ph} - R(N), \tag{2.11}$$

$$\frac{\mathrm{d}N_{ph}}{\mathrm{d}t} = v_g g_c N_{ph} + R_{sp}, \tag{2.12}$$

where v_g is the group velocity, $R(N)$ is the spontaneous recombination rate, g_c is the cavity gain and R_{sp} is the spontaneous emission into the lasing mode.

For a steady-state case, carrier and photon densities do not change

$$\frac{dN}{dt} = 0,$$
$$\frac{dN_{ph}}{dt} = 0. \tag{2.13}$$

Fig. 2.7 shows a schematic view of the output power as a function of current and carrier density as a function of current. The point where the output power increases linearly is called the threshold current which can be obtained from the rate equation (2.11), assuming that the photon density is zero

$$I_{th} = qV_a R(N_{th}), \tag{2.14}$$

where the carrier density remains constant above threshold $N = N_{th}$, and this behavior is called gain-clamping.

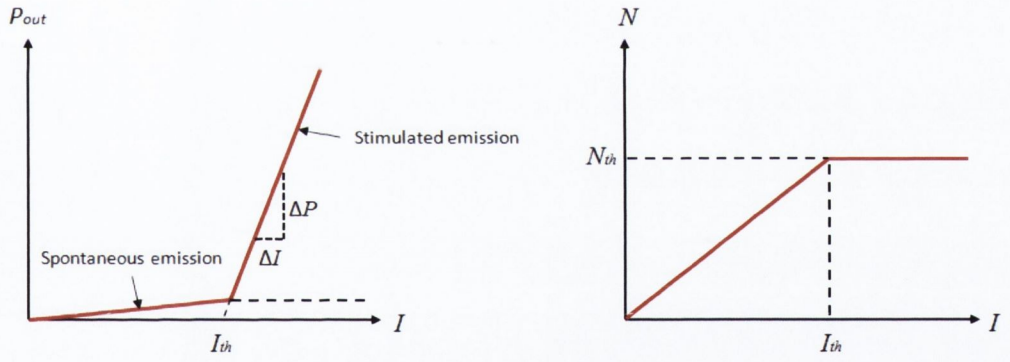

Fig. 2.7 Schematic view of (left) output power vs. current, and (right) carrier density vs. current. Below laser threshold there is no photon emitted except spontaneously emitted photons therefore, the laser operates in spontaneous emission mode. Above threshold, the laser output power increases linearly with the current. The carrier density has a constant value above threshold and this effect is called gain-clamping.

The photon density above threshold will be written as

$$N_{ph} = \frac{I - I_{th}}{qV_a v_g \alpha_{tot}}, \tag{2.15}$$

where α_{tot} is the total cavity loss which is the sum of mirrors loss (α_m) and internal loss (α_i). By taking into account the photon density given in (2.15), we define the optical power from each facet as

$$P = \frac{h\nu}{2q}\frac{\alpha_m}{\alpha_{tot}}(I - I_{th}). \tag{2.16}$$

Above the threshold current, the laser output power increases linearly with the injection current. The differential efficiency η_d is defined as

$$\eta_d = \frac{q}{h\nu}\frac{\mathrm{d}P}{\mathrm{d}I}, \tag{2.17}$$

where $\mathrm{d}P/\mathrm{d}I$ is the slope efficiency which shows the efficiency of a laser diode and measured in a units of mW/mA.

The left hand side of Fig. 2.7 is usually referred as a light-current curve or $L - I$ curve. From this curve it is possible to determine the basic characteristics such as threshold current, I_{th}, and slope efficiency, $\mathrm{d}P/\mathrm{d}I$. Moreover, from the $L - I$ curve internal laser parameters can be calculated, including the internal optical losses and the quantum efficiency of a laser.

The $L - I$ curve is strongly affected by the temperature and the threshold current changes exponentially with the change of temperature

$$I_{th} \sim \exp\left(\frac{T}{T_0}\right), \tag{2.18}$$

where T_0 is the characteristic temperature which defines the temperature stability of the device. Further explanation about the characteristic temperature and the measurement results will be given in Chapter 5.

2.2.2. The spectral characteristics

There are two basic types of lasers, which are termed single-mode and multi-mode. We have already demonstrated a Fabry-Perot laser operating with a multi-mode spectrum. It was mentioned that it has a negative influence on data transmission therefore, the spectral purity of laser diodes is crucial. In this section we will introduce single-mode operation.

A laser can be defined as a single-mode, if the ratio of the power in the strongest mode to the power in the next weakest mode exceeds a given number [11]. The parameter that

determines the single-mode operation is called a side-mode suppression ratio (SMSR). The SMSR can be calculated using rate equations [20] for steady-state condition

$$\frac{dN_{ph_m}}{dt} = 0 = R_{sp}(\lambda_m) + N_{ph_m} v_g g_c(\lambda_m), \tag{2.19}$$

$$\frac{dN_{ph_{m+1}}}{dt} = 0 = R_{sp}(\lambda_{m+1}) + N_{ph_{m+1}} v_g g_c(\lambda_{m+1}), \tag{2.20}$$

where m and $m+1$ are the dominant and the second strongest modes, respectively. The SMSR will be the ratio of these modes

$$SMSR = \frac{N_{ph_m}}{N_{ph_{m+1}}}. \tag{2.21}$$

From the experimental measurements, the SMSR can be calculated as the difference in the optical power of the main mode and the next strongest mode. An example of this single-mode operation is demonstrated in Fig. 2.8. The optical power of the main mode is -10 dBm and the optical power of the next strongest mode is around -56 dBm. Hence, the SMSR of the given single-mode laser is around 46 dB. It should be noted that the SMSR unit is given in dB and not in dBm. The reason is that dB is used to evaluate the ratio between two optical powers (intensities), while dBm is used to quantify an absolute value of the power.

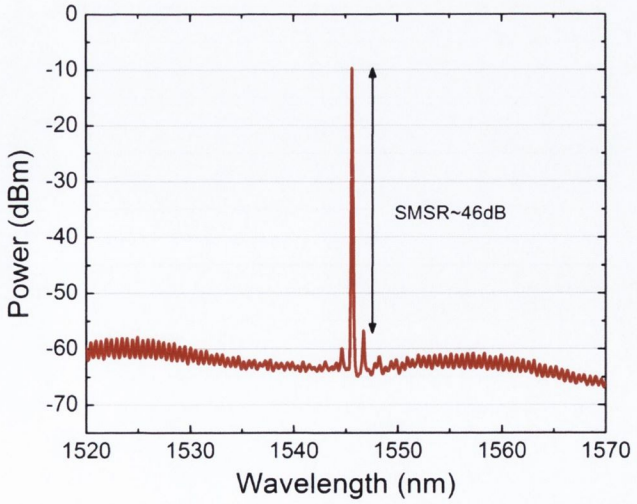

Fig. 2.8 Measured optical spectrum of a single-mode laser.

There are several ways of achieving single-mode operation such as making a laser cavity short so the mode spacing between adjacent modes exceeds the width of the gain curve,

thus only one mode will exist near the gain peak. Operation on a single-mode can be also achieved by using multiple-mirror resonators [21]. Examples of achieving single-mode operation are presented in [11]. However, the most widely used method is to use periodic structures or gratings for mode selectivity. It should be mentioned that the lasers in this thesis are based on high-order gratings. The detailed description of grating theory and the examples of lasers exploiting gratings in their structures will be given in Chapter 3.

2.2.3. The laser linewidth

Schawlow-Townes linewidth

The spectral linewidth of a laser diode is an important parameter in coherent communication systems and in the systems with high order optical modulation formats [differential phase shifting keying (DPSK) and differential quadrature phase shift keying (DQPSK)]. For these high speed modulation formats, the phase noise of the light must be low. Therefore, the main requirement is a narrow laser linewidth [22], [23] which is typically below 500 kHz.

Although, the spectral width of a single-mode laser is very narrow, the linewidth will be still finite due to noise caused by spontaneous emission. Spontaneous emission is inherent for all lasers due to generation of incoherent photons spontaneously which will add to the lasing mode. These photons will have a random phase. The schematic of the situation when a photon with a random phase is added to the field is shown in Fig. 2.9. The light generated through the stimulated emission with phase ϕ, creates an optical field. The light generated through the spontaneous emission has a random phase of θ_i, and it alters the optical field changing its amplitude and phase.

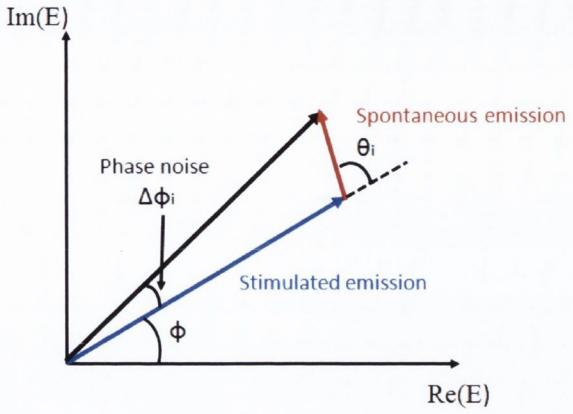

Fig. 2.9 Phasor model of the field showing the phase change of the optical field due to spontaneous emission.

From Fig. 2.9 the phase change $\Delta\phi_i$ is found as

$$\Delta\phi_i = \frac{1}{\sqrt{N'}}\sin(\theta_i), \tag{2.22}$$

where N' is the number of photons and θ_i is the random phase caused by spontaneous emission. This is called phasor theory and it is used when a laser is operated above its threshold.

A laser linewidth can be expressed by the well-known Schawlow-Townes formula [2] which states, that the linewidth is inversely proportional to the photon density or output power and can be represented as

$$\Delta\nu = \frac{h\nu(v_g)^2(\alpha_i + \alpha_m)\alpha_m R_{sp}}{8\pi P}, \tag{2.23}$$

where $h\nu$ is the photon energy, v_g is the group velocity, P is the optical power.

However, the Schawlow-Tones linewidth is valid for below threshold operation, while above threshold, linewidth broadening will be due to carrier density fluctuations. A change in the carrier density will lead to a change of the refractive index, therefore, the phase will change. This will broaden the linewidth by factor of $(1 + \alpha^2)$ [24], where α is the termed linewidth enhancement factor. This $(1 + \alpha^2)$ correction factor was introduced by Henry to the Schawlow-Townes linewidth (2.23). For the nonlinear, above threshold, regime the expression will be modified and is written as

$$\Delta\nu_{STH} = \frac{h\nu(v_g)^2(\alpha_i + \alpha_m)\alpha_m R_{sp}}{8\pi P}(1 + \alpha^2), \tag{2.24}$$

which is referred to as the Schawlow-Townes-Henry linewidth.

2.3. Wavelength tuning

2.3.1. Tuning mechanisms

The wavelength tunability of a laser diode is an important property in most applications where it is used. In this section, the main wavelength tuning mechanisms will be described. In the following, the material about tuning mechanisms is summarized from [10].

There are three different types of electronically tuning schemes: continuous, discontinuous and quasi-continuous tunings as shown in Fig. 2.10.

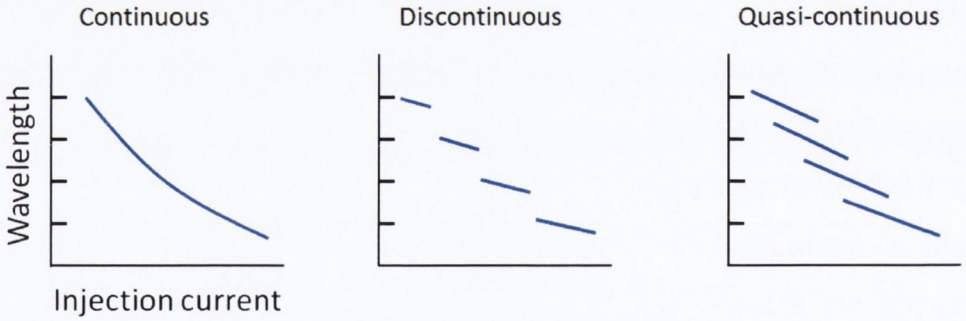

Fig. 2.10 Schematic diagram of (left) continuous, (center) discontinuous and (right) quasi-continuous tuning scheme.

Continuous wavelength tuning is the ideal tuning scheme in optical-fiber communications [20], [25]. In continuous tuning the laser wavelength is tuned smoothly in small steps without mode changes, so that light in the same cavity mode will be emitted throughout the entire tuning range. This means that the laser parameters will be maintained and the laser exhibit stable single-mode operation with reasonably high SMSR during continuous tuning. The accuracy of wavelength tuning is adjustable down to about the spectral linewidth. However, a typical wavelength tuning range is relatively narrow (~3-

4 nm). The maximum tuning range of only 15 nm is achievable [26]. An example of a laser using continuous tuning is a distributed feedback (DFB) laser.

To achieve larger tuning ranges, discontinuous tuning can be used where discrete wavelength jumps occur. In discontinuous tuning, the tuning range is determined by cavity gain which leads to longitudinal mode jumps. This means that a larger tuning range is possible. The tuning range is now between 50-100 nm [27].

The last tuning method is quasi-continuous tuning which is achieved by adding together overlapped intervals of each continuously tunable regimes. The tuning range is between 30-50 nm. The examples of quasi-continuous tuning can be observed in super-structure-grating DBR (SSG-DBR) lasers [28] and wavelength tunable DFB laser arrays [29].

The electronic wavelength control requires the integration of additional wavelength control or the filter into the cavity to tune the cavity roundtrip gain. In the case of tunable DFB or DBR laser, the filter is the Bragg reflector as shown in Fig. 2.11. From the Bragg condition $\lambda_B = 2n_{eff}\Lambda$, the wavelength is dependent on grating pitch and the effective refractive index of grating section. So the tuning of the cavity gain can be achieved by electronic control of the refractive index n_{eff}, which can be done either by applying current or voltage.

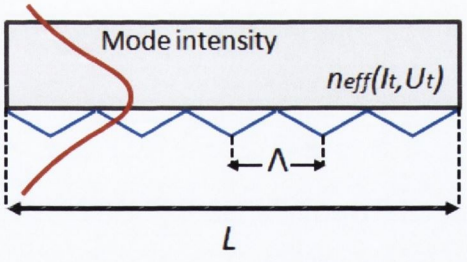

Fig. 2.11 The schematic of the tunable Bragg reflector.

For a single-mode DFB laser, the change in the effective refractive index of the grating section, will lead to a wavelength variation λ_{tune}, and this can be expressed as

$$\frac{\lambda_{tune}}{\lambda_0} = \frac{\Delta n_{eff}}{n_{g,eff}}, \tag{2.25}$$

where $n_{g,eff}$ is the group effective index and λ_0 is the Bragg wavelength. Equation (2.25) is valid for continuous tuning. However, the continuous wavelength tuning in (2.25) is limited

by the maximum amount of achievable effective index change. Practically, the maximum index change is around 1%, therefore, the tuning range is limited to about 0.5-1% of the wavelength which is the maximum 10-15 nm of wavelength tuning. Significantly larger tuning range can be achieved in discontinuous tuning, where the tuning is achieved by mode hops from one longitudinal mode to another, so therefore the limitation (2.25) is no longer valid.

To sum up, the electronic wavelength control of a laser diode is dependent on the ability to control the refractive index of the laser. The practically applicable physical effects for the electronic refractive index control are: 1) free-carrier plasma effect [30], [31], [32], 2) the quantum confined Stark effect (QCSE) [33], [34], and 3) temperature tuning [35], [36].

2.3.2. Physical effects for electronic wavelength tuning

In the **free-carrier plasma effect** the change in the refractive index is caused by the injected electron-hole plasma into a semiconductor [10]. Two physical mechanisms will cause the change in the refractive index. First is the polarization of the free carriers which will reduce the refractive index proportionally to the carrier density. Second is the spectral shift of the absorption edge of the semiconductor to the higher energies which will also reduce the refractive index [37].The maximum refractive index change is -0.04 [37]. The negative aspect of this effect is that, the carrier injection and recombination will cause heat generation in the device which will lead to so-called parasitic thermal tuning which will reduce the refractive index change. Despite the heating, the carrier injection is the most widely used technique to achieve electronic wavelength control. The wavelength tuning of DBR lasers rely on this effect.

In the **quantum confined Stark effect** the applied electric field will change the refractive index. The principle is that a quantum well structure is placed in a reverse biased pn-junction. The applied electric filed will reduce the bandgap energy making the band edges inclined to each other. Thereby, the refractive index will be modified. The main advantage of the QCSE over the free-carrier plasma is the operation in reverse bias. This will not increase the temperature of the device. However, the refractive index changes are typically of the order 10^{-3} to 10^{-2} [34], which is a relatively small effect. Therefore, QCSE is often used for electro-absorption modulations where an electric field applied to the quantum well

structure will cause a red-shifted optical absorption, so that the optical transmission in the waveguide can be modulated [38]. The demonstration of this effect will be discussed in Chapter 5.

The last effect which changes the refractive index and thereby the wavelength, is the **thermal tuning effect**. The gain peak of wavelength of the active medium is dependent on temperature and can be thermally tuned. This is due to temperature dependence of the bandgap energy and the Fermi distribution. Typical gain peak tuning is about 0.5 nm/K for a Fabry-Perot (FP) laser which is because the gain peak of FP laser consists of several longitudinal modes and each of these modes are dependent on the refractive index as shown in equation (2.10). Therefore, the temperature dependence in FP lasesr is higher than in single-mode lasers. For single-mode lasers, the change in the temperature will change the refractive index and hence shift the wavelength. So for single-mode DFB and DBR lasers, the tuning rate is around 0.1 nm/K [39]. For example, a single-mode DFB laser with tuning rate of 0.1 nm/K can obtain 6 nm of wavelength tuning over the temperature change between 20 to 80°C. It is possible to achieve larger tuning by increasing the temperature, however, the heat generation will increase the threshold current as shown in eq. (2.18), decrease optical power, reduce the SMSR and broaden the linewidth at high temperatures.

The comparison of above-described physical mechanisms for laser tuning is shown in Table 2.1 from [10].

Parameter	*Plasma effect*	*QCSE*	*Temperature tuning*
Δn	-0.04	-0.01	0.01
Γ	0.5	0.2	1
$\Delta\lambda_{tune}$	-8nm	-1nm	+5nm
$\Delta\nu$	100MHz	>10MHz	<1MHz
Heat generation	large	negligible	very large
Technology	moderate	demanding	simple

Table 2.1 Comparison of tuning mechanisms for semiconductor laser diodes in terms of different parameters, where Δn is the refractive index change, Γ is the optical confinement factor, $\Delta\lambda_{tune}$ is the output wavelength change, $\Delta\nu$ is the linewidth.

There is another type of tuning related to the refractive index change, it is so-called Vernier tuning [40], where relatively small refractive index changes will provide relatively large wavelength changes. The principal of Vernier tuning is, the device structure consists of two mirrors with comb-like reflection spectra, but exhibits different comb pitches, therefore, the Vernier effect can be used to expand the tuning range. The comb-like reflection spectra can be achieved by spatially modulated Bragg gratings such as sampled gratings [40] or super-structure gratings [41]. Lasers such as Sample Grating Distributed Bragg Reflector (SG-DBR) lasers exploit the Vernier tuning which provides a much wider tuning range in comparison with, for instance, two section DBR lasers. A tuning range of 60 nm was demonstrated in [42], [43]. Wavelength tunability can also be achieved by mechanical tuning in the case of external cavity laser diodes [44] with a widely tunable filter (grating) in the free space part. The tuning can be obtained by simply rotating the grating.

References

[1] A. Einstein, "Zur Quantentheorie der Strahlung (On the quantum theory of radiation)," *Physika Zeitschrift*, vol. 18, pp. 121-128, 1917.

[2] A. L. Schawlow and C. H. Townes, "Infrared and optical masers," *Physics Review,* vol. 112, no. 6, pp. 1940-1949, 1958.

[3] T. H. Maiman, "Stimulated optical radiation in ruby," *Nature,* vol. 187, pp. 493-494, 1960.

[4] R. N. Hall, G. E. Fenner, J. D. Kingsley, T. J. Soltys and R. O. Carlson, "Coherent light emission from GaAs junctions," *Physics Review Letters,* vol. 9, no. 9, pp. 366-368, 1962.

[5] T. M. Quist, R. H. Rediker, R. J. Keyes, W. E. Krag, B. Lax, A. L. McWhorter and J. Zeiger, "Semiconductor maser of GaAs," *Applied Physics Letters,* vol. 1, no. 4, pp. 91-92, 1962.

[6] M. I. Nathan, W. P. Dumke, G. Burns, F. H. Dill and G. Lusher, "Stimulated emission of radiation from GaAs p-n junctions," *Apllied Physics Letters,* vol. 1, no. 3, pp. 62-64, 1962.

[7] N. Holonyak and S. F. Bevacqua, "Coherent (Visible) light emission from $Ga(As_{1-x}P_x)$ junctions,"

Applied Physics Letters, vol. 1, no. 4, pp. 82-83, 1962.

[8] J. Hecht, "A short history of laser development," *Applied Optics,* vol. 49, no. 25, pp. F99-F122, 2010.

[9] P. Unger, "High power diode lasers: Introduction to power diode lasers," *Topics in Applied Physics,* vol. 78, pp. 1-54, 2000.

[10] M. C. Amann and J. Buus, Tunable laser diodes, Norwood: ARTECH HOUSE, INC., 1998.

[11] J. Buus, Single frequency semiconductor lasers, SPIE Press, 1991.

[12] H. Ghafoori-Shiraz, "Temperature, bandgap-wavelength, and doping dependence off peak-gain coefficient parabolic model parameters for InGaAsP/InP semiconductor laser diodes," *Journal of Lightwave Technology,* vol. 6, no. 4, pp. 500-506, 1988.

[13] Z. I. Alferov and R. F. Kazarinov, "Author's certificate no. 1032155/26-25 USSR," 1963.

[14] H. Kroemer, "A proposed class of heterojunction injection lasers," *Proceedings of the IEEE,* vol. 51, p. 1782, 1963.

[15] Z. I. Alferov, V. M. Andreev, E. L. Portnoi and M. K. Trukan, "AlAs-GaAs heterojunction injection lasers with a low room-temperature threshold," *Fiz. Tekh. Polupprov.,* vol. 3, pp. 1328-1332, 1969.

[16] I. Hayashi, P. B. Panish, P. W. Foy and S. Sumski, "Junction lasers which operate continuously at room temperature," *Applied Physics Letters,* vol. 17, no. 3, pp. 109-111, 1970.

[17] C. Weisbuch and B. Vinter, Quantum semiconductor structures, Boston, MA: Academic Press, 1991.

[18] P. S. Zory, Quantum well lasers, Boston, MA: Academic Press, 1993.

[19] L. A. Coldren and S. W. Corzine, Diode lasers and photonic integrated circuits, New York: John Wiley & Sons, 1995.

[20] T. L. Koch and U. Koren, "Semiconductor lasers for coherent optical fiber communications," *IEEE Journal of Lightwave Technology,* vol. 8, pp. 274-293, 1990.

[21] E. A. Bahaa. Saleh and M. C. Teich, Fundamentals of photonics, Hoboken, New Jersey: John Wiley & Sons, Inc., 2007.

[22] S. Savory and A. Hadjifotiou, "Laser linewidth requirements for optical DQSPK systems," *IEEE Photonic Technology Letters,* vol. 16, no. 3, pp. 930-932, 2004.

[23] M. Seimetz, "Laser linewidth limitations for optical systems with high order modulation employing feed forward digital carrier phase estimation," in *Optical Fiber Communication*

Conference, San Diego, CA, 2008.

[24] C. H. Henry, "Theory of the linewidth of semiconductor lasers," *IEEE Journal of Quantum Electronics,* vol. 18, pp. 259-264, 1982.

[25] K. Kobayashi and I. Mito, "Single frequency and tunable laser diodes," *IEEE Journal of Lightwave Technology,* vol. 6, pp. 1623-1633, 1988.

[26] M. C. Amann, "Broad-band wavelength-tunable twin-guide lasers," *Optoelectronics-Devices and Technologies,* vol. 10, pp. 27-38, 1995.

[27] R. C. Alferness, "Widely tunable semiconductor lasers," in *Optical Fiber Communication Conference*, San Jose, CA, 1993.

[28] H. Ishii, H. Tanobe, F. Kano, Y. Tohmori, Y. Kondo and Y. Yoshikuni, "Quasicontinuous wavelength tuning in super-structure-grating (SSG) DBR lasers," *IEEE Journal of Quantum Electronics,* vol. 32, no. 3, pp. 433-440, 1996.

[29] H. Oohashi, Y. Shibata, H. Ishii, Y. Kawaguchi, Y. Kondo, Y. Yoshikuni and Y. Tohmori, "46.9-nm Wavelength-selectable arrayed DFB lasers with integrated MMI coupler and SOA," in *Internation Conference On Induim Phosphide and Realted Materials*, Nara, Japan, 2001.

[30] L. D. Westbrook, "Measurement of dg/dN and dn/dN and their dependence on photon energy in λ=1.5 μm InGaAsP laser diodes," *Optoelectronics, IEE Proceedings J,* vol. 133, no. 2, pp. 135-142, 1986.

[31] M. Okuda and K. Onaka, "Tunability of distributed Bragg-reflector laser by modulating refractive index in corrugated waveguide," *Japanese Journal of Applied Physics,* vol. 16, pp. 1501-1502, 1977.

[32] B. Bennet, R. Soref and J. Del Alamo, "Carrier-induced change in refractive index of InP, GaAs, and InGaAsP," *IEEE Journal of Quantum Electronics,* vol. 26, pp. 113-122, 1990.

[33] D. A. Miller, D. S. Chemla, T. C. Damen, T. C. Gossard, W. Wiegmann, T. H. Wood and C. A. Burrus, "Band edge electroabsorption in quantum well structures: the quantum confined Stark effect," *Physical Review Letters,* vol. 53, pp. 2173-2176, 1984.

[34] J. E. Zucker, I. Bar-Joseph, B. I. Miller, U. Koren and D. S. Chemla, "Quaternary quantum wells for electro-optic intensity and phase modulation at 1.3 and 1.55 μm," *Applied Physics Letters,* vol. 54, pp. 10-12, 1988.

[35] S. L. Woodward, U. Koren, B. I. Miller, M. G. Young, M. A. Newkirk and C. A. Burrus, "A DBR laser tunable by resistive heating," *IEEE Photonics Technology Letters,* vol. 4, no. 12, pp. 1330-1332, 1992.

[36] T. Kameda, H. Mori, S. Onuki, T. Kikugawa, Y. Takahashi, F. Tsuchiya and H. Nagai, "A DBR laser employing passive-section heaters, with 10.8 nm tuning range and 1.6 MHz linewidth," *IEEE*

Photonic Technology Letters, vol. 5, no. 6, pp. 608-610, 1993.

[37] J. P. Weber, "Optimization of the carrier-induced effective index change in InGaAsP waveguides-application to tunable Bragg filters," *IEEE Journal of Quantum Electronics,* vol. 30, no. 8, pp. 1801-1816, 1994.

[38] A. Ramdane, F. Devaux, N. Souli, D. Delprat and A. Ougazzaden, "Monolithic integration of multiple-quantum-well lasers and modulators for high-speed transmission," *IEEE Journal of Selected Topics in Quantum Electronics,* vol. 2, no. 2, pp. 326-335, 1996.

[39] K. Chinen, K. Gen-Ei, H. Suhara, A. Tanaka, T. Matsuyama, K. Konno and Y. Muto, "Low-threshold 1.55 μm InGaAsP/InP buried heterostructure distributed feedback lasers," *Applied Physics Letters,* vol. 51, no. 4, pp. 273-275, 1987.

[40] V. Jayaraman, Z. M. Chuang and L. A. Coldren, "Theory, design, and performance of extended tuning range semiconductor lasers with sampled gratings," *IEEE Journal of Quantum Electronics,* vol. 29, no. 6, pp. 1824-1834, 1993.

[41] Y. Tohmori, Y. Yoshikuni, H. Ishii, F. Kano, T. Tamamura, Y. Kondo and M. Yamamoto, "Broad-range wavelength-tunable superstructure grating (SSG) DBR lasers," *IEEE Journal of Quantum Electronics,* vol. 29, no. 6, pp. 1817-1823, 1993.

[42] B. Mason, G. A. Fish, J. Barton, L. A. Coldren and S. P. DenBaars, "Characteristics of sampled grating DBR lasers with integrated semiconductor optical amplifiers," *IEEE Photonics Technology Letters,* vol. 12, no. 7, pp. 762-764, 2000.

[43] M. Nawrocka, Q. Lu, W. H. Guo, A. Abdullaev, F. Bello, J. O'Callaghan, T. Cathcart and J. F. Donegan, "Widely tunable six section semiconductor laser based on etched slots," *Optics Express,* vol. 22, no. 16, pp. 18949-18957, 2014.

[44] D. Mehuys, D. Welch and D. Scifres, "1W CW, diffraction-limited, tunable external-cavity semiconductor laser," *Electronics Letters,* vol. 29, no. 14, pp. 1254-1255, 1993.

Chapter 3 – The gratings in laser diodes

3.1. Introduction

As we discussed in the previous chapter, laser diodes use different types of cavity structures such as gratings or simple mirrors to achieve optical feedback. In simple Fabry-Perot lasers, the feedback is achieved through cleaved facets. DFB and DBR lasers use wavelength selective filters or gratings to achieve feedback and single-mode operation. Therefore, when dealing with such cavity structures it is important to understand the transmission and reflection from these structures.

Generally, the grating structures are composed of many layers and the problem is to match the boundary conditions across the interfaces of these layers. Because of the large number of layers, it is hard to solve all layers simultaneously. Instead of this, it is more efficient to solve a boundary condition of one layer at a time. For this the transfer matrix (TMM) and the scattering matrix (SMM) algorithms are used. In the transfer matrix method to define the transmission and reflection coefficients, all transfer matrices are simply multiplied. However, it is a straightforward method and it is numerically unstable when the layer structure is large [1]. Therefore, it does not include the scattering losses. On the other hand, the scattering matrix method is a stable and efficient algorithm which does not have numerical instabilities [2].

This chapter organized as follows. First a brief description of scattering and transmission matrix methods will be given. Then we will discuss wave propagation in simple layer structures and calculate the reflection and transmission coefficients. Finally, we will introduce the gratings, particularly distributed Bragg gratings and discuss about DBR and DFB lasers.

3.2. Scattering matrix and transmission matrix theory

To analyze the reflection and transmission properties scattering theory can be used [3], [4]. The detailed explanation of the scattering matrix method is given in Coldren and Corzines' book [5]. In the following we will work with normalized amplitudes, a_j, because it is convenient for complex cavity structures. The magnitude of a_j is equal to the square root of the power flow. For more convenience we choose to reference the phase to the electric field, which is given as

$$E(x,y,z,t) = \hat{e}E_o U(x,y)e^{j(\omega t-\tilde{\beta}z)}, \tag{3.1}$$

where $\hat{e}$ is the unit vector, E_o is the field magnitude, $U(x,y)$ is the normalized electric field profile, ω is the angular frequency, $\tilde{\beta}$ is a propagation constant. The normalized amplitude can be expressed as

$$a_j = \frac{E_0}{\sqrt{2\eta_j}}e^{-\tilde{\beta}z}, \tag{3.2}$$

where η_j is the mode impedance which is the ratio of the transverse electric to transverse magnetic field magnitudes of the mode. If $\int|U|^2dxdy = 1$, then the power flow will be as $P_j^+ = a_j a_j^*$, and the power flow will be in the z-direction with positive sign. If we will consider a waveguide system, there will be two propagating modes. One propagates in the positive z-direction and is referred as incident waves. The second propagates in the opposite direction and is referred to as reflected waves. The net power flowing with incident and reflected powers into the port j is defined as

$$P_j = a_j a_j^* - b_j b_j^*. \tag{3.3}$$

where a_j is the normalized amplitude of the incident (input) waves and b_j is the normalized amplitude of reflected (output) waves. The scattering matrix couples these input waves a_j and output waves b_j and can be expressed as

$$b_i = \sum_j S_{ij} a_j, \tag{3.4}$$

where S_{ij} are the scattering coefficients. From (3.4) to determine a particular S_{ij}, all inputs except a_j must be set to zero which is,

$$S_{ij} = \left.\frac{b_i}{a_j}\right|_{a_k=0, k\neq j}. \tag{3.5}$$

The more general view of (3.5) can be written as

$$b = Sa, \tag{3.6}$$

where b and a are column vectors and S is a matrix. For example, for a two-port junction as shown in Fig. 3.1, the S matrix will work with two sets of inputs to generate two sets of outputs. In this case the scattering matrix will be written as in (3.7)

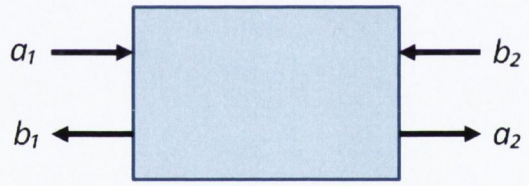

Fig. 3.1 Single two-port junction (scattering matrix).

$$\begin{bmatrix} b_1 \\ b_2 \end{bmatrix} = \begin{bmatrix} S_{11} & S_{12} \\ S_{21} & S_{22} \end{bmatrix} \begin{bmatrix} a_1 \\ a_2 \end{bmatrix}. \tag{3.7}$$

The scattering coefficients from (3.7) have physical meanings. For example, the diagonal coefficients S_{11} and S_{22} are the reflection coefficients of port 1 and 2, respectively and can be written as r_1 and r_2. The power reflection coefficients are just $|S_{11}|^2$ and $|S_{22}|^2$, respectively. The off-diagonal coefficients are the complex (amplitude and phase) outputs at one port due to the input at another. The magnitude squared of any of these scattering coefficients, $|S_{ij}|^2$, will be the fraction of power at the port i due to the power entering port j. Scattering matrices have unique properties, such as for a linear reciprocal two-port system, the scattering matrix is symmetric $S_{12} = S_{21}$. For a lossless two-port system, $|S_{11}| = |S_{22}|$ and $|S_{11}|^2 + |S_{21}|^2 = 1$.

The transmission matrix is another matrix which relates to the normalized amplitudes. The transmission matrix is used to cascade networks together and multiply them using

simple matrix multiplication. In Fig. 3.2 the demonstration of a two-port transmission matrix is shown and it is defined as (3.8)

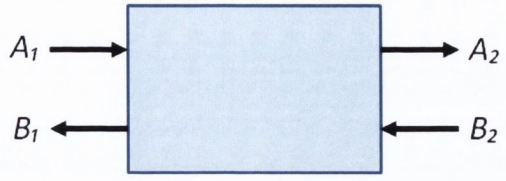

Fig. 3.2 Single two-port network (transmission matrix).

$$\begin{bmatrix} A_1 \\ B_1 \end{bmatrix} = \begin{bmatrix} T_{11} & T_{12} \\ T_{21} & T_{22} \end{bmatrix} \begin{bmatrix} A_2 \\ B_2 \end{bmatrix}, \tag{3.8}$$

where A_i is the forward-going (right) waves and B_i is the backward-going (left) waves. From Fig. 3.2 the relationship between T-matrix and S-matrix amplitudes is as follows: $A_1 = a_1$, $B_1 = b_1$, $A_2 = b_2$, $B_2 = a_2$. The relationship between the T-matrix and the S-matrix elements can be written as

$$\begin{aligned} T_{11} &= \frac{1}{S_{21}}, \quad T_{12} = -\frac{S_{22}}{S_{21}}, \\ T_{21} &= \frac{S_{11}}{S_{21}}, \quad T_{22} = -\frac{S_{11}S_{22} - S_{12}S_{21}}{S_{21}}. \end{aligned} \tag{3.9}$$

Both the transmission and the scattering matrix methods are used to analyze different waveguide structures and they can be both used for the structures in this thesis. However, a detailed comparison of these two methods is given in [2]. In this work we chose to work with the scattering matrix method due to its stable and efficient algorithm [4]. In addition, with TMM method it is not possible to determine the scattering loss [6] which is crucial for high order gratings.

3.2.1. The dielectric interface

First we will start with a simple structure such as dielectric interface shown in Fig. 3.3. The system consists of two different dielectrics with refraction indices n_1 and n_2, respectively.

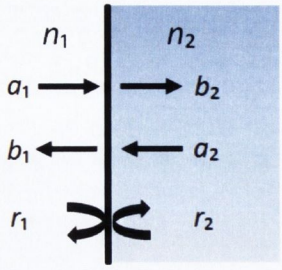

Fig. 3.3 Interface between two dielectric interfaces.

In the case shown above two reference planes are selected at the physical interface between two dielectrics with different refractive indices. Therefore, there is no scattering junction between them. We can find the scattering coefficients for this system using equation (3.5)

$$S_{11} = \frac{b_1}{a_1}\bigg|_{a_2=0} = -r_1 = \frac{n_1 - n_2}{n_1 + n_2}, \tag{3.10}$$

$$S_{22} = \frac{b_2}{a_2}\bigg|_{a_1=0} = -(-r_1), \tag{3.11}$$

$$S_{12} = S_{21} = t = \sqrt{1 - r_1^2}. \tag{3.12}$$

where r_1 and t are the reflection and transmission coefficients of incoming right (left) waves in terms of refractive indices. The system described above is considered to be a lossless system because there is no scattering junction between two dielectrics. Thereby, as it was mentioned before for a lossless two-port system, the power conservation is fulfilled and the scattering coefficients will be equal $S_{12} = S_{21}$ as shown in equation (3.12).

After defining the scattering coefficients, we can write the scattering matrix for dielectric interface in simple form as

$$S = \begin{bmatrix} -r_1 & t \\ t & r_1 \end{bmatrix}. \tag{3.13}$$

For the normal incident plane waves the transmission coefficient in terms of refractive indices can be written as follows

$$t = \frac{2\sqrt{n_1 n_2}}{n_1 + n_2}, \tag{3.14}$$

3.2.2. Transmission line with no discontinuities

Fig. 3.4 shows a network with a distance L with two reference planes and no discontinuities between them. Therefore, such a system has no scattering junctions in this transmission line.

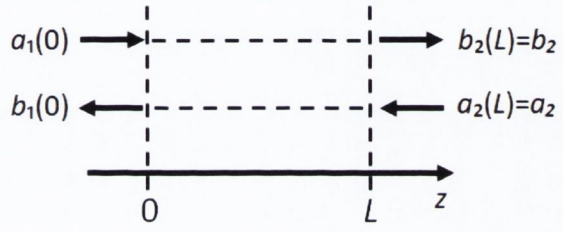

Fig. 3.4 Transmission line section of length L.

In this case the normalized amplitudes are expressed as a function of distance as shown in Fig. 3.4. Since it is a waveguide with no scattering junctions in it, there is no coupling between forward-going and backward-going waves. Therefore, $S_{11} = S_{22} = 0$. Using equation (3.2) we can write the normalized amplitudes for forward-going and backward-going waves as follows

$$b_2 = a_1(L) = a_1(0)e^{-j\tilde{\beta}L} = a_1 e^{-j\tilde{\beta}L}, \tag{3.15}$$

$$a_2 = b_1(L) = b_1(0)e^{-j\tilde{\beta}L} = b_1 e^{j\tilde{\beta}L}. \tag{3.16}$$

Using equations (3.5), (3.15) and (3.16) we will find the scattering coefficients as

$$S_{12} = \frac{b_1}{a_2} = \frac{b_1}{b_1 e^{j\tilde{\beta}L}} = e^{-j\tilde{\beta}L}, \tag{3.17}$$

$$S_{21} = \frac{b_2}{a_1} = \frac{a_1 e^{-j\tilde{\beta}L}}{a_1} = e^{-j\tilde{\beta}L}. \tag{3.18}$$

The resulting scattering matrix will be

$$S = \begin{bmatrix} 0 & e^{-j\tilde{\beta}L} \\ e^{-j\tilde{\beta}L} & 0 \end{bmatrix}. \tag{3.19}$$

From the result above propagation delay is the same for the forward and backward waves. This means that mode propagation at distance L will result in a phase shift of $-\beta L$ and a gain (loss) rate $\beta_i L$ in any direction, assuming that $\tilde{\beta} = \beta + j\beta_i$, where β is the real part of complex propagation constant and β_i is the imaginary part.

3.2.3. Dielectric segment and the Fabry-Perot etalon

Another structure is dielectric segment which is the combination of both structures together described above with another dielectric. Such a dielectric block is known as a Fabry-Perot etalon which is shown in Fig. 3.5 where a dielectric slab with refractive index n_2 separates the semi-infinite media with refractive indices n_1 and n_3. The left-hand side has the refractive index of n_1, the right-hand side region has n_3. The middle section is the dielectric block with refractive index n_2.

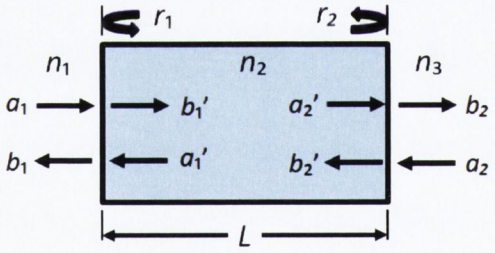

Fig. 3.5 Fabry-Perot etalon.

From the figure we can divide the structure into three scattering junctions, such as two dielectric interfaces and one transmission line. First, assuming that $a_2 = 0$, we can define the outputs b_j as following

$$\begin{aligned} b_1 &= -a_1 r_1 + a_1' t_1, \\ b_1' &= a_1 t_1 + a_1' r_1, \end{aligned} \tag{3.20}$$

$$\begin{aligned} b_2 &= a_2' t_2, \\ b_2' &= a_2' r_2. \end{aligned} \tag{3.21}$$

Also we can express

$$\begin{aligned} a_1' &= b_2' e^{-j\tilde{\beta}L}, \\ a_2' &= b_1' e^{-j\tilde{\beta}L}. \end{aligned} \tag{3.22}$$

Then we can solve the scattering coefficients

$$S_{11} = -r_1 + \frac{t_1^2 r_2 e^{-2j\tilde{\beta}L}}{1 - r_1 r_2 e^{-2j\tilde{\beta}L}}, \tag{3.23}$$

$$S_{21} = \frac{t_1 t_2 e^{-j\tilde{\beta}L}}{1 - r_1 r_2 e^{-2j\tilde{\beta}L}}. \tag{3.24}$$

Similarly, when $a_1 = 0$, the scattering coefficients will be

$$S_{22} = -r_2 + \frac{t_2^2 r_1 e^{-2j\tilde{\beta}L}}{1 - r_1 r_2 e^{-2j\tilde{\beta}L}}, \tag{3.25}$$

$$S_{12} = S_{21}. \tag{3.26}$$

The common factor of $1 - r_1 r_2 e^{-2j\tilde{\beta}L}$ gives rise to the Fabry-Perot resonances. The absolute square of scattering coefficients $|S_{11}|^2$ and $|S_{21}|^2$ give the amount of power reflected through the Fabry-Perot etalon. Using equations above we will find

$$|S_{11}|^2 = \frac{\left(r_1 - r_2 e^{2\beta_i L}\right)^2 + 4R\sin^2\beta L}{(1-R)^2 + 4R\sin^2\beta L}, \tag{3.27}$$

$$|S_{21}|^2 = \frac{(1 - r_1^2)(1 - r_2^2)e^{2\beta_i L}}{(1-R)^2 + 4R\sin^2\beta L}, \tag{3.28}$$

where $R = r_1 r_2 e^{2\beta_i L}$ and $\tilde{\beta} = \beta + j\beta_i$. If we will consider a symmetric ($r_1 = r_2$) and lossless ($\beta_i = 0$) Fabry-Perot cavity, then (3.27) and (3.28) will be written as

$$|S_{11}|^2 = \frac{4R\sin^2\beta L}{(1-R)^2 + 4R\sin^2\beta L}, \tag{3.29}$$

$$|S_{21}|^2 = \frac{(1-R)^2}{(1-R)^2 + 4R\sin^2\beta L}. \tag{3.30}$$

For a lossless case, by power conservation the power flow into the region n_2 is equal to the power flow out of this region and expressed as $|S_{11}|^2 + |S_{21}|^2 = 1$.

3.3. Gratings

Many modern laser diodes use gratings or distributed Bragg reflectors (DBR) for one or both cavity mirrors. In-plane lasers use the gratings for mode selectivity and therefore for single-mode operation. Vertical cavity lasers (VCSEL) also use gratings to achieve high reflection. Gratings consist of a periodic structure where many small reflections will add up in phase at the Bragg wavelength and the reflection coefficient will be high. If they do not add in phase then the reflection will be low. This is the main principle of the DBR laser. There are different types of gratings, such as rectangular, triangular and other shapes. The analysis of several grating shapes can be found in [7]. Here we will discuss only rectangular shaped gratings with equal space (Λ) and mark (Λ_m) as shown in Fig. 3.6. Such gratings are called first-order gratings. The schematic structure of rectangular gratings or DBR mirror with the length L_g for an in-plane laser is shown in Fig. 3.6. The net reflection from the gratings is $r_g \sim 2mr$, where m is the grating period and $2r$ is the reflection per grating step. The factor 2 is added because there are two discontinuities per grating period. In the figure there is a variation in the refractive index in periodic structure n_1 and n_2, respectively. In this case we need to take into account an effective reflectivity at each discontinuity. Therefore, the effective reflectivity from waveguide region 2 to region 1 will be approximately

$$r \approx \frac{\bar{n}_2 - \bar{n}_1}{\bar{n}_2 + \bar{n}_1}, \tag{3.31}$$

where $\bar{n}_1$ and $\bar{n}_2$ are the effective indices in waveguide region 1 and 2, respectively.

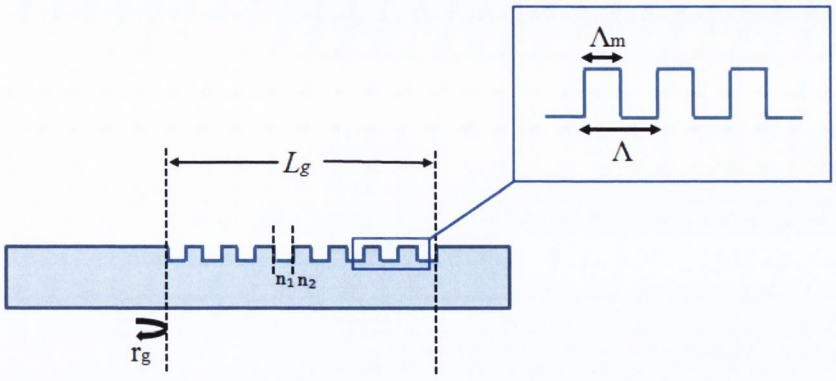

Fig. 3.6 Schematic of a DBR mirror for in-plane laser with length L_g.

When we are dealing with DBR structure we need to define an effective cavity length which is a distance shown in Fig. 3.7. From equations (3.14) and (3.15) in section 3.2.2, the propagating forward-going and backward-going waves result in a phase shift of $-\beta L_{eff}$. Hence, if the reflection phase at the Bragg wavelength is zero, then the net reflection from the grating, r_g, can be expressed as

$$r_g \approx |r_g| e^{-j(\beta-\beta_0)L_{eff}}. \tag{3.32}$$

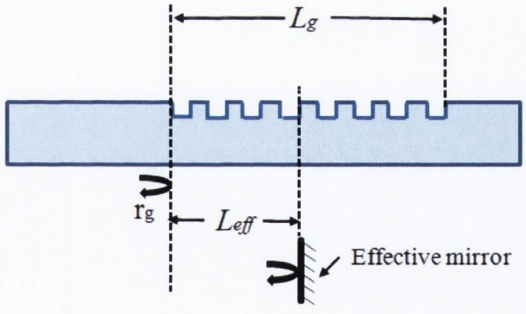

Fig. 3.7 Schematic diagram of an effective cavity length of DBR reflector.

By expanding the DBR reflection phase in a Taylor series: $j\phi \approx j\phi_0 + j(\beta - \beta_0)(\partial\phi/\partial\beta) + \cdots$, and equating the linear $(\beta - \beta_0)$ coefficient with the exponent in equation (3.32), we define the effective cavity length as in (3.33)

$$L_{eff} = -\frac{1}{2}\frac{\partial\phi}{\partial\beta}, \tag{3.33}$$

where β is the propagation constant. From equation (3.33) the effective cavity length of DBR is defined by the phase delay of reflected light normalized by the deviation of the propagation constant. From [5] and [8], for the special case when the structure is loss-less and $\beta = \beta_0$, where β_0 is Bragg propagation constant, the effective cavity length can be expressed as following

$$L_{eff} = \frac{1}{2\kappa}\tanh(\kappa L_g), \tag{3.34}$$

where κ is the coupling constant which is given by

$$\kappa L_g \equiv 2mr = \frac{m\Delta\bar{n}}{\bar{n}} = \frac{L_g}{\Lambda}\left(\frac{\Delta\bar{n}}{\bar{n}}\right), \tag{3.35}$$

where Λ is the grating period, $\Delta\bar{n} = |\bar{n}_2 - \bar{n}_1|$ and $\bar{n} = |\bar{n}_2 + \bar{n}_1|/2$ are the effective indices of waveguide region 1 and 2, respectively. From equation (3.34), for small values of $\kappa L_g \ll 1$ the effective cavity length will be

$$L_{eff} = \frac{L_g}{2}, \tag{3.36}$$

and for high values of $\kappa L_g \gg 1$ which are referred as strongly reflected gratings

$$L_{eff} = \frac{1}{2\kappa}. \tag{3.37}$$

From equation (3.37), when $\kappa L_g \gg 1$ the effective cavity length does not depend on the length of the grating section but depends on the coupling coefficient κ. This means that the effective cavity length depends on the reflectivity at the interface of the high refractive index and low refractive index regions of the waveguide as given in equation (3.35).

3.3.1. DBR and DFB lasers

In the previous section we discussed the gratings in particularly DBR mirrors. In this section we will give examples of laser diodes using periodic gratings in their structure. We will consider only in-plane lasers such as distributed Bragg reflector (DBR) laser and

distributed feedback (DFB) laser. These lasers use gratings for spectral selectivity to form single-mode lasers.

3.3.1. a. DBR laser

A distributed Bragg reflector (DBR) laser is formed by using a grating instead of cleaved facets at one or both ends of the laser structure. The schematic of DBR laser with a grating at one end is shown in Fig. 3.8. An antireflection (AR) coating is applied to suppress any reflection from the end of the grating.

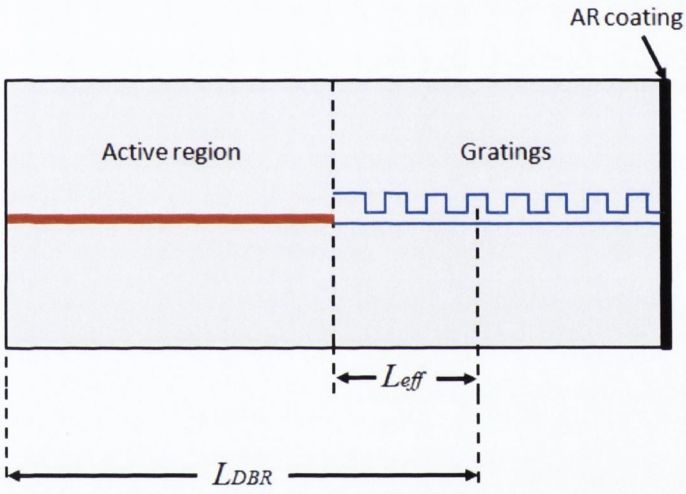

Fig. 3.8 Schematic diagram of DBR laser [8].

The structure has an active section and a passive section which is formed from the grating reflectors. The active section provides gain and the gratings provide wavelength selectivity. Because the gratings are formed along the passive waveguide section, it is important to have a good coupling of the light from the active part of the laser to the grating section. If there is a mismatch during the transition it will cause a coupling loss and undesirable reflections can occur which will interfere with the reflection from the gratings. There are several types of coupling between the active and passive sections such as the bundle integrated guide (BIG) [9] structure, the integrated twin guide structure [10] and the butt-joint (BJ) structure [11], [12]. Among them the butt-joint structure gives the best laser performance.

If the coupling is perfect and without loss, then the gain condition will be

$$R_1 R_g \exp(2 g_{net} L_a) = 1, \tag{3.38}$$

where R_1 is the power reflection from the end of the active region, R_g is the power reflection from the grating section, L_a is the length of the active region. From (3.38) the net modal gain in the active region is

$$g_{net} = \frac{1}{2L_a}\left(\ln\left(\frac{1}{R_1}\right) + \ln\left(\frac{1}{R_g}\right)\right). \tag{3.39}$$

The threshold gain, g_{th} can be found from

$$\Gamma g_{th} = \alpha_{in} + \alpha_m, \tag{3.40}$$

where Γ is the product of lateral and transverse confinement factors, α_{in} is internal loss. In general, the distributed mirrors are lossy and therefore, the mirror loss α_m is defined as

$$\alpha_m = \frac{1}{L_{DBR}} \ln\left(\frac{1}{r_1 |r_g|}\right), \tag{3.41}$$

where $|r_g|$ is the amplitude reflection of grating section and r_1 is for the mirror section. Equation (3.41) is for the effective mirror case and the cavity length is chosen to be L_{DBR} as shown in Fig. 3.8. Since the mirrors are lossy we have to define the fraction of power, F, from each end of the laser. Using the scattering parameters we will find the fraction of power for a single Bragg mirror at end 2 and a discrete mirror at end 1 as following

$$\begin{aligned} F_1 &= \frac{t_1^2}{(1 - r_1^2) + \frac{r_1}{|r_g|}\left(1 - |r_g|^2\right)}, \\ F_2 &= \frac{|t_g|^2}{\left(1 - |r_g|^2\right) + \frac{|r_g|^2}{r_1}(1 - r_1^2)}. \end{aligned} \tag{3.42}$$

where $|t_g|^2$ power transmission through the effective mirror. The output power from the end 1 is

$$P_{01} = \eta_{d1} \frac{h\nu}{q} (I - I_{th}), \tag{3.43}$$

where η_{d1} is a differential quantum efficiency which can be calculated by

$$\eta_{d1} = F_1 \eta_i \frac{\alpha_m}{\Gamma g_{th}}. \tag{3.44}$$

3.3.1. b. DFB laser

A distributed feedback (DFB) laser also uses grating mirrors, but gain is included in the gratings. In DBR lasers the active section and the gratings are separated longitudinally. In a DFB laser the gratings are formed along the entire cavity so the reflection occurs at each slope of the gratings. Therefore the optical feedback is distributed over the entire gain medium. A schematic structure of DFB laser is shown in Fig. 3.9.

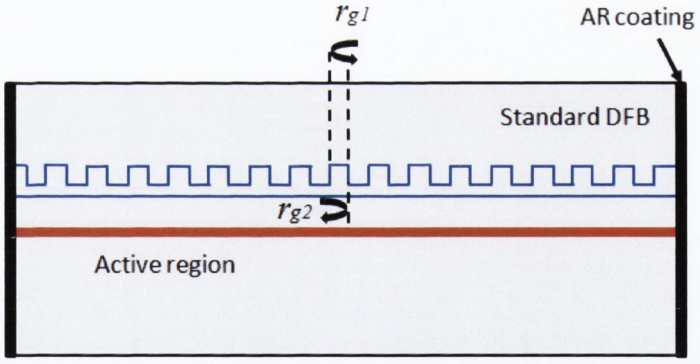

Fig. 3.9 Schematic diagram of standard DFB laser.

Fig. 3.9 shows the so-called standard DFB laser with no shift in the gratings and all periods of the gratings are the same. The active length of such structure is a quarter-wavelength long, $L_a = \lambda/4$, since we have chosen mirror reference planes as In Fig. 3.9, this will yield a zero grating reflection phase at the Bragg wavelength. Therefore, this type of DFB is anti-resonant at the Bragg wavelength. If we consider that the cavity is half a wavelength long [13], [14], $L_a = \lambda/2$ (grating pitch period ~235 nm), the device becomes resonant at the Bragg wavelength where the reflection phase is zero. Half-wavelength mirror spacing corresponds to a quarter-wavelength shift between the gratings. This type of

structure referred to as a quarter-wavelength or phase-shifted DFB laser which is shown in Fig. 3.10.

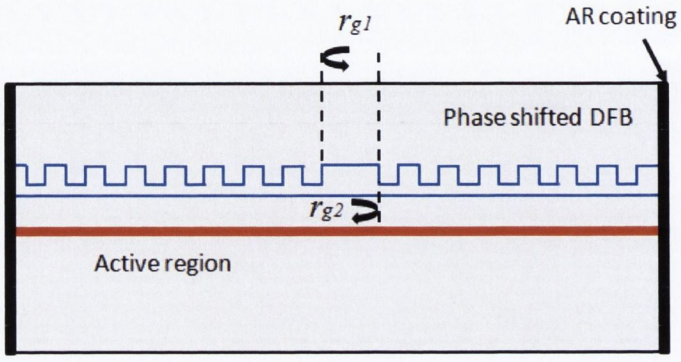

Fig. 3.10 Schematic diagram of quarter-wavelength shifted DFB laser.

The theoretical analysis of DFB laser is carried out using a transfer matrix method which is described in [8] and [15]. The transfer matrix of forward-going and backward-going waves of the grating section is given by [8]

$$F = \begin{pmatrix} \left(\cosh(\gamma L) - \frac{j\Delta\beta}{\gamma}\sinh(\gamma L)\right) & -\frac{j\kappa}{\gamma}\sinh(\gamma L) \\ \frac{j\kappa}{\gamma}\sinh(\gamma L) & \left(\cosh(\gamma L) + \frac{j\Delta\beta}{\gamma}\sinh(\gamma L)\right) \end{pmatrix}. \tag{3.45}$$

From (3.45) the oscillation condition can be presented as

$$\cosh(\gamma L) + \frac{j(\Delta\beta + jg_0)}{\gamma}\sinh(\gamma L) = 0, \tag{3.46}$$

where parameter γ is given by

$$\gamma^2 = \kappa^2 - (\Delta\beta + jg_0)^2. \tag{3.47}$$

Equation (3.46) can be written as

$$\gamma L \coth(\gamma L) = -j(\Delta\beta L + jg_0 L). \tag{3.48}$$

The solution of (3.48) gives the wavelength in terms of $\Delta\beta$ and the required gain in terms of g_0. In [5] and [8] there are shown numerical solutions of equation (3.48). From the

results, there is no propagation exactly at the Bragg wavelength $\Delta\beta L = 0$. At this exact Bragg wavelength $\Delta\beta L = 0$, (3.47) will be written as

$$\gamma^2 = \kappa^2 + g_0^2. \tag{3.49}$$

In addition, for a standard DFB laser as shown in Fig. 3.9, the results show that modes are placed symmetrically around $\Delta\beta L = 0$, which means that there are two modes at the same distance from the Bragg wavelength. Therefore, such type of DFB laser cannot work as a single-mode laser. To achieve a good single-mode operation phase-shifted DFB lasers can be used as shown in Fig. 3.10. After using the transmission matrix method (3.45), the oscillation condition for phase-shifted DFB laser is as following

$$\gamma \coth\left(\frac{\gamma L}{2}\right) + j(\Delta\beta + jg_0) = \pm\kappa. \tag{3.50}$$

The results from [5] and [8] show that there is a mode exactly at the Bragg wavelength which is dominant. Therefore, such type of DFB operates as a single-mode laser.

There is another method of achieving single-mode operation by leaving one or both facets as cleaved, rather than using AR-coatings [16]. This will destroy the unwanted degeneracy if the gratings are not too strong ($\kappa L_g \leq 1$). However, there is a yield issue due to the clevage. In practice, it is not possible to control the exact facet position relative to the grating. Thus, the reflection from the cleaved facet will have a random relative phase and the yield value will be depend on the required end loss difference [17].

3.4. Conclusion

The scattering matrix method described in this chapter will be used for our high order gratings (slots) to calculate the transmission and reflection amplitudes. The simulated results will be given in the following chapter. Since our structures have distributed mirrors, the effective mirror model will also be applied to our structures. The way to determine the effective cavity length in slotted lasers will be given in the following chapters.

References

[1] L. Li, "Multilayer modal method for diffraction gratings of arbitrary profile, depth, and permittivity," *JOSA A,* vol. 10, no. 12, pp. 2581-2591, 1993.

[2] L. Li, "Formulation and comparison of two recursive matrix algorithms for modeling layered diffraction gratings," *JOSA A,* vol. 13, no. 5, pp. 1024-1035, 1996.

[3] K. Kurokawa, "Power waves and the scattering matrix," *Microwave Theory and Techniques, IEEE Transactions on ,* vol. 13, no. 2, pp. 194-202, 1965.

[4] E. Silberstein, P. Lalanne, J. P. Hugonin and Q. Cao, "Use of grating theories in integreated optics," *JOSA A,* vol. 18, no. 11, pp. 2865-2875, 2001.

[5] L. A. Coldren and S. W. Corzine, "Mirrors and resonators for diode lasers," in *Diode lasers and photonic integrated circuits*, New York, John Wiley & Sons, 1995, pp. 65-77.

[6] S. O'Brien and E. P. O'Reilly, "Theory of improved spectral purity in index patterned Fabry-Perot lasers," *Applied Physics Letters,* vol. 86, no. 20, p. 201101, 2005.

[7] W. Streifer, D. R. Scifres and R. D. Burnham, "Coupling coefficients for distributed feedback single- and double-heterostructure diode lasers," *IEEE Journal of Quantum Electronics,* vol. 11, no. 11, pp. 867-873, 1975.

[8] M. C. Amann and J. Buus, Tunable laser diodes, Norwood: Artech House, inc., 1998.

[9] Y. Tohmori, X. Jiang, S. Arai, F. Koyama and Y. Suematsu, "Novel structure GaInAsP/InP 1.5-1.6μm bundle integrated guide (BIG) distributed Bragg reflector laser," *Japanese Journal of Applied Physics,* vol. 24, no. 6A, pp. L399-L401, 1985.

[10] K. Utaka, K. Kobayashi and Y. Suematsu, "Lasing characteristics of 1.5-1.6 GaInAsP/InP integrated twin-guide lasers with first order distributed Bragg reflectors," *IEEE Journal of Quantum Electronics,* vol. 17, no. 5, pp. 651-658, 1981.

[11] Y. Tohmori and M. Oishi, "1.5 butt-jointed distributed Bragg reflector lasers grown entirely by low-pressure MOVPE," *Japanese Journal of Applied Physics,* vol. 27, no. 4A, pp. L693-L695, 1988.

[12] J. Wallin, G. Landgren, K. Streubel, S. Nilsson and M. Oberg, "Selective area regrowth of butt-joint coupled waveguides in multi-section DBR lasers," *Journal of Crystal Growth,* vol. 124, no. 1, pp. 741-746, 1992.

[13] H. Haus and C. V. Shank, "Antisymmetric taper of distributed feedback lasers," *IEEE Journal of Quantum Electronics,* vol. 12, no. 9, pp. 532-539, 1976.

[14] K. Utaka, S. Akiba, K. Sakai and Y. Matsushima, "Analysis of quarter-wave-shifted DFB laser,"

Electronics letters, vol. 20, no. 8, pp. 326-327, 1984.

[15] N. Tessler, R. Nagar, G. Eisenstein, J. Salzman, U. Koren, G. Raybon and C. A. Burns Jr., "Distributed Bragg reflector active optical filters," *IEEE Journal of Quantum Electronics,* vol. 27, no. 8, pp. 2016-2024, 1991.

[16] S. Chinn, "Effects of mirror reflectivity in a distributed feedback laser," *IEEE Journal of Quantum Electronics,* vol. 9, pp. 574-580, 1973.

[17] J. Buus, "Dynamic single-mode operation of DFB lasers with phase shifted gratings and reflecting mirrors," *IEE Proceedings J(Optoelectronics)* , vol. 133, no. 2, pp. 163-163, 1986.

Chapter 4 – Fabry-Perot laser waveguide measurements

4.1. Fabry-Perot laser introduction

Fabry-Perot lasers are the simplest type of semiconductor lasers and can be fabricated easily now days. These lasers consist of two reflecting mirrors without mode selectivity and hence those lasers support multiple longitudinal modes. Therefore, they act as multi-mode lasers. This property is not suitable for long haul optical communication systems because of the fiber dispersion and mode stability within the laser itself. However, the FP lasers are ideal devices to investigate the material and device information such as internal loss, net modal gain, linewidth enhancement factor, injection efficiency and etc. There are different methods to find out these parameters, for instance typically the cutback method [1], which uses the relationship between the cavity length and the slope efficiency to measure the internal loss and injection efficiency is employed. The characterization of the Fabry-Perot lasers can be done using the amplified spontaneous emission (ASE) spectrum when the laser is driven below the threshold current. By measuring the gain spectra it is possible to characterize the semiconductor lasers, semiconductor optical amplifiers and waveguide devices. There have been several methods to measure the net modal gain from the ASE spectrum such as the Hakki-Paoli method [2], the method by Cassady [3], Fourier transform method [4], [5], [6] and Fourier series expansion method [7]. The Hakki-Paoli method uses the ratio of adjacent peaks and valleys of individual Fabry-Perot resonances to calculate the gain. However, the resolution of the measurement system may underestimate the gain if it is not high enough [8] and it will affect the measurement accuracy. To solve this limitation, Cassidy proposed the method which uses the ratio of the average mode intensity to the minimum intensity instead of the ratio of peaks and valleys. Therefore it is less sensitive to the measurement resolution. However, Cassidy's method is sensitive to the noise of emission spectra [9]. This will cause a problem in calculating the gain. Another method to evaluate the gain is by the Fourier transform method. In this method, the whole ASE spectrum is transformed from the wave number domain to the length domain which gives a

series of reflection peaks. Then by taking the inverse Fourier transform of two such reflection peaks and by dividing them, the gain spectrum can be obtained. The advantage of this method is that a correction can be included if the gain spectrum is influenced by the resolution bandwidth of the measured system [4]. However, the measured gain spectra have the fluctuations at the edges of the gain spectrum due to a window effect [6]. To overcome this problem, the Fourier series expansion (FSE) method can be used. It also allows an instrument response function to be included if the response function can be measured as in Fourier transform. FSE is more accurate at the edges from both sides of the wavelength range. The advantage of this method is that it can work on individual longitudinal modes of the ASE spectrum. This method was developed in our group and it has been shown that by using this method it is possible to extract different important parameters [10], [11]. In this chapter, we will use this Fourier series expansion method to characterize our FP lasers. We will basically repeat the measurements described in [11]. Using this method we will extract the following parameters: the net modal gain, internal loss, quasi-Fermi level separation, spontaneous emission factor and the linewidth enhancement factor.

The chapter is organized as follows. First, the theoretical description of the ASE will be given and the FSE method will be explained. From this method we will define the round-trip gain and net modal gain. Next from the extracted net modal gain we will calculate the internal loss and spontaneous emission factor. The last part will be calculating the linewidth enhancement factor using the extracted round trip gain.

4.2. Fourier series expansion method

4.2.1. Theoretical description of the ASE spectrum

In Chapter 2, we discussed that spontaneous emission is an incoherent emission where photons generated due to spontaneous recombination of electrons and holes as shown in Fig. 4.1. It is inherent process for all laser diodes because it is the natural way of generating the photons. Spontaneous emission affects the linewidth as was discussed in Section 2.2.3, and it also influences the number of longitudinal modes and the modulation response of a laser [12]. Therefore, it is an important process in characterizing the laser diodes.

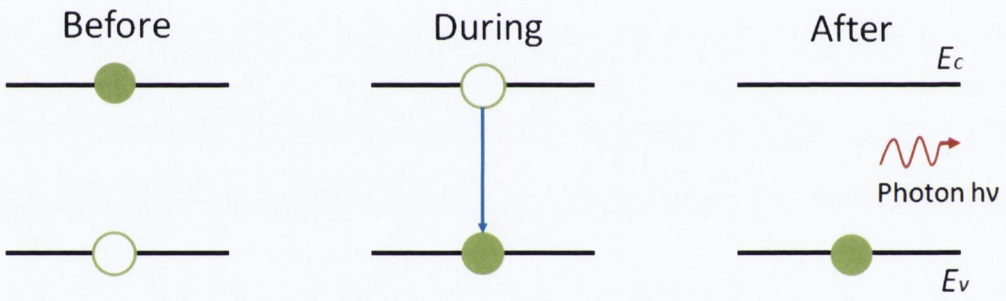

Fig. 4.1 Spontaneous emission schematic.

From [7] and [13], the amplified spontaneous emission (ASE) spectrum of a Fabry-Perot laser can be expressed by

$$I = \frac{I_{sp}(1-R)(1+b)}{1+b^2-2b\cos(2n_{eff}kL)}, \tag{4.1}$$

where $b = \exp(gL)\,R$ is the round-trip gain, g is the net modal gain; L is the cavity length; R is the power reflectivity from the end facet; $k = 2\pi/\lambda$ is the wave number in vacuum.

$$I_{sp} = \frac{S[\exp(gL)-1]}{g}, \tag{4.2}$$

is the single pass of ASE and S is the spontaneous emission coupled into the waveguide mode and can be expressed as

$$S = \frac{hc}{\lambda} r_{sp} A \beta_g, \tag{4.3}$$

where h is Plank constant, c is the speed of light, A is the cross-sectional area of the quantum well region, β_g is the geometrical spontaneous emission factor, and r_{sp} is the total spontaneous emission rate. In practice, the ASE spectrum can be measured using an optical spectrum analyzer (OSA). The measured ASE spectrum will be the convolution of the response function of the OSA $f(\lambda - \lambda')$ with the intrinsic ASE spectra $I(\lambda')$ of the FP laser which is described by (4.4).

$$I' = \int I(\lambda') f(\lambda - \lambda') d\lambda'. \tag{4.4}$$

The response function of the OSA can be found by measuring the spectrum of the external laser with the bandwidth much narrower than the resolution bandwidth of the OSA. In this case, the measured spectrum by the OSA will be

$$P_2(\lambda) = \int P_1 \delta(\lambda' - \lambda_0) f(\lambda - \lambda') d\lambda' = P_1 f(\lambda - \lambda_0), \tag{4.5}$$

where $P_1 \delta(\lambda' - \lambda_0)$ is the spectral line of the external laser and P_1 is the total power of the spectral line. From (4.5) the response function of the OSA will be

$$f(x) = \frac{P_2(\lambda - \lambda_0)}{P_1}. \tag{4.6}$$

If we will consider one longitudinal mode as shown in Fig. 4.2, the round-trip phase $\phi = 2kn_{eff}L$ varies from $-\pi$ to π, where the mode peak has a phase of 0.

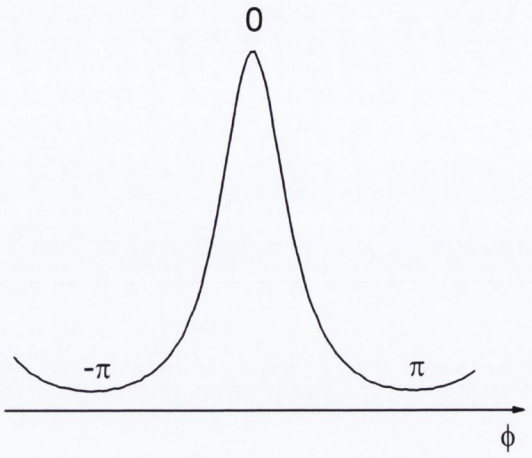

Fig. 4.2 Schematic diagram of one longitudinal mode.

By applying the FSE method to this longitudinal mode we will get the Fourier series coefficient as

$$\tilde{I}_m = \frac{1}{2\pi}\int_{-\pi}^{\pi} I(\phi)\exp(-im\phi)\,d\phi, \tag{4.7}$$

where $\tilde{I}_m$ is the m-th coefficient. The single pass of the ASE $I(\phi)$ and the round-trip gain are the slowly varying functions of the wavelength which means that they can be approximated as constants over the longitudinal mode range. Hence (4.7) can be calculated as follows

$$\tilde{I}_0 = \frac{S\,(1-R_l)(1+R_r\exp(gL))(\exp(gL)-1)}{g}\frac{1}{1-b^2}, \tag{4.8}$$

$$\tilde{I}_m = \tilde{I}_0 b^{|m|}, \tag{4.9}$$

where m is an integer. Equations (4.8) and (4.9) are the zeroth and the first harmonics, respectively. For a single longitudinal mode the wavelength range is very small and the phase can be expressed as

$$\phi = -2\pi\frac{\lambda-\lambda_l}{\Delta\lambda}, \tag{4.10}$$

where $\Delta\lambda$ is a mode spacing. Taking wave number as the argument (4.7) can be written as

$$\tilde{I}_m = \frac{1}{\Delta\lambda}\int_{\lambda_l}^{\lambda_r} I(\lambda)\exp\left(i\frac{2m\pi(\lambda-\lambda_l)}{\Delta\lambda}\right)d\lambda. \tag{4.11}$$

It was mentioned above that the measured ASE spectra is the convolution of the response function of the OSA and the intrinsic ASE spectra. Using the convolution theorem in [14], the FSE coefficients from the convoluted ASE spectra will be

$$\tilde{I}'_m = \tilde{I}_m \tilde{f}_m, \tag{4.12}$$

where

$$\tilde{f}_m = \int f(x) \exp\left(i2m\pi \frac{x}{\Delta\lambda}\right) dx\,. \tag{4.13}$$

From (4.12) and (4.13) we will get the round-trip gain of the convoluted ASE spectra from

$$b = \frac{\tilde{I}'_{m+1}}{\tilde{I}'_m} \frac{\tilde{f}_m}{\tilde{f}_{m+1}}. \tag{4.14}$$

Using the calculated round-trip gain and by knowing the facet reflectivity and the laser cavity length, we define the net modal gain as follows

$$g = \frac{\log(b) - \log\left(\sqrt{R_r R_l}\right)}{L}. \tag{4.15}$$

4.2.2. Internal loss and Quasi-Fermi level separation

To obtain these parameters we assume that the FP laser has no coatings and the reflection from both facets are identical, $R = R_l = R_r$. The power reflectivity is 0.3. The ASE spectrum of the FP laser is given by (4.1). For the zeroth harmonics and by taking its inverse Fourier transform (FT) we can obtain the spectrum as

$$I_0 = \int_{-n_{eff}L}^{n_{eff}L} \tilde{I}(z) \exp(ikz) = \frac{I_{sp}(1-R)}{1-b}. \tag{4.16}$$

By substituting the single pass ASE I_{sp} with (4.2), we will get the spontaneous emission coupled into the waveguide mode as

$$S = \frac{I_0 g(1-b)}{(1-R)(\exp(gL)-1)}. \tag{4.17}$$

The relationship between the spontaneous emission and the material gain is given in [15] and can be described as follows

$$g_m = \frac{\lambda^4}{8\pi c n^2} r_{sp} \left[1 - exp\left(\frac{hc/\lambda - \Delta F}{k_B T}\right)\right], \tag{4.18}$$

where g_m is the material gain, ΔF is the quasi-Fermi level separation, k_B is the Boltzmann constant, T is the carrier temperature, n is the refractive index of the active region and r_{sp} is the spontaneous emission factor. The material gain is related to the net modal gain through

$$g = \Gamma g_m - \alpha_{in}, \tag{4.19}$$

where Γ is the optical confinement factor and α_{in} is the internal loss. By combining equations (4.18) and (4.19) we will get

$$\begin{aligned} g(\lambda) &= C'\left(S \cdot \lambda^5 \cdot \left(1 - exp\left(\frac{hc/\lambda - \Delta F}{k_B T}\right)\right)\right) - \alpha_{in} \\ &= C' q(\lambda, \Delta F) - \alpha_{in}, \end{aligned} \tag{4.20}$$

where

$$C' = \frac{\Gamma}{8\pi h A \beta_g c^2 n^2 C}. \tag{4.21}$$

From equation (4.20) we see that the net modal gain is a linear function of $q(\lambda, x)$ as $x = \Delta F$. Therefore the quasi-Fermi level separation ΔF can be extracted as follows. Scanning x within a range the ΔF is estimated. Then for each value of x we fit the $g(\lambda) - q(\lambda)$ curve with a line $y = ax + d$, where $g(\lambda)$ is treated as y and $q(\lambda)$ is treated as x. Next we will be determining ΔF. The standard deviation D between the vector y and the vector from the linear fitting y' is calculated for each variation of ΔF as

$$D = \frac{\sum_i (y_i - y_i')^2}{\sqrt{\sum_i y_i^2}\sqrt{\sum_i y_i'^2}}. \tag{4.22}$$

The value corresponding to the minimum D gives the quasi-Fermi level separation ΔF. After determining ΔF, we can find from the same linear fit the internal loss α_{in}.

4.2.3. Geometrical spontaneous emission factor calculation

The geometrical spontaneous emission factor β_g is defined as the probability that a spontaneously emitted photon is captured by the mode of interest [12]. The geometrical spontaneous emission factor is a unit less factor. From equation (4.21) in the previous section, we can define the geometrical spontaneous emission factor as

$$\beta_g = \frac{\Gamma}{8\pi h A C'^2 c^2 n^2 C'} \tag{4.23}$$

where Γ is optical confinement factor, A is the cross sectional area of quantum well region, C is the coupling coefficient and C' is the coefficient which is extracted from the linear fitting in (4.20). To calculate β_g from (4.23) we need to know what are the optical confinement factor and the coupling coefficient. The first one can be calculated through simulations. The former can be determined using two experiments. First, we need to measure the total output power of the FP laser using a large area detector. Second, we again need to measure the output power of the laser but this time by a lensed fiber which needs to be coupled to one facet of the FP laser. The ratio of the coupled power to the total output power when the laser is driven at high currents above threshold will give the coupling coefficient.

4.2.4. Linewidth enhancement factor

The linewidth enhancement factor is the ratio between the real index change and the imaginary index change when they are affected by the carrier density. From [1] and [16] the relationship between the gain and the imaginary index expressed as

$$g = 2k_0 n_i = \frac{4\pi n_i}{\lambda}. \tag{4.24}$$

It is well known that the gain changes with the change of the injected carrier density due to the change of the refractive index at the peak energy. Because the lasing occurs around the gain peak, these changes will produce ultra-fast frequency changes of the laser emission during relaxation processes. This will increase the spectral linewidth of the laser modes and the parameter which describes this enhancement is referred as the linewidth enhancement factor α. Using (4.24) the linewidth enhancement factor can be described as follows

$$\alpha = -\frac{dn/dN}{dn_i/dN} = -\frac{4\pi}{\lambda}\frac{dn/dN}{dg/dN} = -\frac{4\pi}{\lambda q}\frac{dn}{dN}. \tag{4.25}$$

where q is used to define the differential gain.

To calculate the α factor we use the method described in [17] by measuring the ASE spectrum at two slightly different currents. From the measured ASE spectra we extract the round-trip gain at two different current levels and then calculate the linewidth enhancement factor. The round-trip gain of FP laser is calculated using FSE method described above and is given as

$$b = \frac{\tilde{I}'_{m+1}}{\tilde{I}'_m}, \tag{4.26}$$

where $\tilde{I}'_m$ is the m-th order Fourier coefficient. Since the round trip gain is obtained, the linewidth enhancement factor can be calculated by [17]

$$\alpha = -\frac{\lambda_2 - \lambda_1}{\log(\mathrm{b}_2) - \log(\mathrm{b}_1)}\frac{2\pi}{\Delta\lambda}, \tag{4.27}$$

where $\lambda_{1,2}$ are the longitudinal modes at different currents, $b_{1.2}$ are the round-trip gain at these different currents, and $\Delta\lambda$ is the mode spacing. $\lambda_2 - \lambda_1$ gives the real index change and the imaginary index change can be obtained from the net modal gain change which can be extracted from the round-trip gain $\log(\mathrm{b}_2) - \log(\mathrm{b}_1)$.

4.3. Experimental measurements

For the measurements we used a FP laser with a typical 2-μm wide ridge waveguide. The laser cavity is 590 μm. The microscope image of the FP laser is shown in Fig. 4.3. The active region consists of five compressively strained AlGaInAs quantum wells with the gain peak around 1550 nm. The laser has as-cleaved facets without any reflection coatings, therefore the power reflectivity is assumed to be around 30%.

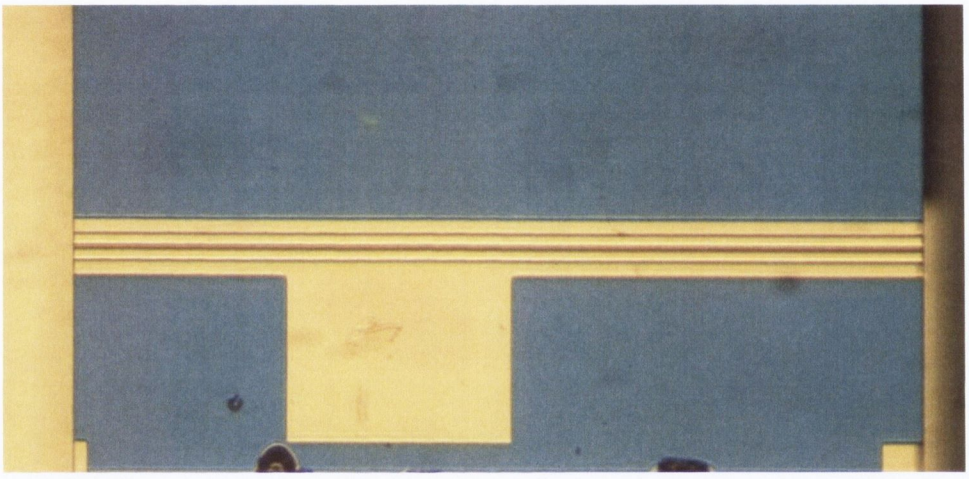

Fig. 4.3 Top view of the Fabry-Perot laser with cavity length of 590 μm.

The laser temperature was controlled through a thermoelectric cooler (TEC) and the temperature was set at 20°C. First, the laser total output power was measured using a large Ge detector. The measured $L - I$ curve is shown in Fig. 4.4. The threshold current is around 19 mA with slope efficiency of 0.16 mW/mA. Then an antireflection coated lensed fiber was used to measure the output power. This was done to measure the coupling coefficient which is around 30 % in this case.

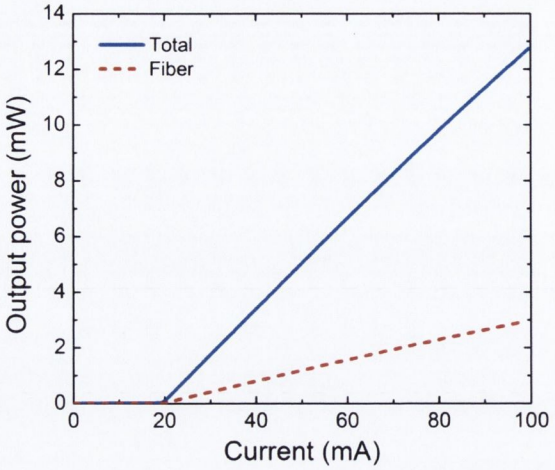

Fig. 4.4 Light-current curve $(L-I)$ of the total emitted power and fiber coupled output power of the FP laser.

We measured the ASE spectrum below threshold using the AR coated lensed fiber and an Agilent optical spectrum analyzer which has the highest resolution of 0.06 nm. First, we measured the ASE spectrum at an injection current of 18 mA for different OSA resolutions, e.g. 0.06 and 0.1 nm. In Fig. 4.5 the measured ASE spectrum for different OSA resolution is shown. It is clearly seen that when the resolution is decreased from 0.06 nm to 0.1 nm, the longitudinal mode peak power increased by about 2 dB and the valleys increased up to 2 dB. The spacing between the adjacent modes is around 0.85 nm.

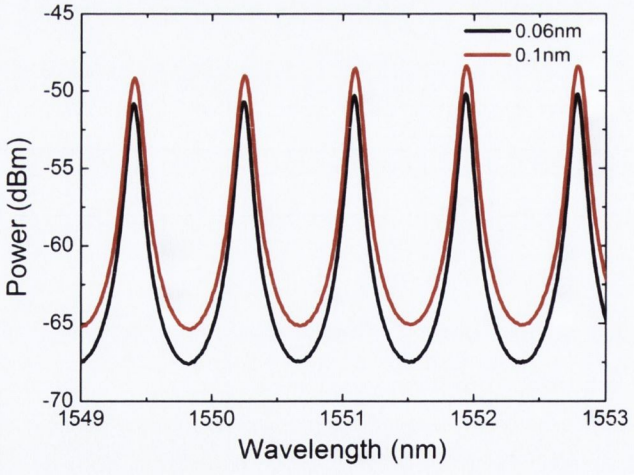

Fig. 4.5 Measured ASE spectrum for different OSA resolution as 0.06 and 0.1 nm.

The response function of the OSA is found by measuring the spectrum of an external tunable laser, in our case we used a HP laser with a spectral linewidth of around 150 kHz. This linewidth is much lower than the resolution bandwidth of the OSA which is around 7.5 GHz at the highest 0.06 nm resolution. The measured response function is shown in Fig. 4.6.

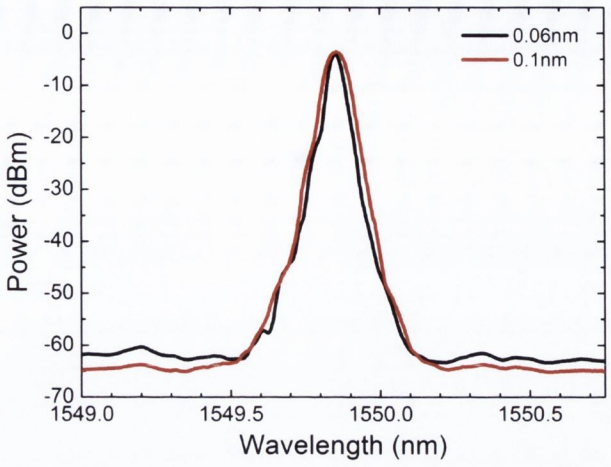

Fig. 4.6 Response functions of the OSA for different resolution settings of 0.06 and 0.1 nm.

In order to calculate the round-trip gain we need to measure the ASE spectrum of the FP laser. We measured the ASE spectrum for different currents from 16.5 to 19 mA with a step of 0.5 mA. A step of 0.5 mA was chosen so that the wavelength shift due to current injection will be lower than the mode spacing. The OSA resolution was set to 0.1 nm. In Fig. 4.7 the ASE spectrum at 18 mA is shown. The gain peak is around 1550 nm as shown in the figure.

From the measured ASE spectra we calculated the round-trip gain using the FSE method described above. In this method we included the response function of the OSA to achieve accurate results. In Fig. 4.8 the round-trip gain for different injected current values, e.g. from 16.5 to 19 mA is plotted.

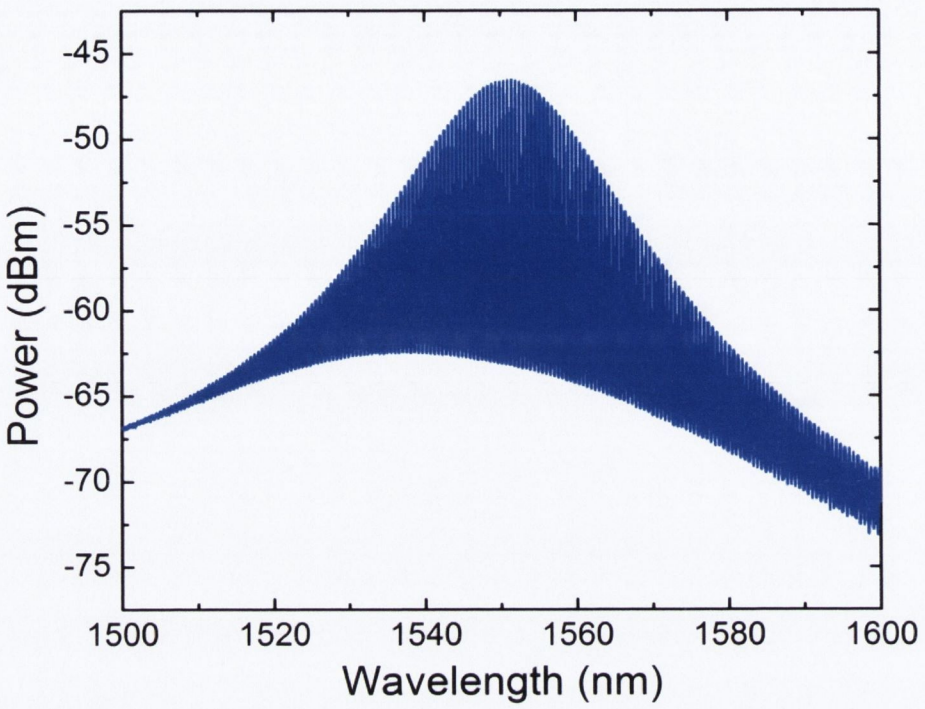

Fig. 4.7 Measured ASE spectrum of FP laser operating at 1550 nm with the OSA resolution bandwidth of 0.1 nm.

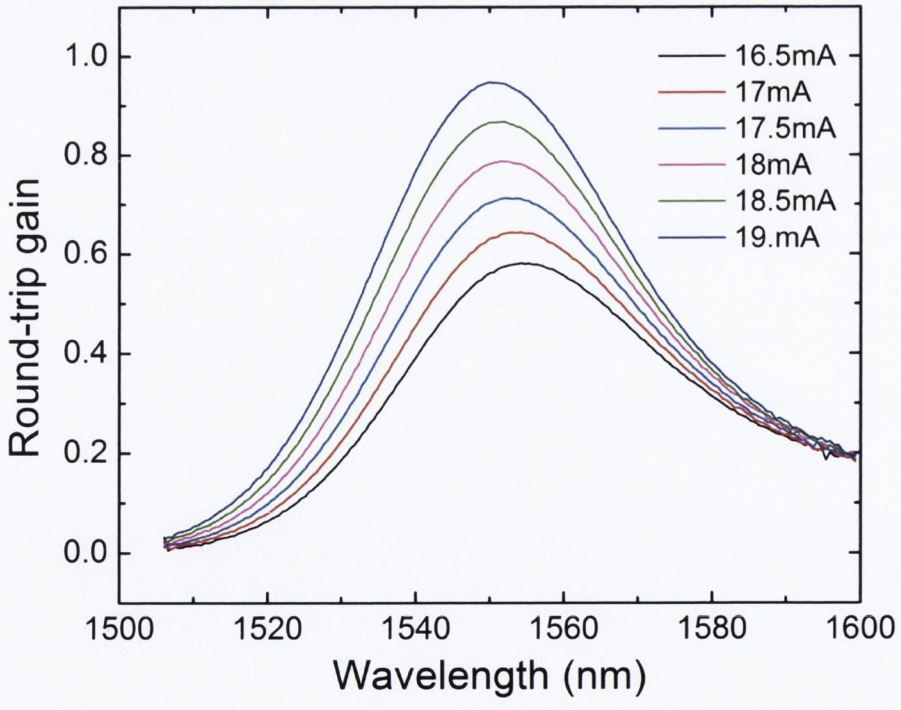

Fig. 4.8 Extracted round-trip gain with the OSA response function included for different injected current values.

Using the extracted round-trip gain and the mirror reflectivity we can then calculate the net modal gain by (4.15). Considering that the FP laser has identical mirrors on both sides, (4.15) can be written as

$$g = \frac{\log(b) - \log(R)}{L} \tag{4.28}$$

The net modal gain and the roundtrip gain are plotted in the same figure as shown in Fig. 4.9 for different current values.

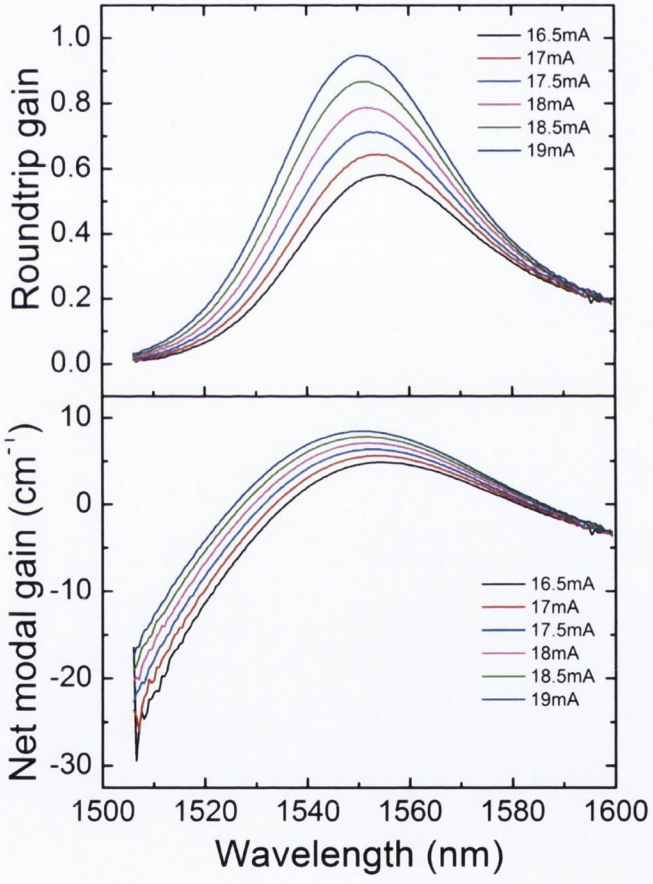

Fig. 4.9 Calculated roundtrip gain (top) and net modal gain (below) using the FSE method with the OSA response function included at different injection current values.

As we calculated the round-trip gain and the net modal gain, the next step was to calculate the spontaneous emission coupled into the waveguide which is described by (4.17). The results are shown in Fig. 4.10. From this figure it is seen that the long wavelength side of the spontaneous emission is obtained.

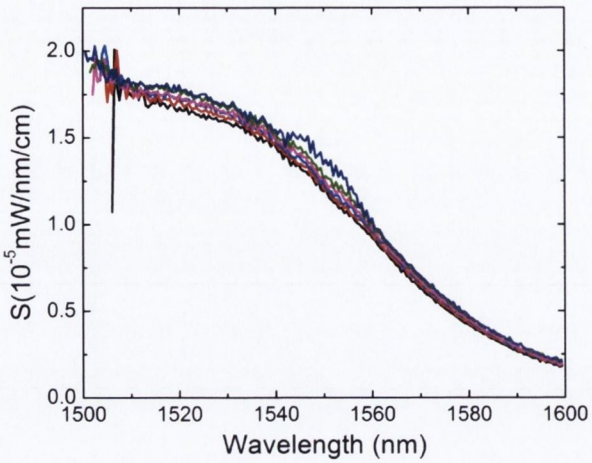

Fig. 4.10 Calculated spontaneous emission coupled into the waveguide for currents from 16.5 to 19 mA.

Equation (4.20) shows the relationship between the gain and the spontaneous emission. Based on the calculated spontaneous emission spectrum S, the spectrum of $q(\lambda, \Delta F)$ at different values of ΔF can be calculated and then the $g(\lambda) - q(\lambda)$ curve is fitted with a line as provided by equation (4.20). The fitting effect is evaluated by standard deviation as calculated from (4.22). Fig. 4.11 shows the standard deviation versus different values of ΔF for the current of 16.5 mA. The energy which corresponds to the minimum value of the standard deviation gives the estimated quasi-Fermi level separation at a specific current injection. For 16.5 mA the quasi-Fermi level separation is 0.816 eV.

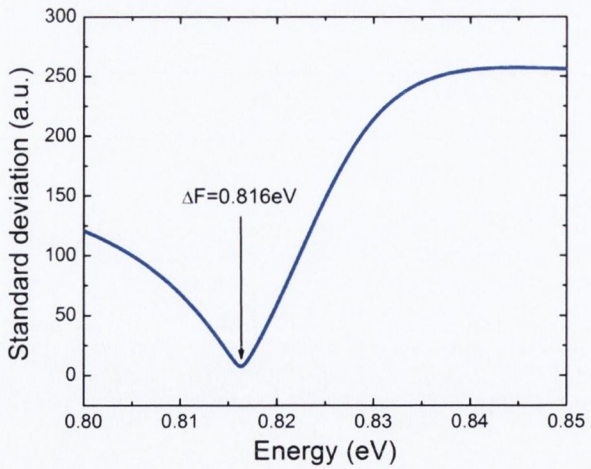

Fig. 4.11 Standard deviation from the linear fit and the original $g - q$ curve versus different values of ΔF.

At this value of ΔF, the $g - q$ curve and the linear fit are shown in Fig. 4.12. A very good linear fit has been achieved with the original data as shown in the figure. As mentioned

above from the intercept of the fitting we can determine the internal loss. The intercept from the linear fit gives the internal loss of 17.62 cm^{-1}.

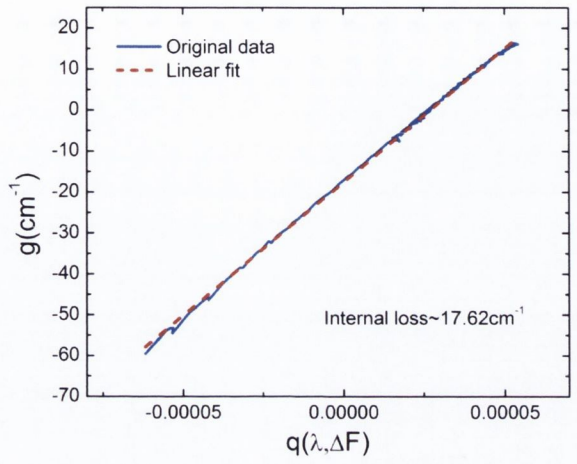

Fig. 4.12 $g - q$ curve and the linear fit when ΔF equals the estimated quasi-Fermi level separation.

We repeated the measurements above to determine the quasi-Fermi level separation and the internal loss for different injection currents. For each injection current we scanned the ASE spectrum. The quasi-Fermi level separation and the internal loss for different injection currents are shown in Fig. 4.13. The quasi-Fermi level separation increases gradually with the injection current up to 19 mA. The internal loss varies around 18 cm^{-1} for all different injected currents.

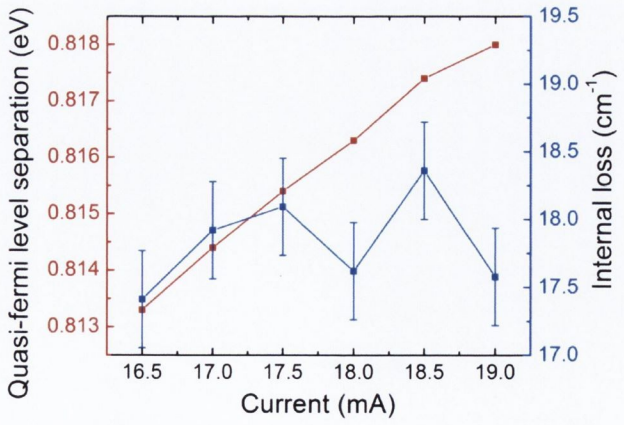

Fig.4.13 Extracted quasi-Fermi level separations and internal losses for different injected current values.

From the linear fitting we extracted the coefficient C' which is close to 600 $mW^{-1}\,\mu m^{-1}$. By using this coefficient, the geometrical spontaneous emission factor can be calculated through equation (4.23). The optical confinement factor Γ is calculated to be around 5%, so

each quantum well containing 1%. The cross-sectional area of the quantum well region is $2.5 \times 0.006 \times 5 = 0.075\mu m^2$. The resulted geometrical spontaneous emission factor is shown in Fig. 4.14. The geometrical spontaneous emission factor is dimensionless and it is around 0.000174 for different injected currents. This value is typical of experimental values for most in-plane lasers [1].

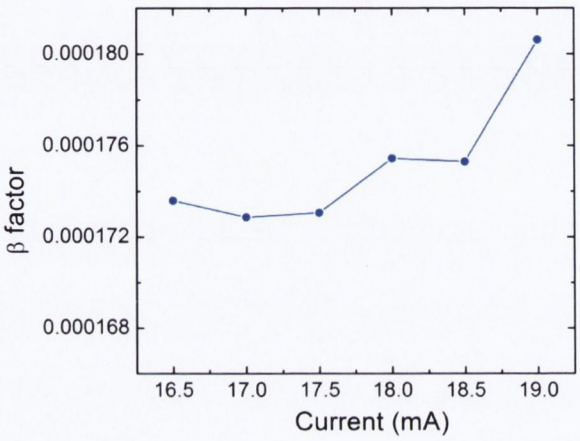

Fig. 4.14 The geometrical spontaneous emission factor versus injected current.

The last parameter to extract is the linewidth enhancement factor. As we discussed in section 4.1.4 we extract the LWEF from the round-trip gain for two slightly different injection currents. The linewidth enhancement factor is calculated from the ASE spectra recorded at 16.5 and 17 mA using equation (4.27). Fig. 4.15 shows calculated results for two different injection currents. The dashed line is the averaged result. For the AlGaInAs quantum well system, the LWEF is around 3 at the gain peak.

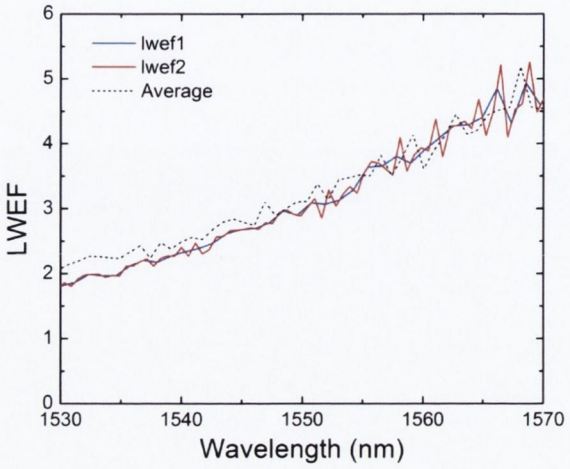

Fig. 4.15 Calculated the linewidth enhancement factor for injection currents of 16.5 and 17 mA.

4.4. Conclusion

In this chapter we characterized the Fabry-Perot laser with a cavity length of 590 μm. For characterization the amplified spontaneous emission spectrum was used when the FP laser was biased below threshold current. The Fourier series expansion method was used to obtain the parameters such as net modal gain, geometrical spontaneous emission factor, quasi-Fermi level separation and linewidth enhancement factor. The FSE method gives high accuracy measurements of the internal loss and the quasi-Fermi level separation. This was done by using deconvolution process from the response function of the measurement system which calculates the net modal gain with high accuracy even if the resolution bandwidth of the measurement system is low. From the experiments we calculated the internal loss of the FP laser to be around 18 cm^{-1}. Another important parameter which is extracted by the FSE method is the linewidth enhancement factor which is important in characterizing single mode and tunable lasers. The linewidth enhancement factor of the FP laser in this work is around 3 at 1550 nm. The ASE spectrum is an important tool in evaluating a laser performance. This method described here will be useful in characterization of slotted single mode lasers and laser arrays which will be discussed in the following chapters.

References

[1] L. A. Coldren and S. W. Corzine, Diode lasers and photonic integrated circuits, New-York: John Wiley & Sons, Inc., 1995.

[2] B. W. Hakki and T. L. Paoli, "Gain spectra in GaAs double-heterostructure injection lasers," *J. Appl. Phys.*, vol. 46, no. 3, pp. 1299-1305, 1975.

[3] D. T. Cassidy, "Technique for measurement of the gain spectra of semiconductor laser diodes," *J. Appl. Phys.*, vol. 56, no. 11, pp. 3096-3099, 1984.

[4] W. H. Guo, Q. Y. Lu, C. L. Han and L. J. Yu, "Measurement of gain for Fabry-Perot semiconductor lasers by the Fourier transform method with a deconvolution porcess," *IEEE J. Quantum Electronics*, vol. 39, no. 6, pp. 716-721, 2003.

[5] K. G. Gan and J. E. Bowers, "Measurement of gain, group index, group velocity dispersion, and linewidth enhancement factor of an InGaN multiple quantum well laser diode," *IEEE Photonic*

Technology Letters , vol. 15, no. 5, pp. 1256-1258, 2004.

[6] D. Hofstetter and J. Faist, "Measurement of semiconductor laser gain and dispersion curves utilizing Fourier transforms of the emission spectra," *IEEE Photonic Technology Letters,* vol. 11, no. 11, pp. 1372-1374, 1999.

[7] W. H. Guo, Q. Y. Lu, Y. Z. Huang and L. J. Yu, "Fourier series expansion method for gain measurement from amplified spontaenous emission spectra of Fabry-Perot semicondcutor lasers," *IEEE Journal of Quantum Electronics,* vol. 40, no. 2, pp. 123-129, 2004.

[8] L. A. Lam Sin Cho, P. M. Smowton and B. Thomas, "Spectral gain measurements of semiconudctor laser diodes," *IEE Proceedings* , vol. 137, no. 1, pp. 64-68, 1990.

[9] J. V, "Gain measurements of semiconductor laser diodes: Requirements for the wavelength resolution and sensitivity to noise," *IEE Proc. Optoelectron.* , vol. 141, no. 1, pp. 13-15, 1994.

[10] D. Byrne, W. H. Guo, R. Phelan, Q. Y. Lu, J. F. Donegan and B. Corbett, "Measurement of linewidth enhancement factors for InGaAlAs laser diode by Fourier series expansion method," *Electronics Letters,* vol. 43, pp. 1145-1145, 2007.

[11] W. H. Guo, D. Byrne, Q. Y. Lu, B. Corbett and J. F. Donegan, "Fabry-Perot laser characterization based on the amplified spontaenous emission spectrum and the Fourier series expansion method," *IEEE Journal of Selected Topics in Quantum Electronics,* vol. 17, no. 5, pp. 1356-1363, 2011.

[12] D. T. Cassidy, "Spontaenous emission factor of semiconductor diode lasers," *J. Opt. Soc. Am. B* , vol. 8, pp. 747-752, 1991.

[13] C. S. Chang, S. L. Chuang, j. R. Minch, W. W. Fang, Y. K. Chen and T. Tanbun-Ek, "Amplified spontaneous emission spectroscopy in strained quantum-well lasers," *IEEE Journal of Selected Topics in Quantum Electronics,* vol. 1, no. 4, pp. 1100-1107, 1995.

[14] R. N. Bracewell, The Fourier Transform and Its Applications, New-York: McGraw-Hill, 1978.

[15] J. Minch, S. H. Park, T. Keating and S. L. Chuang, "Theory and experiment of $In_{1-x}Ga_xAs_yP_{1-y}$ and $In_{1-x-y}Ga_xAl_yAs$ long-wavelength strained quantum-well lasers," *IEEE Journal of Quantum Electronics* , vol. 35, no. 5, pp. 771-782, 1999.

[16] M. C. Amann and J. Buus, Tunable Laser Diodes, Norwood, MA: Artech House, Inc, 1998.

[17] C. A. Green, N. K. Dutta and W. Watson, "Linewidth enhancement factor in InGaAsP/InP multiple quantum well lasers," *Applied Physics Letters* , vol. 50, no. 20, pp. 1409-1410, 1987.

Chapter 5 – Slotted single-mode lasers

5.1. Introduction to slotted single mode lasers

Single mode semiconductor lasers are key components in wavelength-division-multiplexing (WDM) systems used in local area network (LAN) and in coherent communication systems because of their stable single mode operation over a wide temperature range. Distributed feedback (DFB) and distributed Bragg reflector (DBR) lasers achieved great success in terms of good performance and reliability. However, generally the fabrication of DFB and DBR lasers requires regrowth of additional material on top of the gratings [1], [2]. This leads to special requirements in order to preserve the grating during the regrowth which will cause complex fabrication and lower yield. Recent advances in dry etching technology have simplified the fabrication of DFB and DBR laser structures. For example, laterally coupled DFB lasers [3], [4]where lateral gratings are etched on the surface of the ridge enable a regrowth free process. Surface-grating distributed Bragg reflector (SG-DBR) lasers also need a single growth step [5]. However, these types of lasers usually need electron beam (e-beam) lithography to pattern the gratings. It is well known that e-beam lithography is time consuming and quite an expensive process in comparison for instance with standard photolithography. So it is desirable to have simple fabrication and high yield.

There is another way to achieve a single mode laser without using a regrowth process. Single mode operation can be obtained by positioning reflective defects (features) or slots into a conventional Fabry-Perot (FP) laser cavity [6]. These defects manipulate the FP cavity mirror loss spectrum by enhancing one FP mode and suppressing the others and therefore single mode emission can be achieved [7]. The authors call them discrete mode (DM) lasers. The schematic of such a laser is shown in Fig. 5.1. The researchers achieved good single mode operation with high side mode suppression ratio (SMSR) more than 40 dB and narrow linewidth [8], [9]. But these types of lasers cannot be monolithically integrated with other photonic components because of the need to cleave both facets to form the mirrors for the fundamental FP cavity. Therefore, to be independent of cleavage of both facets it is possible to etch multiple distributed slots into the ridge to obtain sufficient reflection for lasing.

These are what we call slotted single mode lasers. The slots act as a distributed mirror and produce modulation of the reflection and transmission spectra which will be dependent on slot parameters such as slot width, depth, spacing and number. For this, the slot parameters should be optimized which will be discussed in section 5.2.1. In this case there is no need to cleave both facets, hence such a laser can be monolithically integrated with other photonic components. This will be demonstrated in section 5.3.3. In this chapter, we will discuss the design and fabrication of slotted single mode lasers. Afterwards, the basic characterization of laser diodes and detailed linewidth characterization will be presented.

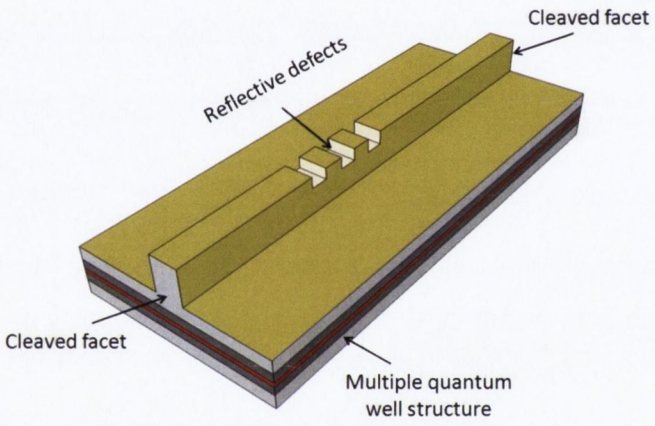

Fig. 5.1 Schematic view of discrete mode (DM) laser. DM lasers have many slots in their structure. The schematic is a simplified version.

5.2. Design and fabrication

5.2.1. Numerical simulations

The schematic structure of slotted single mode laser is shown in Fig. 5.2. The laser has a 2 μm wide ridge. The active layer consists of five AlGaInAs quantum wells with a photoluminescence (PL) peak near 1530 nm. One side of the laser has uniformly distributed multiple slots which act as a Bragg reflector of the laser. The other side consists of a straight waveguide and to have enough reflection, the back side of the laser must be cleaved. The front side of the laser is curved to 7 degrees from the normal of the cleaved facet, which reduces any reflection back from the facet, hence it removes the influence of the FP cavity and as we will see later makes the laser integrable with other photonic devices. To minimize the threshold current and increase output power anti-reflection (AR) and high-reflection (HR) coatings should be applied to the front and back facets, respectively.

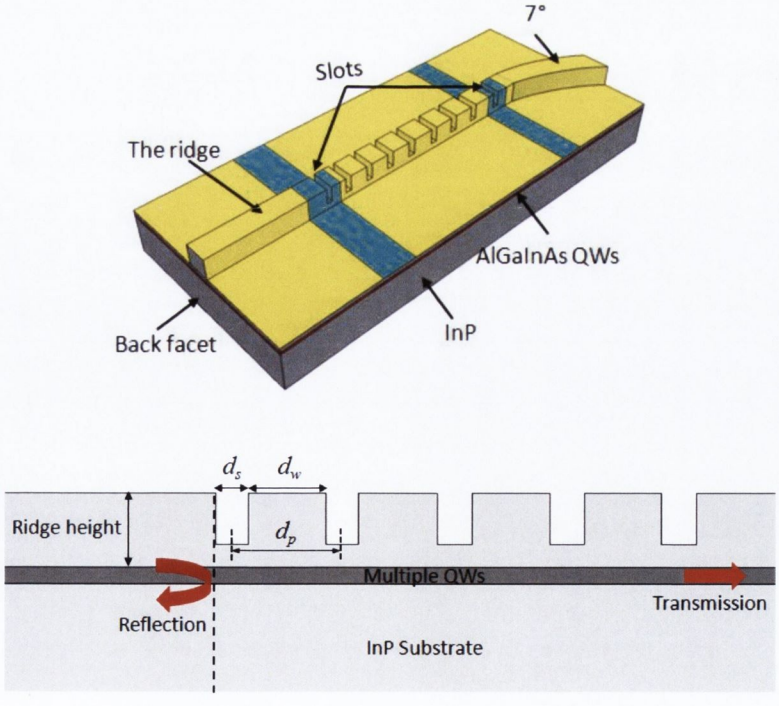

Fig. 5.2 Top: 3-D schematic structure of single mode slotted laser. Bottom: Simplified 2-D waveguide structure, where d_s is the slot width, d_w is the slot spacing and d_p is the slot period.

The laser reflection is dependent on slot reflectivity, so the slot parameters such as slot width, depth, period and number which are depicted in the bottom of Fig. 5.2 should be optimized. To achieve this we used the 2D scattering matrix method (SMM) [10] described in Chapter 3. For generality, a multiple slot structure was chosen and the structure was broken down into N uniform sections. Then 2D SMM method was used to calculate reflection and transmission of a group of slots. Initially 20 slots were taken with uniform period to analyze how the slot width and spacing will affect the reflection and transmission. Three slot depths of 1.0 μm, 1.35 μm and 1.6 μm from shallow to deep were considered. In the simulation the slot width and slot spacing are defined as

$$d_s = \frac{(2p+1)\lambda_B}{4n_s}, \tag{5.1}$$

$$d_w = \frac{(2q+1)\lambda_B}{4n_w}, \tag{5.2}$$

where p and q are integers, λ_B is Bragg wavelength, n_s and n_w are effective index of slot region and waveguide region. The Bragg wavelength was set to 1550 nm. We defined the slot width to be around 1 μm which makes it suitable for standard photolithography for patterning the slots. By defining slot width and slot depth we calculated amplitude reflection which is given in Fig. 5.3. The red color shows high reflection peaks and the blue color shows low reflection peaks. The idea is to find high reflection peaks as a function of slot width and spacing for different slot depths. The contour plot shows that slot width and spacing have a strong effect on the reflection. It is seen that when slot width is around 1.1 μm there are high reflection peaks for all three different depths. The deeper slots need a larger spacing to maximize the reflection and for example for a slot depth 1.35 μm with slot width 1.1 μm the slot spacing will be around 7.87 μm which makes the slot section act as a very high order surface grating (37th order). The grating order m was calculated by:

$$d_p = \frac{m\lambda_B}{2n_{eff}}, \tag{5.3}$$

where d_p is the slot period which is depicted in Fig. 5.2 and it is set to be 8.96 μm in our design, n_{eff} is the average effective refractive index in the waveguide structure which is 3.2.

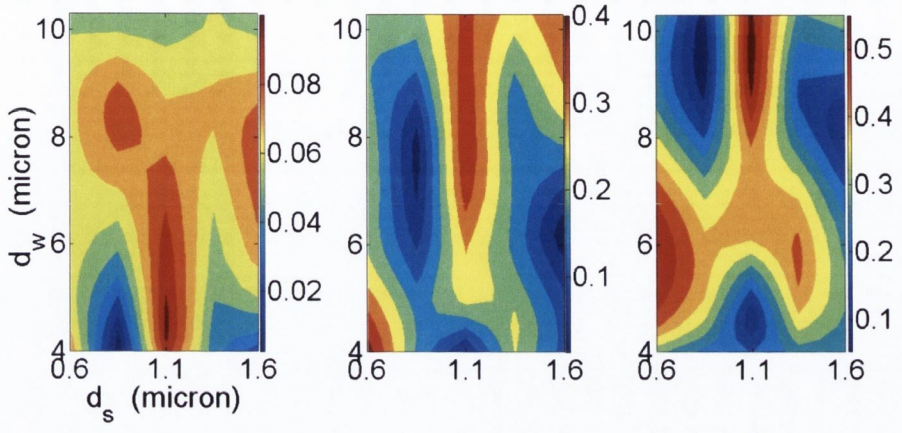

Fig. 5.3 Contour plot of simulated amplitude reflection versus slot width and spacing for 20 slots with the slot depth of (a) 1.0, (b) 1.35, (c) 1.6 μm.

The next step was to determine the slot number. It is obvious that by increasing the slot number a high reflection can be achieved but the transmission will decrease due to the losses from each slot. Because we are dealing with high-order gratings (37^{th} order), a radiation loss occurs. When a guided wave propagates through the grating structure, there will exist a coupling between propagating guided wave and an exact the same contradirectional wave. If the mark and period of the gratings are equal, then the coupling between these two waves will be strong. However, if the mark and period of the gratings will be unequal (high-order gratings), the propagating guided waves will interact with nonguided waves, which somewhat radiate away. It will lead to a radiation loss of the guided waves. So there will be a tradeoff between getting enough reflection and having a good transmission. In Fig. 5.4 the calculated amplitude reflection and transmission of the group of slots versus the slot number is shown. The reflection for deep slots saturates with slot number increase because of the large scattering loss. So for slot depth 1.6 μm the reflection saturates when the slot number is 10 but the transmission continuous to drop while slot number increases. For shallow slots, i.e the slot depth of 1.0 μm, the reflection is weak hence a large number of slots is needed to provide enough reflection for lasing. This will lead to a long laser cavity which results in high threshold. For the slot depth of 1.35 μm,

24 slots give an amplitude reflection of around 0.43 and a transmission of 0.4 as shown in Fig. 5.4.

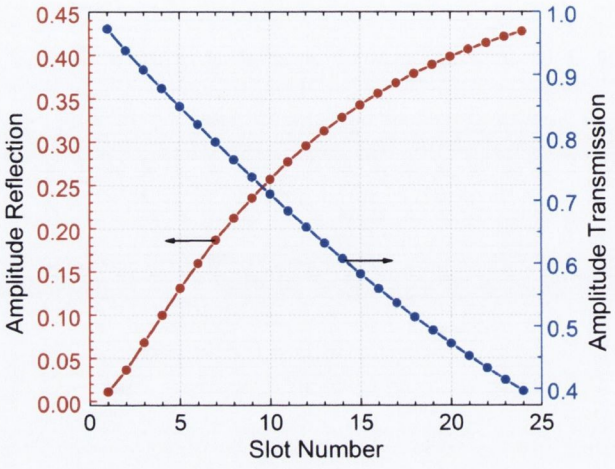

Fig. 5.4 Calculated amplitude reflection and transmission as a function of slot number for slot depth of 1.35 μm.

To achieve good single mode operation with high SMSR it is also required to have relatively narrow reflection spectrum. In Fig. 5.5 the 3-dB bandwidth of the reflection spectrum as a function of slot number for different slot depths is shown. It is clearly seen that for a slot depth of 1.6 μm the reflection spectrum is broad and is around 4 nm. This will lead to a poor SMSR. For a slot depth of 1.35 μm and when the slot number is between 20 and 30, the reflection bandwidth is below 3 nm which will cover two to three longitudinal modes of a standard FP laser with cavity length around 300 μm.

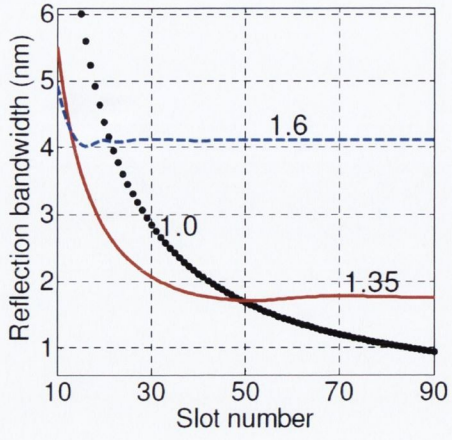

Fig. 5.5 Calculated bandwidth of reflection peaks from a group of slots with the slot depth 1.0, 1.35 and 1.6 μm versus the slot number.

By taking into account the analysis above, the slots are optimized with slot number of 24 and slot depth of 1.35 μm. This optimization gives high enough reflection and narrow reflection bandwidth while also resulting in a short cavity length which leads to a lower laser threshold.

5.2.2. Fabrication process

The epitaxial structure of the laser is based on a standard 1550 nm LD design. We used standard commercial wafer (IQE Ltd, UK). The active region of the laser consists of five AlGaInAs quantum wells with photoluminescence peak (PL) centered at 1530 nm. Above it are a 1.6 μm-thick p-doped InP layer, a 50 nm-thick p-doped InGaAsP layer, and a 200 nm-thick InGaAs contact layer. The full wafer stack layer of the material is given in Table 5.1.

Layer	Material	Group	Repeat	Mole Fraction (x)	Mole Fraction (y)	Strain (ppm)	PL (nm)	Thickness (μm)	Dopant	Type	CV Level (cm^{-3})
16	GaIn(x)As			0.530		0		0.2000	Zinc	P	> 1.50E19
15	GaIn(x)As(y)P			0.710	0.620	0	1300 +/-50	0.0500	Zinc	P	> 3.00E18
14	InP							0.1000	Zinc	P	> 1.50E18
13	InP							1.5000	Zinc	P	= 1.00E18
12	GaIn(x)As(y)P			0.850	0.330	0	1100 +/-20	0.0200	Zinc	P	= 1.00E18
11	InP							0.0500	Zinc	P	= 7.00E17
10	[Al(x)Ga]In(y)As			0.900	0.530	0		0.0600	Zinc	P	= 4.00E17
9	[Al(x)Ga]In(y)As			0.720 to 0.900	0.530	0		0.0600	Undoped	U/D	
8	[Al(x)Ga]In(y)As			0.440	0.490	-3000	1100 +/-20	0.0100	Undoped	U/D	
7	[Al(x)Ga]In(y)As	1	5	0.240	0.710	12000	1530	0.0060	Undoped	U/D	
6	[Al(x)Ga]In(y)As	1	5	0.440	0.490	-3000	1100 +/-20	0.0100	Undoped	U/D	
5	[Al(x)Ga]In(y)As			0.900 to 0.720	0.530	0		0.0600	Undoped	U/D	
4	[Al(x)Ga]In(y)As			0.900	0.530	0		0.0600	Silicon	N	= 1.00E18
3	[Al(x)Ga]In(y)As			0.860 to 0.900	0.530	0		0.0100	Silicon	N	= 1.00E18
2	InP							0.5000	Silicon	N	= 1.00E18
1	InP							0.3000	Silicon	N	= 3.00E18
SUBSTRATE											

Table 5.1 The wafer structure specifications of a standard 1550 nm LD design.

For the first fabrication run e-beam lithography was used to pattern the slots. Then two steps of inductively coupled plasma (ICP) based dry etching with Cl_2/N_2 gas combination were used to form the ridge and the slots as shown in Fig. 5.6.

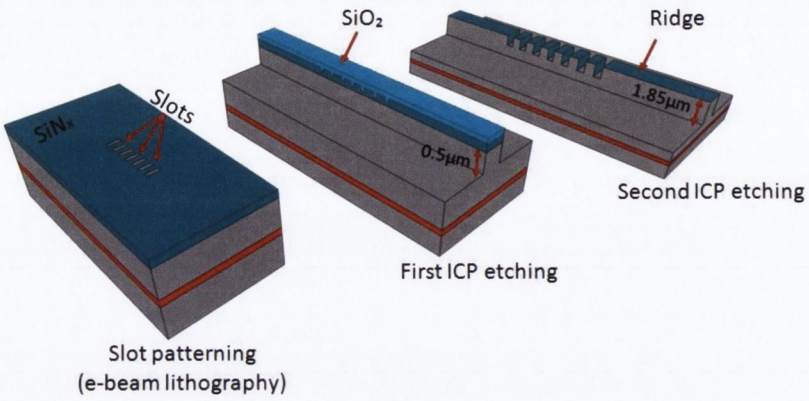

Fig. 5.6 Schematic of fabrication process.

First a silicon nitride (SiN) layer was deposited using a plasma enhanced chemical vapor deposition process (PECVD). Then slots and the alignment marks were defined using e-beam lithography. After the SiN layer was etched using hard dry etch process, a silicon dioxide (SiO_2) was deposited to protect the slot area during the dry etching process. The next step was an ICP dry etching process. First the target etch depth was 0.5 μm (+/-30 nm) to form the ridge and the slots. Then the SiO_2 layer was selectively removed to start the second dry etching process to etch the ridge. The ridge was etched to a depth of 1.85 μm (+/-30 nm). The slot was about 0.5 μm shallower than the ridge as was determined by this two step dry etching process. After completing the dry etching process, the ridge was passivated by depositing an SiO_2 contact layer by PECVD. Then, the ridge was p-metal deposited and the metal was lift off. Finally, the laser bars were cleaved and mounted on carriers. The microscope images of the slotted lasers are shown in Fig. 5.7. The image on left hand side of Fig. 5.7 is a laser bar with 7 lasers in it. The last laser is a Fabry-Perot laser. The lasers are mounted on a Si carrier. The image on right hand side of Fig. 5.7 represents a single laser.

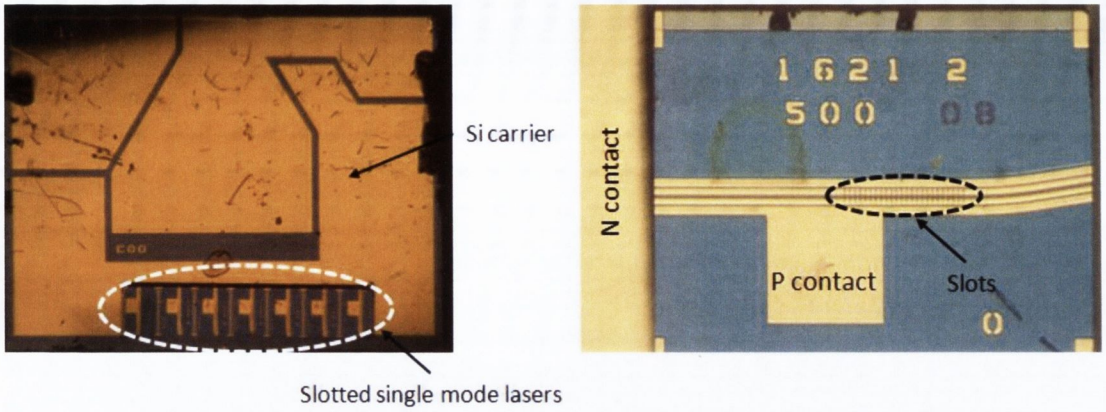

Fig. 5.7 Left: The image of a laser bar. Right: The image of a single laser.

In Fig. 5.8 (left) and (right) are depicted SEM images of fabricated devices with the ridge and single slot, respectively. There are some issues with fabrication as shown in these images. There is some residue left on InP walls beside the slots which might affect to the loss from the slots. However, the four corners of etched slot are quite sharp as shown in Fig. 5.8 (right).

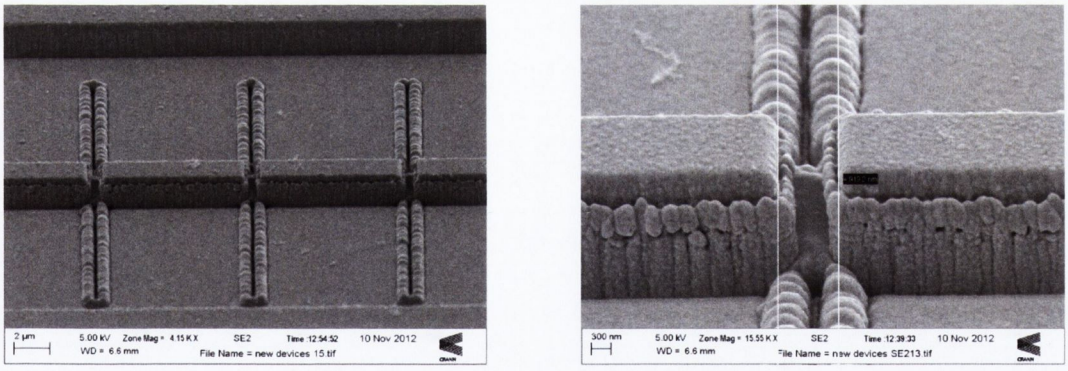

Fig. 5.8 SEM image of (left) ridge and group of slots; (right) a single slot.

We designed lasers with different cavity length, i.e. 550, 650 and 750 μm for detailed characterization. So for the 650 μm laser, the laser consists of a long section without slots which is 235 μm, the 215 μm slotted section and the 200 μm long curved and angled front section. The penetration length of the laser is defined through:

$$L_{pen} = (N-1)d_p/2, \tag{5.4}$$

N is a slot number which is 24, d_p is a slot period which is in our case 8.96 μm. From this we defined a penetration length to be 103 μm. The penetration length is needed to find out what is the effective cavity length of our laser. The effective cavity length is the length without slots plus penetration length and this is shown in Fig. 5.9. From the above calculations, the effective length, L_{eff} is around 340 μm for a laser with total cavity length of 650 μm. Therefore the bandwidth of the reflection peak covers 3 longitudinal modes of the laser to obtain single mode operation.

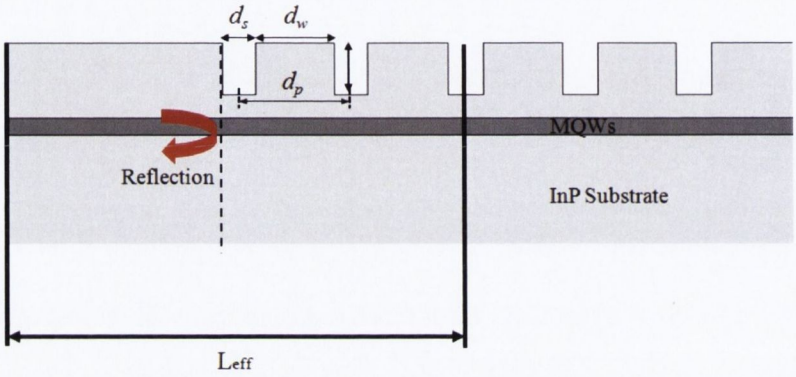

Fig. 5.9 2D schematic of the waveguide with slots.

5.3. Basic characterization

5.3.1. Power-current and current-voltage characteristics

The fabricated lasers were tested under continuous wave (CW) operation at room temperature. The measurement setup to measure power-current $(L-I)$ and voltage-current $(V-I)$ curves is shown in Fig. 5.10.

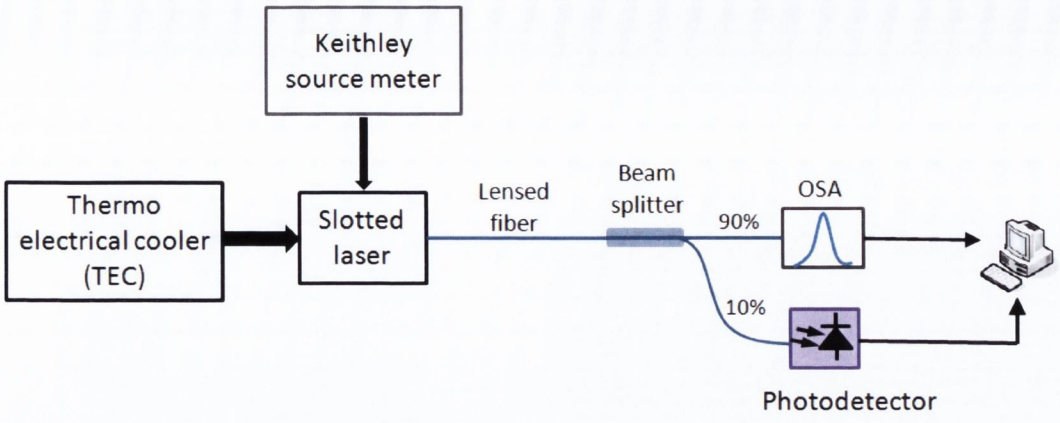

Fig. 5.10 Experimental setup for laser characterization.

The slotted laser is placed on a copper heat sink and the temperature of the chip was controlled by a thermoelectric cooling (TEC) controller. The temperature was set to 25°C. The slotted laser was driven by a Keithley 2400-C current source meter. Then the light was coupled to an antireflection coated lensed fiber. The lensed fiber has a focal spot which has a Gaussian profile and has a diameter ($1/e^2$) of 5 μm. Afterwards, the light was split into two paths by a beam splitter. 90% goes to an optical spectrum analyzer (OSA) to analyze the spectrum of the laser. The OSA resolution was set at 0.06 nm with sensitivity of -80 dBm. 10% of the light goes to a photodetector to monitor the coupling power. Finally, the data was collected by Lab View software.

The most common characteristics of the laser diode is the $(L-I)$ curve to determine the laser total output power and threshold current. To measure the total output power we used a calibrated large area (5 mm × 5 mm) Ge detector. First as-cleaved lasers or in other words lasers without coating were measured. The total cavity length is 650 μm and the slot width is 0.9 μm in the first laser. The measured $L-I$ and $V-I$ curves are shown in Fig. 5.11. The laser exhibits a threshold current (I_{th}) of about 32 mA corresponding to threshold current density (J_{th}) of 2.5 kA/cm^2. The output power of the laser was 8 mW at 100 mA corresponding to slope efficiency of around 0.12 mW/mA. The voltage drop is around 1.5 V at 100 mA.

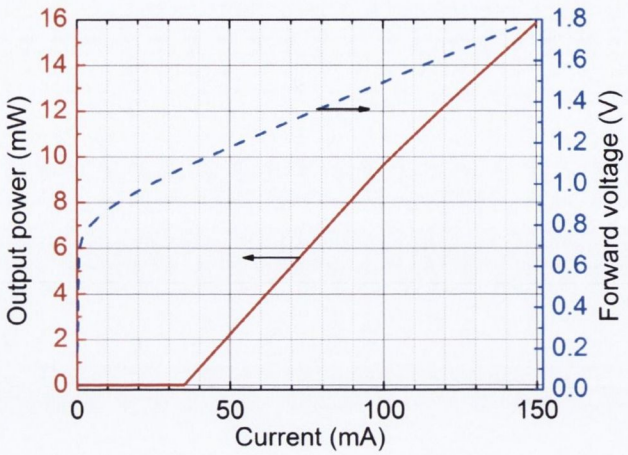

Fig. 5.11 Measured light-current ($L-I$) and current-voltage ($V-I$) curves at 25°C under CW condition.

To achieve better performance in terms of threshold current and output power, high reflection (HR) and antireflection (AR) coated films were applied to the back and front facets, respectively. In Fig. 5.12 the $L-I$ curve for the laser with coatings is depicted. As seen in the graph, the threshold current decreased to 19 mA and output power at 100 mA increased up to almost 15 mW. The slope efficiency is around 0.17 mW/mA. It is clear that reflection coatings improve the performance. However, for comparison the $L-I$ curve of Fabry-Perot laser (dots), which was fabricated on the same chip is plotted in the same figure. The threshold current of FP laser is around 22 mA. The slope efficiency of the slotted laser is reduced to around half of the FP laser. This was due to the loss caused by the etched slots. By measuring the amplified spontaneous emission (ASE) of the FP laser we calculated the net modal gain spectrum by the Fourier series expansion (FSE) method [11] which is given in Chapter 4. From the calculations we found the internal loss to be 22 cm^{-1}. Also some fabrication issues mentioned in section 5.2.2 caused the reduction in slope efficiency.

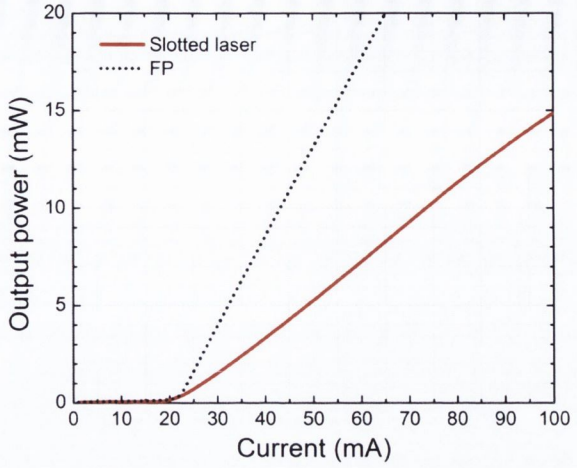

Fig. 5.12 Measured $L-I$ curves for HR and AR coated slotted laser (solid line) and FP laser fabricated on the same chip (dotted line).

The $L-I$ curve of laser diodes is usually linear, however, there can occur some nonlinearities or kinks due to the parasitic series resistance, current leakage or overheating of the material gain. To find this, derivatives of $L-I$ and $V-I$ curves can be used. Fig. 5.13 (left) shows $L-I$ curve and its derivative dL/dI curve as a function of injection current for a slotted laser with AR and HR coatings. From the figure we don't see any major kinks and dL/dI curve remains stable above threshold regime. However, there is a slight decrease at high currents but it is because of excessive heat generation. In Fig. 5.14 (right) the $V-I$ curve and IdV/dI curve as a function of injection current is shown. This derivative determines the series resistance of a laser diode. In other words, it shows the quality of a metal contact of a laser diode. In our case the resistance is around 9.5 Ohms. Also, from IdV/dI curve we can define a threshold current. In the Fig. 5.13 (right) we see a kink at injection current of 19 mA. This kink shows the threshold current of the slotted laser.

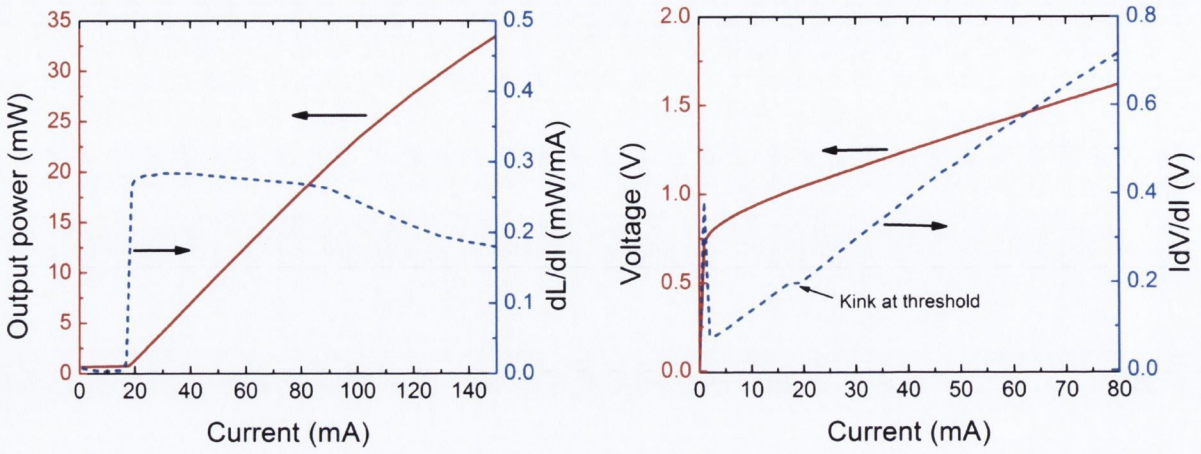

Fig. 5.13 (left) Measured $L-I$ curve and dL/dI curve vs. injection current, for HR and AR coated slotted laser. (right) Measured $V-I$ curve and IdV/dI curve vs. injection current for the same laser.

5.3.2. Spectral characteristics

To measure the output spectrum of the laser we used an Agilent 86140B optical spectrum analyzer with resolution of 0.06 nm and sensitivity of -80 dBm. Fig. 5.14 shows lasing wavelength for the slotted laser with HR and AR coatings. The peak is around 1550 nm at 38 mA which is twice of threshold current (I_{th}~19 mA). The side mode suppression ratio (SMSR) is around 51 dB at this current value.

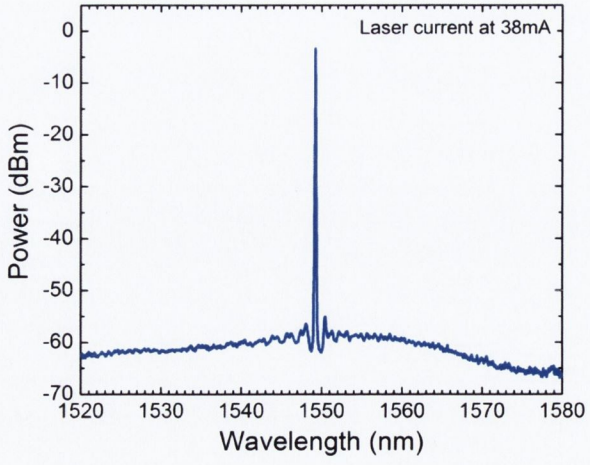

Fig. 5.14 Measured output spectrum of slotted laser with HR and AR coatings at 38 mA.

From the measured spectrum we can define what the effective cavity length of the laser. The effective cavity length can be expressed through equation:

$$\Delta\lambda = \frac{\lambda_0^2}{2n_g L_{eff}}, \tag{5.5}$$

where $\Delta\lambda$ is mode spacing, λ_0 is PL peak, n_g is a group refractive index of an active waveguide. Fig. 5.15 shows mode spacing of the laser which is around 1.2 nm. The laser peak is 1549.24 nm. By applying these numbers to the equation above, we found the effective cavity length, L_{eff} to be around 315 μm.

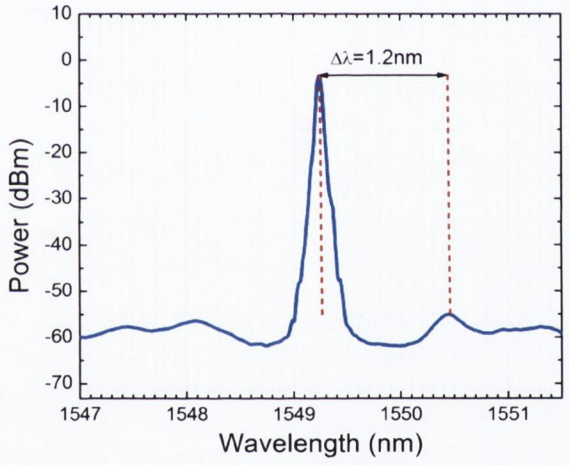

Fig. 5.15 Mode spacing of slotted laser at 38 mA.

One of the important laser characteristics is the tunability of the laser. There are two parameters which cause the center wavelength of the laser to shift. They are the drive current and temperature change. The former one is often used for wavelength tuning of single mode lasers. Changes in temperature affect the bandgap of the semiconductor laser hence the peak wavelength of the gain will be affected as well. To check the tunability of our laser we changed the temperature of the chip using the TEC. Fig 5.16 (left) shows the laser output spectrum over a temperature range from 10 to 50°C. The laser current was set at 130 mA to increase the SMSR. From the figure it is seen that the laser can work over a wide temperature range without mode hopping and stable single mode operation with SMSR more than 50 dB. The laser wavelength can be tuned over 4 nm in a 40°C temperature

variation as shown in Fig. 5.16 (right). Also in the figure we see linear behavior with tuning range of around 0.1 nm/^{o}C which is typical for telecom lasers.

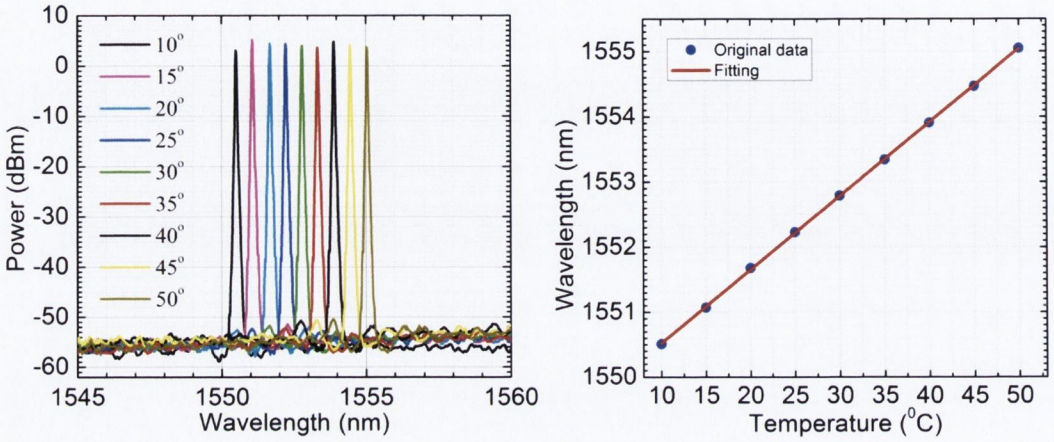

Fig. 5.16 (left) Measured output spectrum of slotted laser at 130 mA over a temperature range from 10 to 50°C. (right) Wavelength tuning versus temperature change of the laser.

5.3.3. Slot width characterization

The fabrication tolerances of the slot parameters are simulated in [12]. From the simulations it was found that slot depth has a large influence on reflection and hence on threshold current and output power of the laser. To overcome this problem a proper etching stop layer should be included during the fabrication to control the slot depth. The proper etching stop layer includes a combination of dry etching and wet etching processes. This is not present in the IQE standard material that we use. Another slot parameter which can be caused by fabrication inaccuracy is slot width. For the simulations different slot width were considered with variation of $\pm$0.1 μm. From the simulations a variation of slot width ($\pm$0.1 μm) doesn't affect to the threshold current as shown in Fig. 5.17.

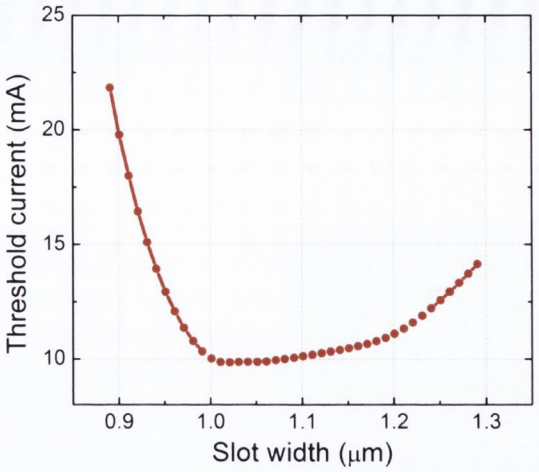

Fig. 5.17 Simulated threshold current versus slot width.

To check this, the lasers with different slot width were fabricated, e.g. 0.9, 1.0, 1.1, 1.2 and 1.3 μm. The lasers have the same effective cavity length, L_{eff} of around 350 μm. Other slot parameters such as slot depth, period and number are the same as well. As predicted from the simulations, the slot width doesn't affect the laser threshold current as shown in Fig. 5.18. The threshold current for all lasers remains around 32 mA. However, the slope efficiency changes a lot. This is because the reflection changes with the slot width as it was demonstrated from the simulations in Fig. 5.3 which affects the power. Therefore, it will lead to a big change in the slope efficiency even though, the threshold doesn't change much.

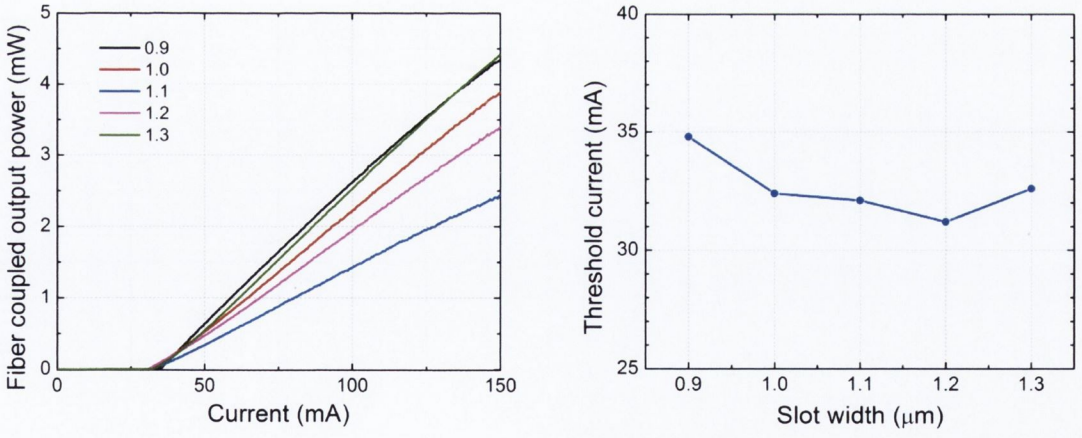

Fig. 5.18 (left) Measured L-I curves for lasers with different slot width from 0.9 to 1.3 μm. (right) Threshold current as a function of slot width.

From the experiments it was found that the slot width doesn't affect to the spectrum of the laser either. The lasers were driven at 100 mA at room temperature. The results are shown in Fig. 5.19. The figure shows laser peak and the SMSR as function of slot width. It is

clearly seen that the laser wavelength peak doesn't change at all and remains around 1546 nm. The SMSR also doesn't change and for all lasers the SMSR is around 50 dB at 100 mA. This means that lasers exhibit stable single mode operation.

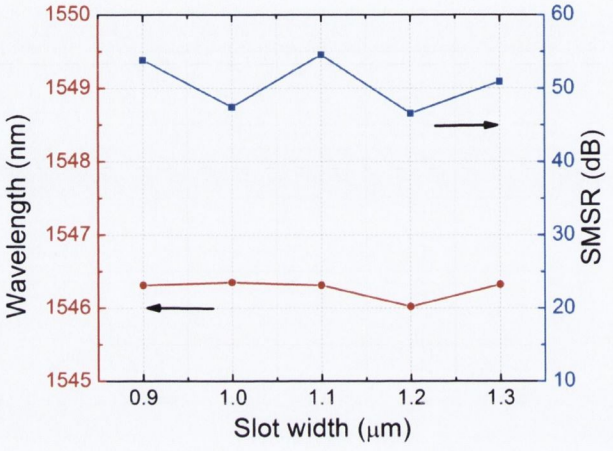

Fig. 5.19 Wavelength peak and SMSR as function of slot width.

The characterization presented above shows that these lasers can be fabricated by a standard photolithography process to pattern the slots. This will be advantageous in terms of time, ease of fabrication and cost.

5.3.4. Monolithically integration of slotted laser with SOA and EA modulator

The ability to integrate semiconductor lasers with other photonics components in one chip is a crucial advantage in terms of size, packaging and cost. In addition, integration of semiconductor lasers and other photonic components on the same chip reduces high fiber-to-fiber coupling losses which occur in discrete components. In the slotted lasers one facet is not cleaved and hence it is possible to integrate it with amplifiers and modulators. We demonstrated that by monolithically integrating the slotted laser with a semiconductor optical amplifier (SOA). It was done also to boost the output power due to the losses from the slots discussed above. In Fig. 5.20 the schematic structure of the laser integrated with the SOA is shown. The laser structure is the same as in section 5.2.1. The SOA is angled to 7^{o} from the normal of the facet to eliminate any back reflection. The length of the SOA section

is around 190 μm. An isolation slot is added to electrically isolate the SOA section from the laser section to reduce the threshold current while increasing output power. Finally, an AR coated film was applied to the front section.

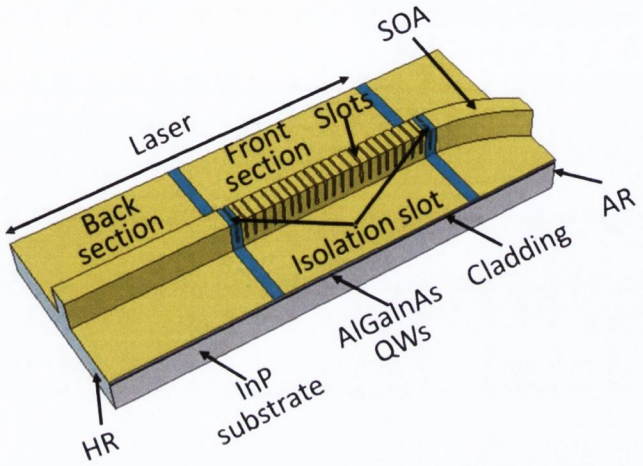

Fig. 5.20 The schematic structure of the laser integrated with an SOA on the same chip.

To measure the total output power from the laser we kept the laser current at a constant value of 130 mA and changed the SOA current as demonstrated in Fig. 5.21. The output power was more than 45 mW at an SOA current injection of 70 mA which means the total current injection into the system is 200 mA in this case.

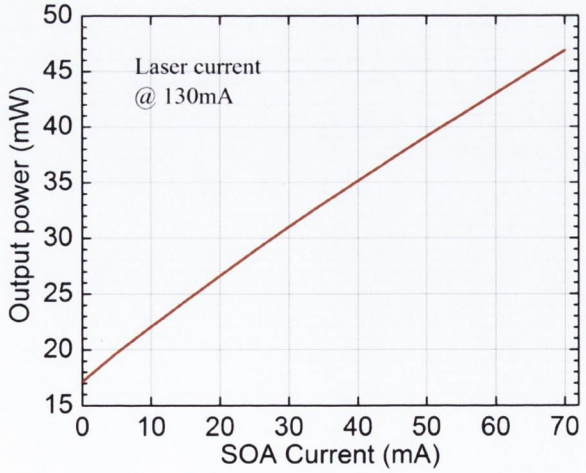

Fig. 5.21 The laser output power as a function of SOA current.

The SOA didn't influence the spectrum of the laser. As it was designed the SOA should only increase the output power and not affect to the lasing wavelength. This is achieved due to applied AR coating in the end of the SOA which suppresses the cavity resonances. Essentially, an SOA is a laser diode with a Fabry-Perot type cavity where amplification is achieved by electrically pumping the active region. However, to get only the amplification the FP resonances must be suppressed to remove the laser effect and usually it is done by applying AR coating to the end of the facet.

In Fig. 5.22, the laser spectra for the SOA unbiased and biased at 50 mA current is shown. It is seen that the SOA doesn't affect to the laser wavelength but only changes the amplitude of the spectrum. There is a small change in the wavelength (~0.15 nm) which is caused due to temperature rise when SOA is turned on. We also see no clear FP resonance ripples in the laser spectrum when SOA is biased which proves that the angled output with the AR coating is efficient to reduce the reflection from the facet.

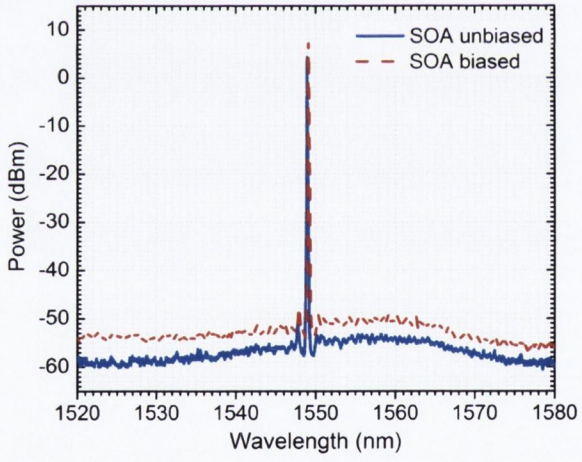

Fig. 5.22 Measured output spectrum of the slotted laser with SOA unbiased and biased at 50 mA. The laser current was set at 130 mA.

The temperature tuning of the laser with SOA turned on was also recorded as shown in Fig. 5.23. The laser current was set as previous at 130 mA, the SOA was set at 50 mA and the temperature of the chip was changed from to 10 to 50°C. Again the laser shows stable single mode operation without mode hops with a slight wavelength shift of 0.15 nm due to the temperature rise when SOA is biased.

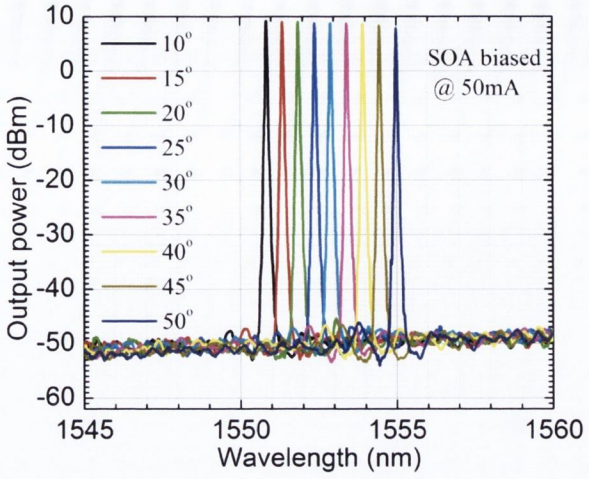

Fig. 5.23 Measured output spectrum of the slotted laser over a temperature range from 10 to 50°C with SOA biased at 50 mA.

The electro-absorption (EA) modulator is a semiconductor device to control the laser intensity by applying an electric voltage. The main advantages of EA modulator are low voltage operation, high bandwidth, less wavelength chirp and easy integration with CW lasers. A lot of work in different types of integration schemes such as Butt-joint etching [13], selective area growth (SAG) [14] and nonplanar epitaxy [15] have been published, however such methods need complicated growth process and fabrication. In terms of simple fabrication and low cost, the identical active layer (IAL) [16], [17] method can be used to monolithically integrate a CW laser with an EA modulator. Its principle is based on the quantum confined Stark effect (QCSE) which was given in Section 2.3.2. In QCSE the quantum well is placed between a reverse biased pn-junction, so that the applied electric field influences the refractive index [16]. In this method the laser and modulator will have the same quantum well active region.

The schematic structure of the slotted single mode laser integrated with an EA modulator is shown in Fig. 5.24. The epitaxial structure of the laser is the same as was mentioned above in section 5.2.1. The slotted laser and EA have the same quantum well layer which consists of AlGaInAs multiple quantum wells. The laser length is around 600 μm and EA length is around 200 μm. An angled (10°) deep etched slot was introduced between the laser and modulator for the electrical isolation. The typical isolation resistance was measured to be around 100 kΩ. The microscope image of the real device is shown in Fig. 5.25.

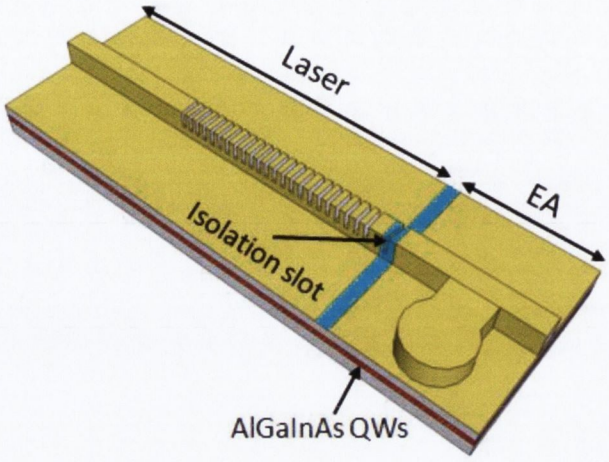

Fig. 5.24 The schematic image of slotted laser monolithically integrated with EA modulator.

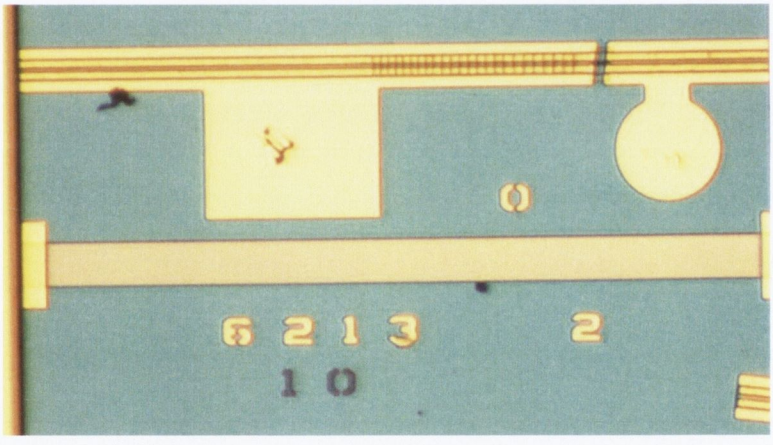

Fig. 5.25 Microscope image of slotted laser integrated with electro absorption (EA) modulator.

For integration with the EA modulator, the laser wavelength needs to be red shifted from the gain peak. To obtain this the slot parameters should be optimized. For a group of slots with uniform slot period of 9 μm, the calculated free spectral range is about 37 nm which means there are three reflection peaks in the wavelength range between 1500 and 1600 nm as shown in Fig. 5.26. We need to suppress the side peaks to shift the laser wavelength to the longer wavelength. To obtain this we introduced three different slot periods (8.5, 9.9, 11.4 μm) as shown in Fig. 5.26 (left), where nearly no overlap between the side peaks exists. Fig. 5.26 (right) shows the calculated reflection spectrum from such a group of slots, where the central reflection peak dominates and side modes are suppressed.

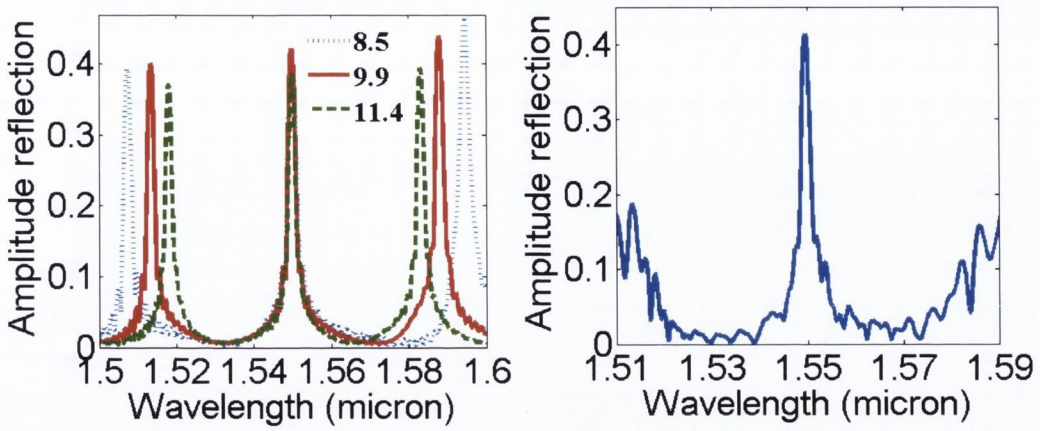

Fig. 5.26 (left) Calculated reflection spectrum from group of 24 slots with the slot periods of 8.5, 9.9 and 11.4 μm. (right) with three above slot periods.

Fig. 5.27 shows the calculated reflection spectrum with the gain under a current density of 2300 A/cm^2. It is seen that at longer wavelength, the gain is lower which results in low reflection hence in a higher threshold. For the trade-off between low threshold and high extinction ratio of the EA modulator, the laser wavelength is designed to be around 1570 nm.

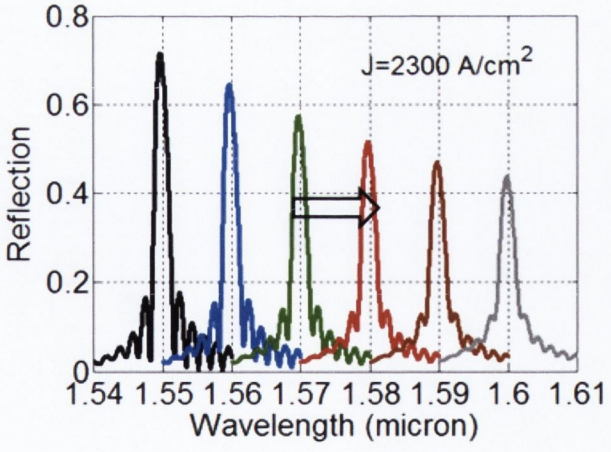

Fig. 5.27 Calculated red shift reflection spectrum.

First, the output spectrum from the EA modulator facet was measured which is shown in Fig. 5.28. The laser current was set at 100 mA and the modulation voltage was set to 0 V. From the figure it is seen that stable single mode emission with a lasing wavelength at 1569

nm which is around 20 nm of a red shift from the gain peak. The SMSR is over 50 dB at 100 mA of injection current.

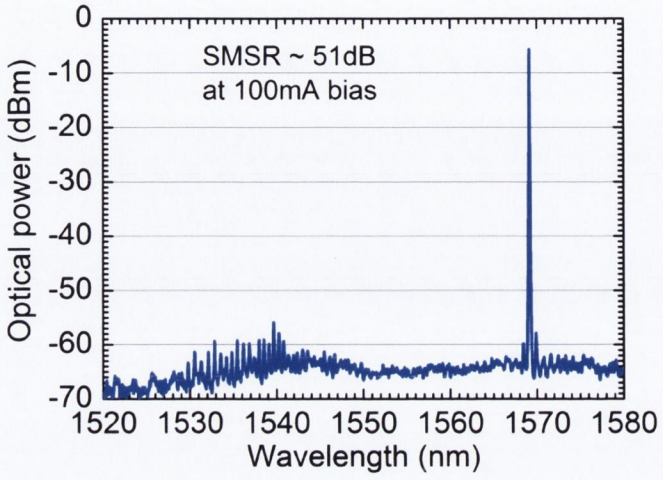

Fig. 5.28 Measured output spectrum from the EA facet at 0 V.

Fig. 5.29 shows the spectrum from EA facet for various EA modulator reverse bias voltage. There is no peak change for different reverse bias voltages which is good. The SMSR remains over 50 dB at 200 mA of laser injection current.

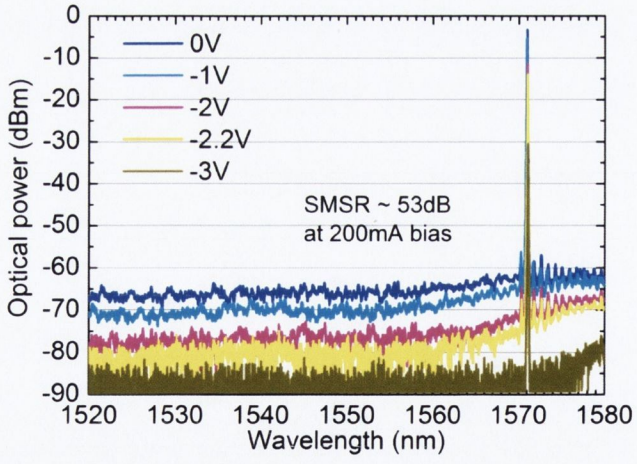

Fig. 5.29 Measured output spectrum for different EA reverse bias voltage. Laser diode set at 200 mA.

The normalized output power versus reverse bias of EA modulator is shown in Fig. 5.30. An extinction ratio of around 10 dB was obtained when the modulator bias was -2.2 V. A 20 dB extinction would be required from a commercial device, so there is still more work to be done on the integrated laser-EA modulator.

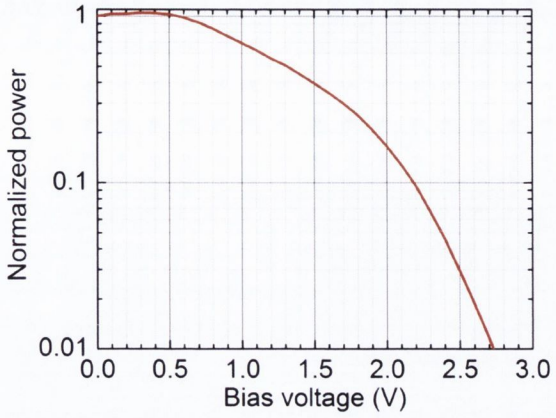

Fig. 5.30 The normalized output power versus the reverse bias of EA modulator.

5.4. Linewidth measurements

5.4.1. Free space setup

There are different methods to measure laser linewidth such as homodyne, heterodyne and delayed self-heterodyne methods. For the linewidth characterization of the slotted lasers the delayed self-heterodyne (DS-H) method was used [18]. The advantage of this technique is there is no need to use a reference laser (local oscillator) in comparison with heterodyne methods. Instead of this a large optical delay is needed. The experimental setup of the DS-H method is depicted in Fig. 5.31.

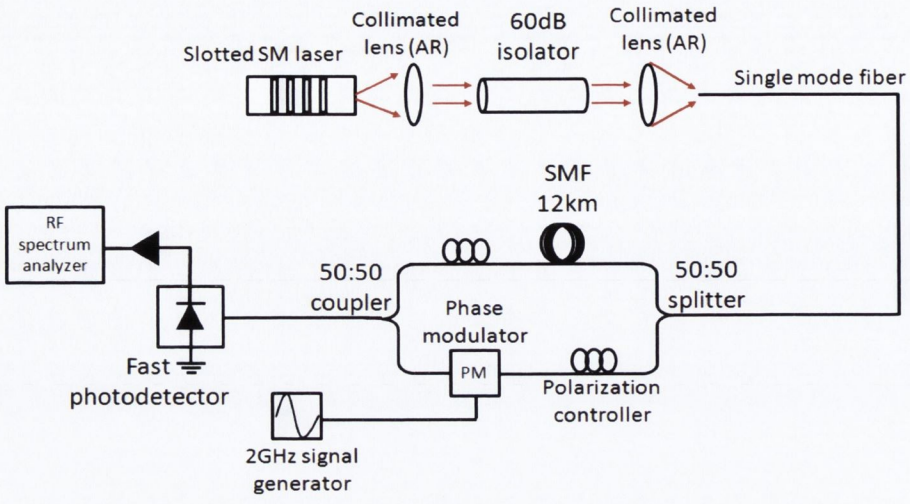

Fig. 5.31 Delayed self-heterodyne technique for linewidth characterization.

The concept of this technique is that light from the laser is split into two paths. One part goes through a 12 km long optical fiber which corresponds to 60 μs optical delay. Another part passes through a phase modulator to shift the signal to 2 GHz to see the whole spectrum. Polarization controllers maintain the beam polarization. Then the two combined beams are sent to a fast photodetector and the linewidth spectrum is recorded by an electrical spectrum analyzer (ESA). The optical delay serves as a local oscillator in heterodyne detection, making the two combined beams appear as they were from two separate sources. The fast photodetector detects the mixed optical signal and converts it to an electrical signal which is recorded by the ESA. If the optical delay time is larger than the coherence time of the laser, then the spectrum detected by the ESA will be the spectrum of the laser, but at lower frequencies. Therefore, we use a phase modulator to shift the signal to higher frequencies to increase the measurement accuracy. Because we are dealing with unpackaged devices it is very important to have sufficiently high isolation to avoid any back reflections to the laser cavity. For this we added to the DS-H setup two antireflection coated collimation lenses and a 60 dB optical isolator to minimize any back reflection.

5.4.2. Linewidth characterization

For the linewidth characterization a laser with cavity length of 750 μm was used. The effective cavity length of this laser is around 450 μm. From Fig. 5.31 the threshold current is around 31 mA and the side mode suppression ratio is around 50 dB at 64 mA which is twice the threshold current.

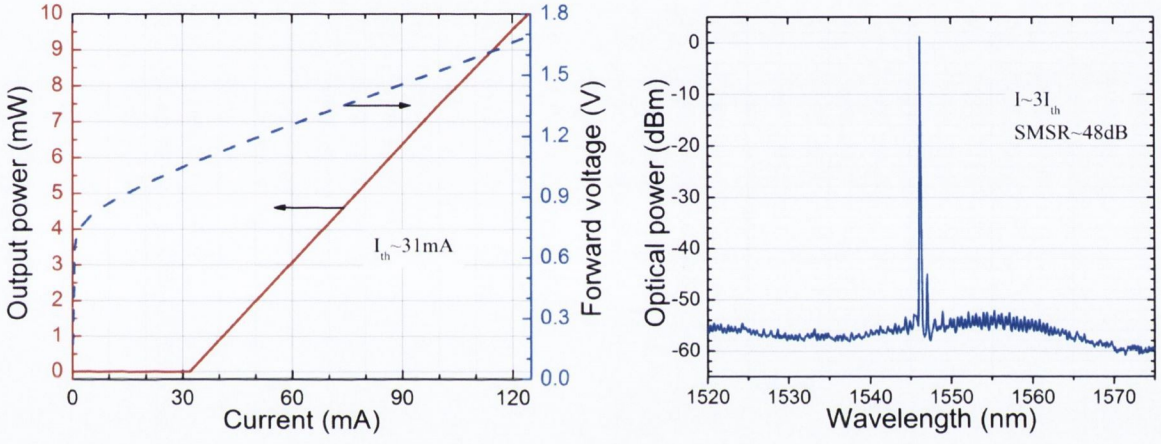

Fig. 5.32 (left) $L-I-V$ curve for slotted with effective cavity length of 450 μm. (right) Output spectrum of slotted laser at 64 mA.

Fig. 5.33 shows the electrical spectrum of slotted laser at 130 mA recorded by electrical spectrum analyzer (ESA). The resolution bandwidth of the ESA was set at 30 kHz. Blue dots represent original data and red line is Voigt fitting which is a convolution of Lorentz and Gaussian profiles [20]. The spectrum is well fitted with a Voigt function. The Lorentzian or intrinsic linewidth of the laser is found to be around 840 kHz at 130 mA.

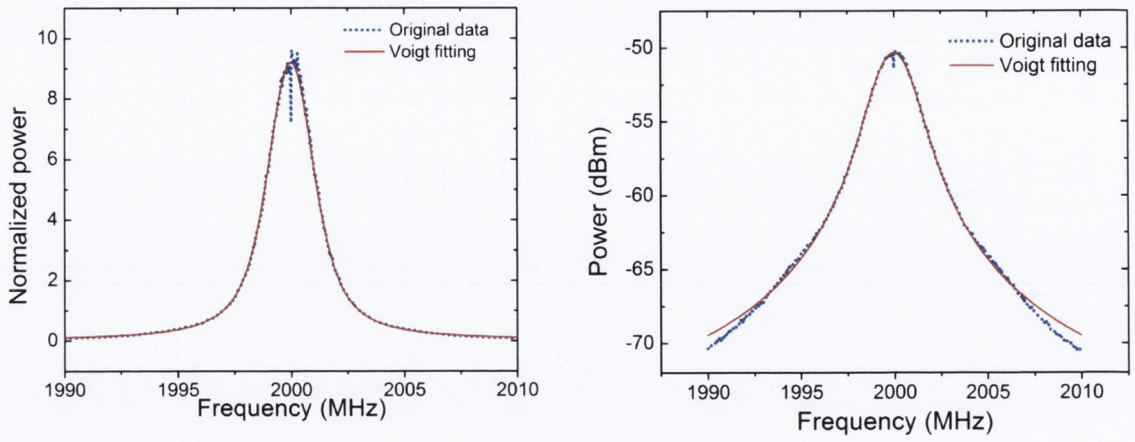

Fig. 5.33 Measured spectrum in (left) linear and (right) log scales of slotted single mode laser fitted by Voigt fitting.

The basic linewidth characterization is the linewidth dependence on output power. The well known Schawlow-Townes formula modified by Henry [19], expresses the linewidth as being inversely proportional to output power. In Fig. 5.34 this behavior was verified; the linewidth of slotted laser was measured between 60 to 180 mA using an ultra low noise current source at room temperature. It is clearly seen that a dramatic decrease of linewidth occurs by increasing the number of carriers injected into the system. The blue dots represent the intrinsic linewidth of the laser and red dots correspond to the full width at half maximum (FWHM). The lowest intrinsic linewidth of the laser is around 720 kHz at 170 mA. As found in [20], a Gaussian profile comes from the technical noise and as seen in the figure at high currents the Gaussian contribution is greater than the intrinsic Lorentzian linewidth, hence the total linewidth or FWHM gets larger again at high currents.

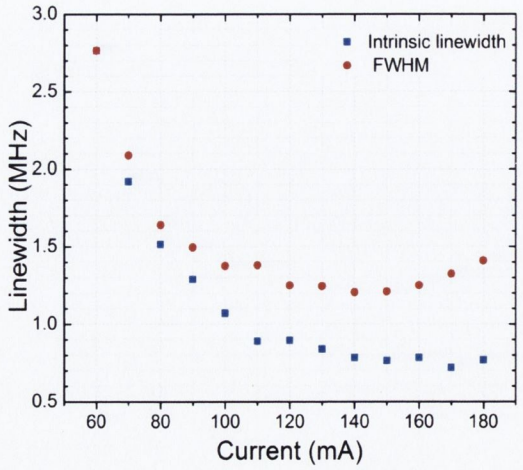

Fig. 5.34 Lorentzian linewidth and FWHM as a function of injection current.

Fig. 5.35 shows conventional linewidth dependence on inverse output power which was obtained by converting input current to output power using Fig. 5.32 (left) shown above.

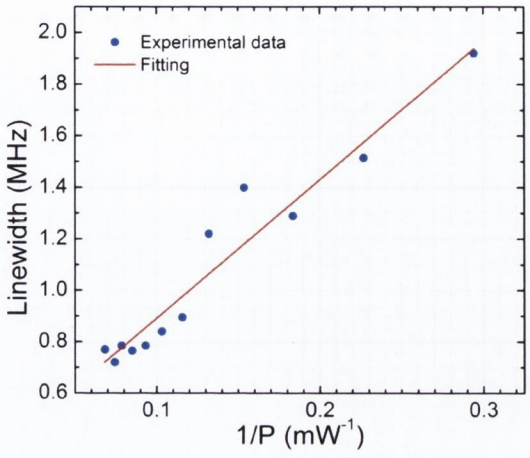

Fig. 5.35 Linewidth dependence on inverse output power.

The linewidth dependence on temperature was also measured. The laser was set at 130 mA and the laser chip temperature was changed using TEC. The TEC temperature was changed from 10 to 70°C. Fig. 5.36 shows the Lorentzian linewidth as a function of temperature. Results show that temperature has a negligible influence on linewidth within temperature range from 10 to 60°C and remains around 1 MHz. However, at higher temperatures, the laser power drops and affects the laser linewidth. So for 70°C the laser linewidth broadens up to 2 MHz. Moreover, because the measurements were done with unpackaged devices at high temperature this leads to poor heat dissipation which in turn gives rise to increased spontaneous emission and to broadening of the linewidth.

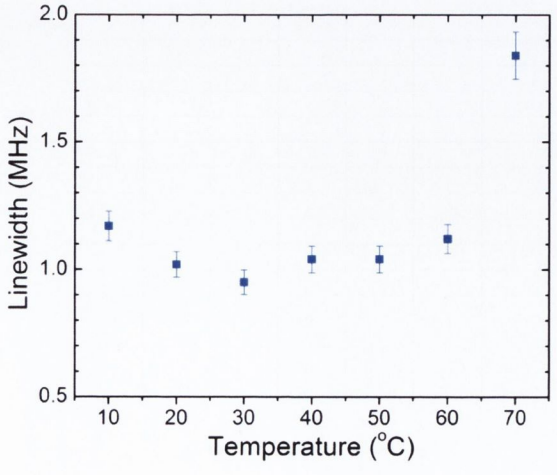

Fig. 5.36 Linewidth dependence on laser temperature from 10 to 70°C.

The next step of the linewidth characterization was to check how slot parameters will affect to laser linewidth. For this, lasers with different slot width were chosen, i.e 0.9, 1.0, 1.1, 1.2 and 1.3 μm. For these lasers the effective cavity length, L_{eff} were about 350 μm. These variations in slots were done due to the likely fabrication inaccuracy if standard photolithography were used. From the simulations in [12] and from the experimental results shown in section 5.3.2, a variation of slot width (±0.1 μm) doesn't influence the threshold current as shown in Fig. 5.37.

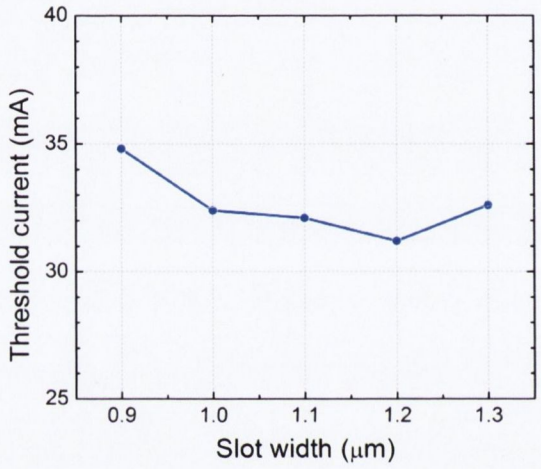

Fig. 5.37 Measured threshold current versus slot width.

From the experiments we see that the slot width does not affect the linewidth strongly as shown in Fig. 5.38 which is the linewidth dependence on injection current for lasers with different slot width. From the figure the overall trend is the same as the current increased, the linewidth for different lasers varies between 1.5 to 3 MHz at highest current. Also, we can clearly see the connection between the variations in linewidth and the variations in slope efficiencies observed earlier in Fig. 5.18 (left). It was mentioned that the slot width variation will change the reflection (see Fig. 5.3), therefore, the power will be affected. However, we need to have a large set of lasers with different slot widths and depth to obtain a clear picture of the effects of slot parameters on the linewidth.

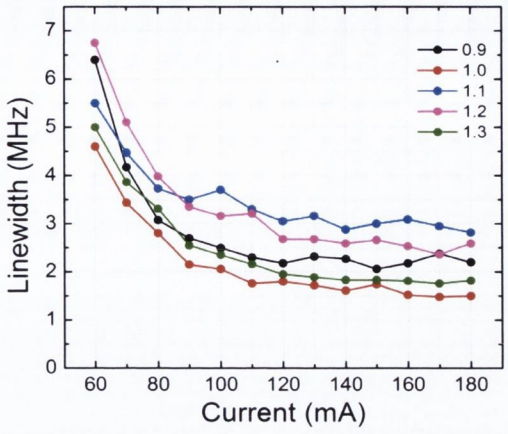

Fig. 5.38 Linewidth as a function of injection current for lasers with different slot width from 0.9 to 1.3 μm.

It is well known that the spectral linewidth is inversely proportional to laser cavity length. When the cavity length increases, the threshold carrier density decreases as shown in equation (2.11). This will reduce the spontaneous emission rate R_{sp} and the linewidth enhancement factor α. Hence, the linewidth will decrease as described in equation (2.24). Therefore, by making the laser longer it is possible to achieve narrower linewidth [21], [22], [23]. To check this initially we took three different lasers with different effective cavity lengths, i.e 250, 350 and 450 μm. The slot width for all of these lasers is 1.0 μm. The lasers were set at a room temperature of 20°C. The linewidth dependence on injection current for different cavity length is shown in Fig. 5.39. As was predicted the longer the cavity length the narrower is the linewidth. The lowest linewidth was 720 kHz at 170 mA for the laser with the effective cavity length of 450 μm.

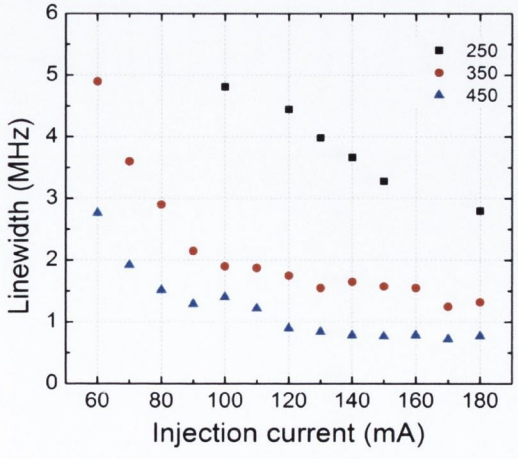

Fig. 5.39 The linewidth versus injection current for different effective cavity length lasers.

Considering the results above we can predict what the effective cavity length should be to achieve a laser linewidth below 0.5 MHz which is the main requirement in coherent communications. Fig. 5.40 shows the spectral linewidth at 150 mA of injection current for lasers with different cavity length. The extrapolation in Fig. 5.40 indicates that a laser with effective cavity length of only 550 μm is required to reach the point below 0.5 MHz.

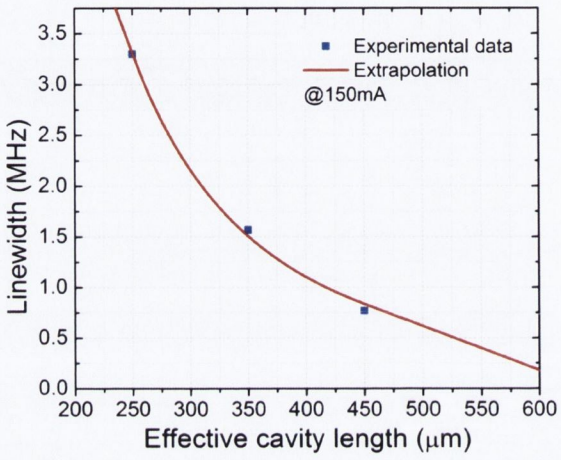

Fig. 5.40 The Lorentzian linewidth dependence on effective cavity length of the slotted laser.

5.5. Conclusion

In this chapter the design and performance of slotted single mode lasers are presented. The presented devices use high order gratings or slots etched on top of the ridge waveguide structure to achieve optical feedback. Through etching the slots as deep as possible but not through the active region it is possible to remove the fundamental FP cavity and make lasers totally dependent on slots. In this way lasers are based on single epitaxial growth steps or in other words re-growth free fabrication steps and can be integrated with other photonic components.

The fabricated lasers exhibit a threshold current of 32 mA with slope efficiency of 0.11 mW/mA. To improve the laser performance in terms of the threshold current and output power, an anti-reflection and high-reflection coatings were applied to the front and back facets, respectively. The threshold current decreased to 19 mA and slope efficiency increased to 0.17 mW/mA. The SMSR more than 50 dB was achieved when the laser is

biased at twice the threshold current and it remains stable during the temperature tuning over the range from 10 to 50°C. The fabrication tolerances of the slot width are also investigated. It was found that the slot width does not affect much at SMSR and the threshold current.

Because the lasers totally dependent on slots and don't need to cleave the both facets, these lasers can be integrated with other photonic components in one chip. We have demonstrated that these lasers can be monolithically integrated with an SOA and an EA modulator. The integrated devices have output power more than 45 mW and DC extinction ratio around 10 dB.

The spectral linewidth has been characterized in detail and it was found that for short cavity length lasers it varies between 1 and 2 MHz. However, for long cavity lasers a linewidth of below 1 MHz has been achieved. It is also predicted that by increasing the effective cavity length, we can reach the industry standard of 500 kHz linewidth for coherent communications.

Overall, the key advantage of these lasers is the simple fabrication technology with straightforward method. The laser structure needs only a single wafer growth during the entire fabrication process and can be fabricated by standard photolithography which is beneficial in terms of cost and time. In addition, the ability to integrate these lasers with SOA, EA modulators and passive optical circuits like beam splitters/combiners make such a laser platform to have a strong potential to become a light source in WDM and coherent communication systems.

Reference

[1] Y. Inaba, H. Nakayama, M. Kito, M. Ishino and K. Itoh, "High-power 1.55-m mass-transport-grating DFB lasers for externally modulated systems," *IEEE Journal of Selected Topics in Quantum Electronics,* vol. 7, no. 2, 2001.

[2] M. Faugeron, M. Tran, F. Lelarge, M. Chtioui, Y. Robert, E. Vinet, A. Enard, J. Jacquet and F. V. Dijk, "High power, low RIN 1.55μm directly modulated DFB lasers for analog signal transmission," *IEEE Photonics Technology Letters,* vol. 24, no. 2, pp. 116-118, 2012.

[3] J. Telkka¨la, J. Viheria¨la, A. Aho, P. Melanen, J. Karinen, M. Dumitrescu and M. Guina, "Narrow linewidth laterally-coupled 1.55 mm DFB lasers fabricated using nanoimprint lithography,"

Electronics Letters, vol. 47, no. 6, pp. 400-401, 2011.

[4] L. Hou, M. Haji, J. Akbar and J. H. Marsh, "Narrow linewidth laterally coupled 1.55 μm AlGaInAs/InP distributed feedback lasers integrated with a curved tapered semiconductor optical amplifier," *Optics Letters,* vol. 37, no. 21, pp. 4525-4527, 2012.

[5] R. M. Lammert, A. M. Jones, C. T. Youtsey, J. S. Hughes, S. D. Roh, I. Adesida and J. J. Coleman, "InGaAsP–InP ridge-waveguide DBR lasers with first-order surface gratings fabricated using CAIBE," *IEEE Photonics Technology Letters,* vol. 9, no. 11, pp. 1445-1447, 1997.

[6] B. Corbett and D. McDonald, "Single longitudinal mode ridge waveguide 1.3 μm Fabry-Perot laser by modal perturbation," *Electronics Letters,* vol. 31, no. 25, pp. 2181-2182, 1995.

[7] C. Herbet, D. Jones, A. Kaszubowska-Anandarajah, B. Kelly, M. Rensing, J. O'Carroll, R. Phelan, P. Anandarajah, P. Perry, L. P. Barry and J. O'Gorman, "Discrete mode lasers for communication applications," *IET Optoelectronics,* vol. 3, no. 1, pp. 1-17, 2009.

[8] Y. Wang, Y. Yang, S. Zhang, L. Wang and J. J. He, "Narrow linewidth single-mode slotted Fabry–Pérot laser using deep etched trenches," *IEEE Photonics Technology Letters,* vol. 24, no. 14, pp. 1233-1235, 2012.

[9] B. Kelly, R. Phelan, D. Jones, C. Herbert, J. O'Carroll, M. Rensing and J. O'Gorman, "Discrete mode laser diodes with very narrow linewidth emission," *Electronics Letters,* vol. 43, no. 23, pp. 1282-1284, 2007.

[10] Q. Lu, W. H. Guo, R. Phelan, D. Byrne, J. F. Donegan, P. Lambkin and B. Corbett, "Analysis of slot characteristics in slotted single-mode semiconductor lasers using the 2-D scattering matrix method," *IEEE Photonics Technology Letters,* vol. 18, no. 24, pp. 2605-2607, 2006.

[11] W. H. Guo, D. Byrne, Q. Lu, B. Corbett and J. F. Donegan, "Fabry-Perot laser characterization based on the amplified spontaneous emission spectrum and the Fourier series expansion method," *IEEE Journal of Selected Topics in Quantum Electronics,* vol. 17, no. 5, pp. 1356-1363, 2011.

[12] Q. Lu, W. H. Guo, D. Byrne and J. F. Donegan, "Design of slotted single mode lasers suitable for photonic integration," *IEEE Photonics Technology Letters,* vol. 22, no. 11, pp. 787-789, 2010.

[13] U. Koren, B. I. Miller, M. G. Young, M. Chien, G. Raybon, T. Brenner, R. Ben-Michael, K. Dreyer and R. J. Capik, "Polarization insensitive semiconductor optical amplifier with integrated electroabsorption modulators," *Electronics Letters,* vol. 32, no. 2, pp. 111-112, 2002.

[14] B. Mason, A. Ougazzaden, C. W. Lentz, K. G. Glogovsky and C. L. e. a. Reynolds, "40-Gb/s tandem electroabsorption modulator," *IEEE Photonics Technology Letters,* vol. 14, no. 1, pp. 27-29, 2002.

[15] F. Koyama, K. Y. Liou, A. G. Dentai, G. Raybon and C. A. Burrus, "GaInAs/GaInAsP strained-

quantum-well monolithic electroabsorption modulator amplifier by lateral bandgap control with nonplanar substrates," *Electronics Letters,* vol. 29, no. 24, pp. 2104-2106, 2002.

[16] A. Ramdane, F. Devaux, N. Souli, D. Delprat and A. Ougazzaden, "Monolithic integration of multiple quantum- well lasers and modulators for high-speed transmission," *IEEE Journal of Selected Topics in Quantum Electronics,* vol. 2, no. 2, pp. 326-335, 1996.

[17] B. Xiong, J. Wang, L. Zhang, J. Tian, C. Sun and Y. Luo, "High-speed (>40 GHz) integrated electroabsorption modulator based on identical epitaxial layer approach," *IEEE Photonics Technology Letters,* vol. 17, no. 2, pp. 327-329, 2005.

[18] T. Okoshi, K. Kikuchi and A. Nakayama, "Novel method for high resolution measurement of laser output spectrum," *Electronics Letters,* vol. 16, no. 16, pp. 630-631, 1980.

[19] C. H. Henry, "Theory of the linewidth of semiconductor lasers," *IEEE Journal of Quantum Electronics,* vol. 18, no. 2, pp. 259-264, 1982.

[20] S. Spießberger, M. Schiemangk, A. Wicht, H. Wenzel, O. Brox and G. Erbert, "Narrow linewidth DFB lasers emitting near a wavelength of 1064nm," *Journal of Lightwave Technology,* vol. 28, no. 17, pp. 2611-2616, 2010.

[21] S. Ogita, Y. Kotaki, M. Matsuda, Y. Kuwahara and H. Ishikawa, "Long-cavity multiple-phase-shift distributed feedback laser diode for linewidth narrowing," *Journal of Lightwave Technology,* vol. 8, no. 10, pp. 1596-1604, 1990.

[22] M. Okai, T. Tsuchiya, K. Uomi, N. Chinone and T. Harada, "Corrugation-pitch-modulated MQW-DFB laser with narrow spectral linewidth (170 kHz)," *IEEE Photonics Technology Letters,* vol. 2, no. 8, pp. 529-530, 1990.

[23] S. Ogita, Y. Kotaki, K. Kihara, M. Matsuda, H. Ishikawa and H. Imai, "Dependence of spectral linewidth on cavity length and coupling coefficient in DFB laser," *Electronics Letters,* vol. 24, no. 10, pp. 613-614, 1988.

Chapter 6 – Wavelength tunable laser array based on slotted single-mode lasers

6.1. Introduction to laser array

Widely wavelength tunable lasers are the major components in the wavelength-division multiplexing (WDM) systems and the main light source in optical add-drop multiplexing (OADM) nodes. So far, different types of wavelength tunable light sources, including sampled grating DBR (SGDBR) lasers [1], grating-coupled sampled reflector (GCSR) laser [2], external cavity lasers (ECL) [3] [4], tunable vertical-cavity surface-emitting (VCSEL) lasers [5] and distributed feedback laser (DFB) laser arrays have been developed [6] [7] [8]. The most successful lasers in terms of tuning range and narrow linewidth from this list are external cavity lasers, DBR lasers and DFB laser arrays. All of these laser structures provide wavelength tuning of more than 35 nm and low linewidth which is required in WDM systems.

The ECL can achieve a wide tuning range using a widely tunable filter in a free space part of the laser cavity. Generally, the cavity length of an ECL is long and might be several millimeters which in turn makes the laser linewidth very narrow [4]. However, the ECLs need hybrid integration and consist of many optical parts which make the laser complex in fabrication and in operation.

Monolithic widely tunable DBR lasers also have wide tuning ranges which can be achieved by changing the refractive index and/or temperature. Generally, the refractive index is changed by a carrier plasma effect induced by current injection. The most well known example of such lasers is a sampled-grating DBR (SG-DBR) laser. The tuning in these lasers is achieved by the Vernier effect which was discussed in Section 2.3.2. The structure consists of two mirrors which are sampled gratings with comb-like reflection spectra. By tuning the current in both mirrors, a set of overlapped reflection peaks will line up and a wide tuning range can be achieved. The tuning time in SG-DBR lasers is only a few nanoseconds [9]. However, such lasers suffer from complicated tuning mechanisms which require the control of three or more current injection. In addition, most of DBR lasers have

the linewidth in order of MHz which is too broad for coherent communications. However, new methods to reduce the linewidth below 500 kHz have been developed [10] [11].

Another way to obtain a widely tunable laser is to make a DFB laser array. Single mode DFB lasers are well known of their excellent performance, mode stability and reliability in terms of free mode hopping during temperature tuning. Although, the tuning time is much slower than in DBR lasers, the mode stability and the narrow linewidth make these lasers very attractive in commercial optical networks. Also, the tuning mechanism is simpler than in ECL and SG-DBR lasers because it needs only a temperature change to tune the wavelength. Many DFB laser arrays have been researched (See Table 1.3). The researchers from NTT company developed a 12-channel DFB laser array coupled with MMI coupler and integrated with an SOA. A wavelength tuning range of 40 nm and output power more than 40 mW was reported in [8], [12]. The linewidth of these lasers has been improved and recently they have demonstrated tunable DFB laser array with ultra-narrow spectral linewidth below 160 kHz for all channels [13]. Also they have demonstrated tunable DFB laser array integrated with Mach-Zehnder (MZM) and EA modulators for high speed applications [14], [15]. However, DFB lasers still require the re-growth of additional material on top of the gratings and need e-beam lithography to define the low order gratings. The disadvantages of complex fabrication are discussed in previous chapters and it was mentioned that it leads to time consuming, low yield and high cost process.

In a previous chapter we discussed how single mode operation is achieved by etching high order surface gratings on top of the ridge, which solves the issue with the re-growth process. By carefully optimizing the slot parameters we achieved stable single mode operation with high side-mode suppression ratio (SMSR). Lasers with a longer cavity length showed a linewidth around 500 kHz which makes these lasers suitable in coherent communications. By taking into account these results, we formed tunable laser array based on slotted single mode lasers. The advantage of such laser platforms is the re-growth free process, potential to use standard photolithography instead of e-beam and high yield. In this chapter, the design and characterization of two different tunable laser arrays will be discussed. First, a 10- channel laser array with periodic slot spacing and second a 12-channel laser array with non-periodic slot spacing will be presented. Also, the thermal impedance of such structures will be discussed at the end of the chapter.

6.2. 10 channel laser array

The schematic structure of the slotted single mode laser array is shown in Fig. 6.1. There are 10 single mode lasers in the array. Each laser of the array has a standard 2 μm-wide surface ridge waveguide structure. The laser epitaxial structure is the same as in section 5.2.2 which is based on standard 1550 nm laser diode design. The active region consists of five AlGaInAs quantum wells. Above it are a 1.6 μm thick p-doped InP layer, a 50 nm-thick p-doped InGaAsP layer and a 200 nm-thick InGaAs contact layer. One side of each laser has multiple unifromly distributed slots which act as an active DBR reflector of the laser and provide sufficient reflection for lasing. The other side reflection is provided by the cleaved facet. Because of this, there is a single mode issue caused by the uncertainty of the cleaving position. To remove this problem, each laser is divided into two sections and electrically isolated by the last slot as shown in Fig. 6.1. By changing the current of the back section it is possible to change the position of the longitudinal mode and move it to the reflection peak, and this will lead to single mode operation with high SMSR. This property will be demonstrated in the experimental results.

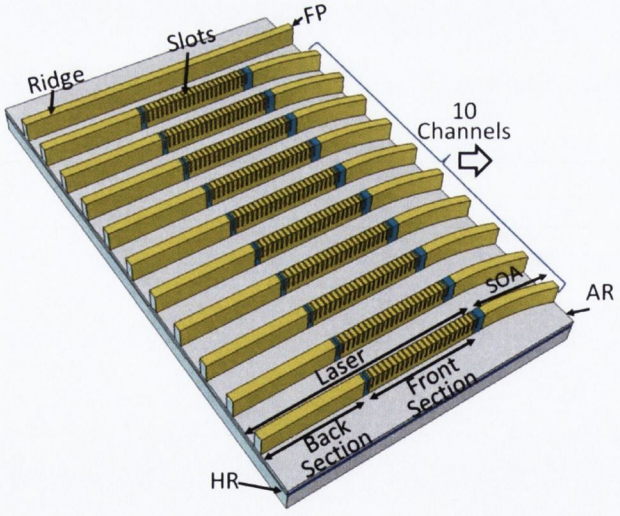

Fig. 6.1 3D schematic structure of tunable slotted single mode laser array. Each laser in the array consists of laser section integrated with SOA. The front and back facets are coated with AR and HR coatings, respectively. The last device is a FP laser on the same sub-mount for comparison.

Each laser in the array is monolithically integrated with an SOA to increase the output power. The SOA is angled to 7° with respect to the waveguide to reduce the reflection from the front facet. To further improve the laser performance in terms of increasing the output power and reducing the threshold current, antireflection (AR) and highreflection (HR) coatings were applied to the front and back facets, respectively.

For each laser in the array, the slot parameters such as slot width, depth and number are optimized. For optimization, the 2D scattering matrix method was used which was discussed in Chapter 3. The slot width is set to be around 1.1 μm, the slot depth is the same as for single mode lasers at 1.35 μm. Such a slot depth can provide around 1% amplitude reflection and 97% amplitude transmission for a single slot. Therefore, reflection from a single slot is weak and a group of slots is needed to provide sufficient reflection. The number of slots is optimized to be 24 which will maximize the reflection and minimize the bandwidth of reflection peaks and keep the cavity length relatively short to minimize the threshold. Such a group of slots will provide a narrow bandwidth of reflection spectrum to achieve good single mode emission. The laser array is designed to cover the full C-band which is between 1530 and 1565 nm as shown schematically in Fig. 6.2.

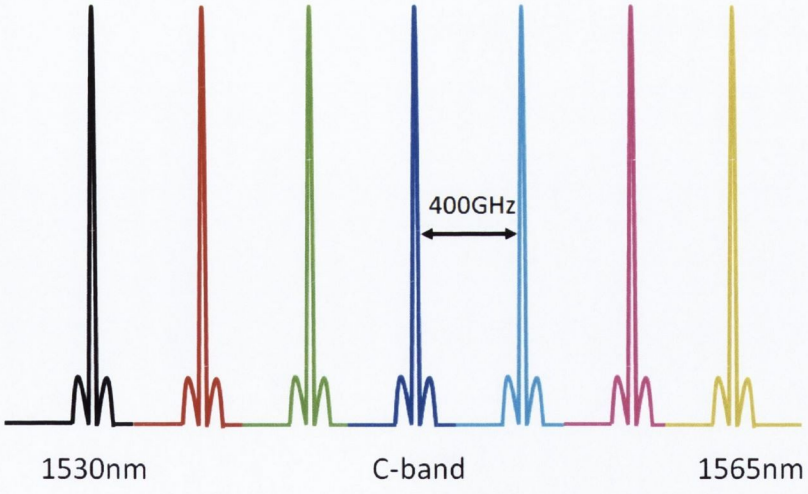

Fig. 6.2 Schematic spectra of C-band with channel spacing of 400 GHz.

We designed the laser array to have a frequency spacing of 400 GHz (3.2 nm) which is specified by ITU-T standards (ITU-T: International Telecommunication Union, Telecommunication Standardization Sector) [16]. This was achieved by changing the slot period according to:

$$d_p = \frac{m\lambda_B}{2n_{eff}} \tag{6.1}$$

where d_p is the slot period, λ_B is the Bragg wavelength, n_{eff} is the average effective refractive index in waveguide structure and m is grating order which is 37. Considering a 37th order grating, the slot periods of the individual lasers in the laser array are designed as 8.897, 8.917, 8.936, 8.954, 8.973, 8.992, 9.011, 9.030, 9.049 and 9.067 μm which correspond to lasing wavelengths as 1539, 1542.2, 1545.4, 1548.6, 1551.8, 1555, 1558.2, 1561.4, 1564.6 and 1567.8 nm with a channel spacing of 3.2 nm which is equivalent to 400 GHz.

For the fabrication process, the same method was used as was discussed in section 5.2.2. Two steps of ICP based dry etching process with Cl_2/N_2 gas combinations to form the ridge and the slots. E-beam lithography was used to pattern the slots. The total length of each laser in the array is around 400 μm plus a 190 μm long curved front SOA section. The back section is about 185 μm long and the front slotted section is about 205 μm long. After fabrication the ridge was passivated and metal contacted (the electrode metal covered the slots area except for the isolation slots), the laser array bars were coated with HR and AR films. Finally, the laser arrays were cleaved into individual bars and mounted on AlN carriers for testing. Fig. 6.3 shows a microscope image of 10-channel laser array based on slots. It is a top side image. Fig. 6.4 shows one laser from the array with a periodic slot spacing.

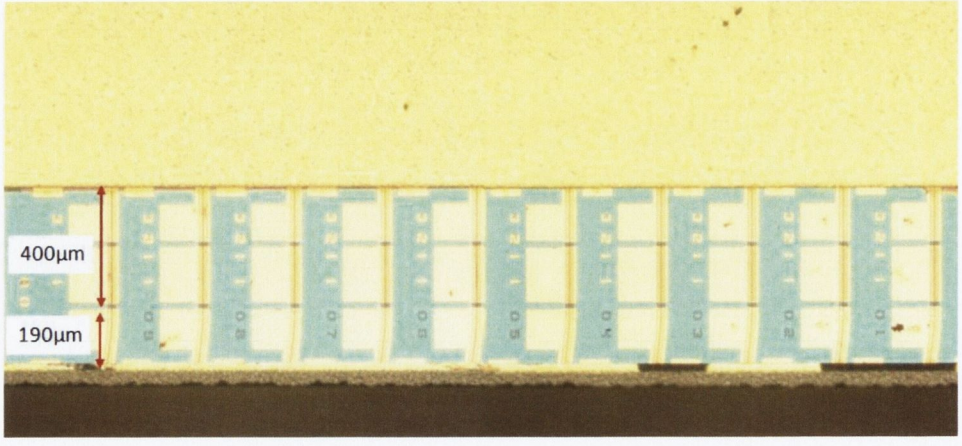

Fig. 6.3 Top side microscope image of 10-channel laser array based on slots. The numbers from 1 to 10 indicate the laser number. Each laser in the array has a cavity length of 400 μm and curved SOA section of 190 μm.

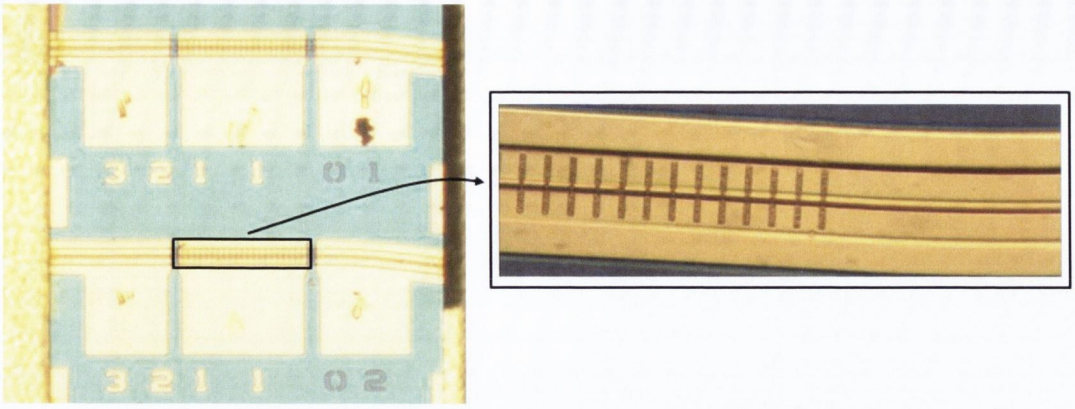

Fig. 6.4 Top side microscope image of two slotted lasers (left) and zoomed image of distributed slots with periodic slot spacing.

6.2.1. Basic characterization

The mounted devices were measured under CW condition. The temperature of the chip was controlled by a thermo-electrical cooler (TEC) and was set at 20°C. First, a typical light-current ($L-I$) characterization was measured to define the threshold current and output power. For this we electrically connected two sections of the laser, i.e. the front and back sections to give the same injection current. The SOA section was left unbiased to remove the influence of the FP cavity. Fig. 6.5 shows the measured $L-I$ curve for all 10-channels in the laser array. The threshold current for all lasers varies between 19 and 21 mA. It is clearly seen that the HR coating produces high reflection which results in such a low threshold current. The slope efficiency is about 0.17 mW/mA and it increases from the blue region to the red region. So for the lasers on the blue side the slope efficiency is around 0.15 mW/mA and for the red side it is around 0.17 mW/mA. The FP laser $L-I$ curve is also depicted in Fig. 6.5 for comparison. The output power for all lasers is more than 16 mW at 140 mA injection current.

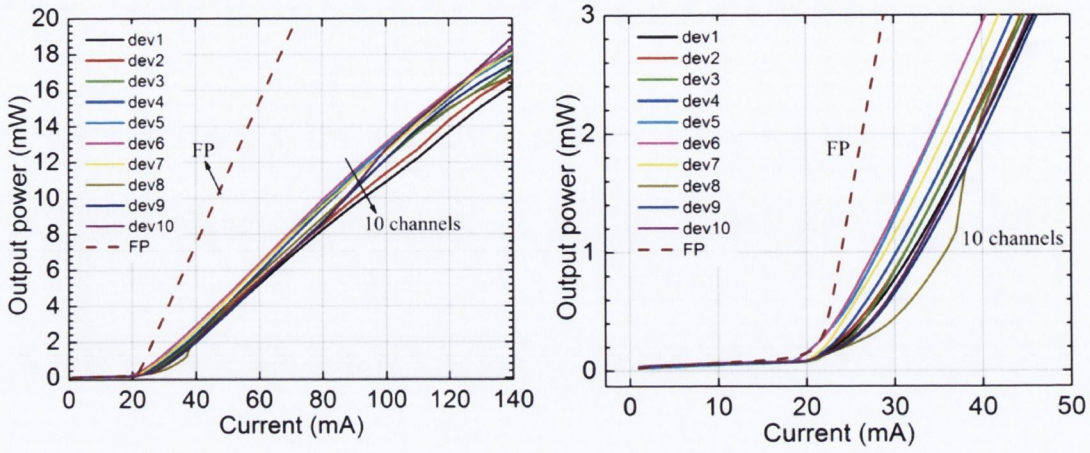

Fig. 6.5 (Left) Measured light-current (L-I) curve for all 10-channel laser and the Fabry-Perot (FP) laser on the same chip at 20°C under CW condition. (Right) Enhanced view of the region around threshold current.

The power can be further increased using semiconductor optical amplifier (SOA). The current was set at 130 mA for each laser in the array and the current of SOA was changed. Fig. 6.6 shows the measured output power as a function of SOA injection current. An output power of more than 35 mW for all channels has been obtained at SOA injection current of 70 mA. For comparison, most of the DFB laser arrays have the output power more than 15-16 mW at an injection current more than 100 mA with slope efficiency of more than 0.2 mW/mA [17]. The power can be further increased using an SOA. In [8] and [18] the DFB laser arrays integrated with an SOA have demonstrated the output power of more than 40 mW.

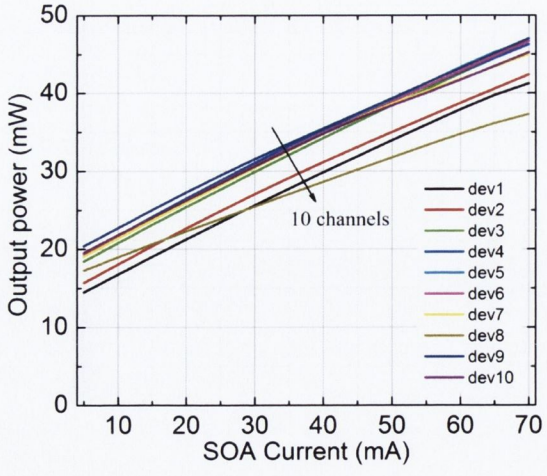

Fig. 6.6 Measured output power vs. SOA injection current.

6.2.2. Optical spectrum

To measure the optical spectrum of the laser array, a lensed fiber was used and an optical spectrum analyzer (OSA). The OSA resolution was set to its highest value of 0.06 nm. The sensitivity of the OSA was set to -80 dBm. From Fig. 6.5 some kinks in $L-I$ curve are observed. The longitudinal modes of some lasers such as 2 and 9 do not coincide well with reflection peak for these channel lasers, therefore resulting in mode hopping between the neighboured longitudinal modes as shown by the kinks from the $L-I$ curves. In our laser platform, we still need to cleave the back facet and this causes an uncertainty of cleaving position. To overcome this issue we separated the laser into two sections to adjust the back section current to obtain high SMSR. By changing the current of the back section and keeping the front section current constant it is possible to tune the position of the longitudinal mode to coincide with the relfection peak and hence to increase the SMSR. An example of such tuning is shown in Fig. 6.7 for laser 2. It was found that when we keep front current at 75 mA and give a current of 50 mA to the back section, the SMSR reached 54 dB resulting in stable single mode operation.

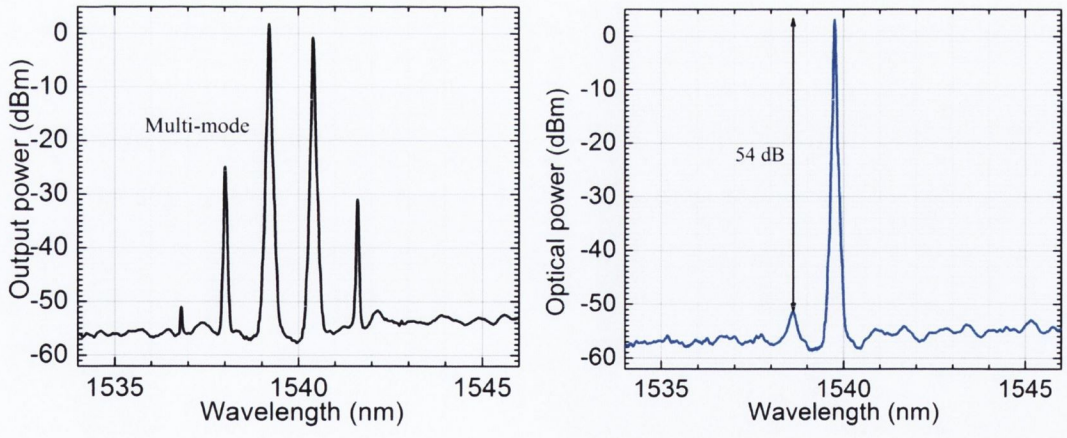

Fig. 6.7 Measured output spectrum versus back section current for the laser 2. The front section was biased at 75 mA and the back section 70 mA (left) and 50 mA (right), respectively.

The same re-tuning was used with other lasers that exhibited mode hopping. Fig. 6.8 shows the measured spectrum for laser 9. The front section of the laser was kept at 75 mA and the back section was set at 90 mA. The SMSR increased up to 57 dB.

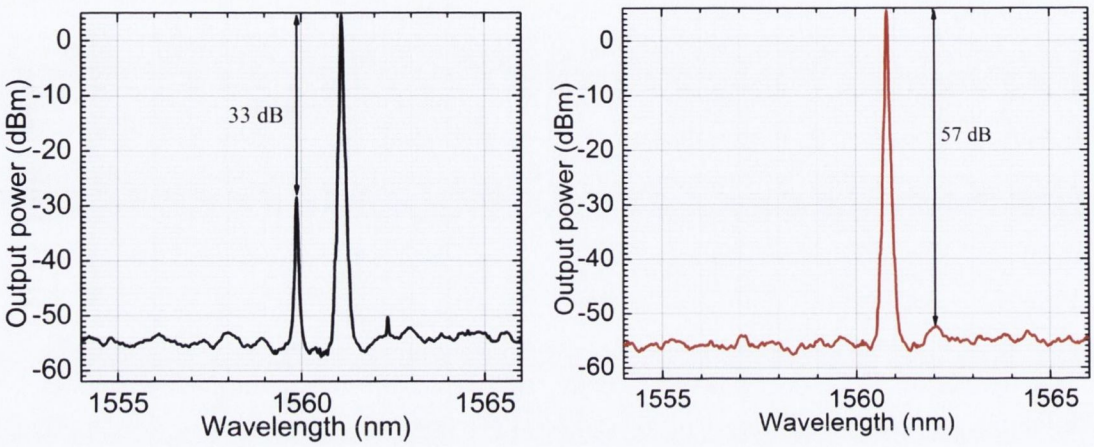

Fig. 6.8 Measured output spectrum versus back section current for the laser 9. The front section was biased at 75 mA and the back section 70 mA (left) and 90 mA (right), respectively.

By using the back section tuning demonstrated above the output spectra for all 10-channels in the array is shown in Fig. 6.9. The total current of each laser was set at 130 mA with SOA unbiased. From the figure stable single mode performance is observed with SMSR more than 50 dB for all channels. The lasing wavelengths were 1537.18, 1540.02, 1542.69, 1545.76, 1548.95, 1551.93, 1555.18, 1558.04, 1560.43 and 1563.11 nm. The wavelengths are shifted to the blue side of around 3 nm from the design. This might be due to fabrication tolerances. As was mentioned above, the wavelength is dependent on slot period therefore, fabrication inaccuracy may lead to wavelength shift. The channel spacing is different from the design as well and among all 10-channels it is within the range from 2.39 nm to 3.25 nm. This is due to the back section tuning which changed the position of some channels. Considering a temperature tuning slope of about 0.1 nm/°C, a temperature change of 32.5°C would be needed to make a wavelength tuning of 3.25 nm for each laser to cover the channel spacing. This will allow the laser to work over a wide wavelength range continuously.

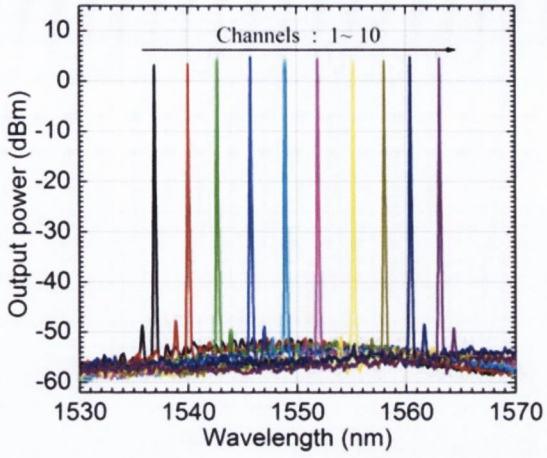

Fig. 6.9 Measured output spectrum for all 10 channels with a total drive current of 130 mA with SOA unbiased at 20°C.

To check the wavelength tuning behaviour of the laser array we kept the driving current as in the previous case at 130 mA with the SOA section unbiased. Then we changed the chip temperature through changing the temperature of the laser using the TEC. Fig. 6.10 shows the output spectra over a temperature range from 10 to 45°C with a step of 5°C.

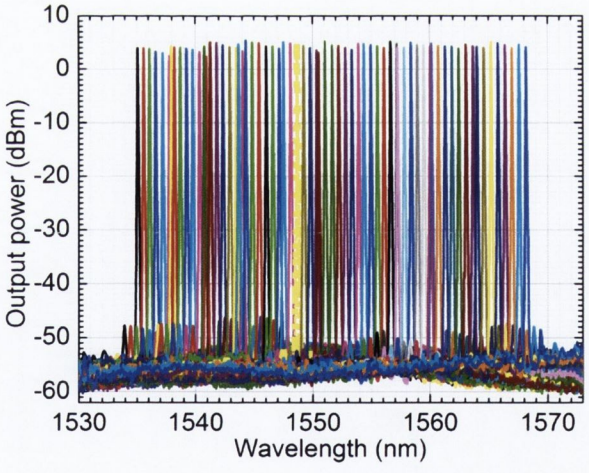

Fig. 6.10 Measured output spectra over the temperature range from 10 to 45°C.

The wavelength tuning characteristics of each laser in the array is shown in Fig. 6.11. The slotted single mode laser array can cover a wavelength range of about 31 nm from 1535 to 1565.8 nm over a 42°C (3°C to 45°C) temperature range.

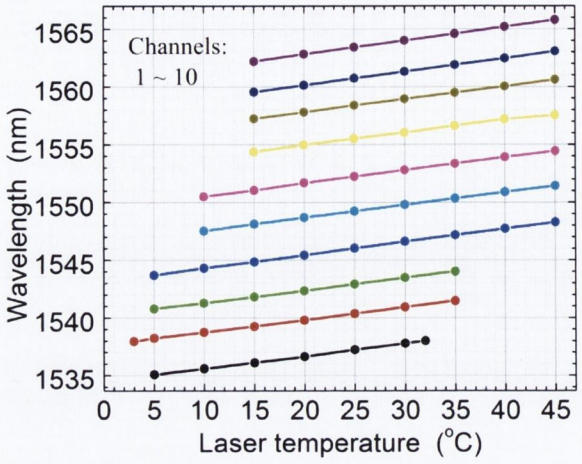

Fig. 6.11 Wavelength tuning characteristics of 10-channel slotted laser array.

The measured SMSR of the laser array for all channels as a function of lasing wavelength during the temperature tuning is shown in Fig. 6.12. An SMSR of more than 35 dB was achieved for all channels.

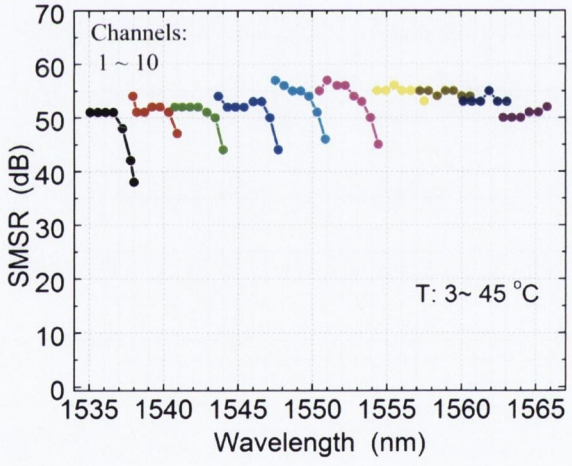

Fig. 6.12 The SMSR vs. wavelength for all channels.

The drop of the SMSR from 50 dB to 35 dB for the channels on the shorter wavelength side is caused not by competition from the modes adjacent to the lasing mode but from the mode which is one free spectral range (FSR) longer, where the FSR is determined by the slot period to be about 40 nm as shown in Fig. 6.13. Fig. 6.13 shows the output spectrum for a laser at 150 mA and it is clearly seen there is another mode at 1576 nm which is 40 nm away from the lasing wavelength. To suppress these undesirable modes non-periodically spaced slots should be used as was discussed in section 5.3.3. The laser array with different slot periods will be discussed below in section 6.3.

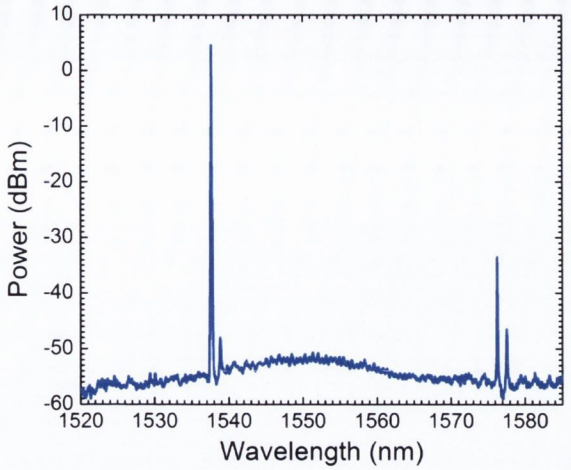

Fig. 6.13 The measured output spectrum of laser 1 at the short wavelength side of the array at 150 mA.

6.2.3. The linewidth

The linewidth of the laser array was measured using the method described in section 5.4. The delayed self-heterodyne technique was used for measurements. First, the central channel was measured, channel 6 which has a lasing wavelength around 1550 nm. The cavity length is about 400 μm. We repeated the measurements described in section 5.4.2, the linewidth dependence on output power. Device 6 was driven by an ultra-low noise current source from 50 to 150 mA at room temperature of 20°C. The SOA section was unbiased. The linewidth dependence on injection current is shown in Fig. 6.14. The behaviour is similar to what we observed in single mode lasers, the linewidth is inversely proportional to the power.

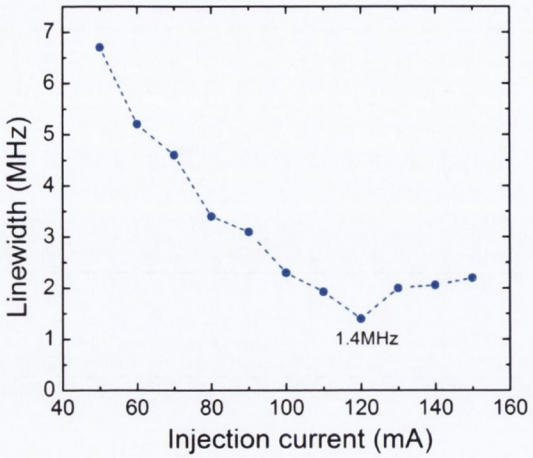

Fig. 6.14 The linewidth as a function of injection current for channel 6.

At high currents we see a slight increase in linewidth due to heat generation which causes an increase in spontaneous emission hence the linewidth become broad. The lowest linewidth of 1.4 MHz was obtained at 120 mA injection current.

Next, the linewidth of all channels of the laser array were measured according to the measurements above. Each laser in the array was driven using the ultra-low noise current source. Fig. 6.15 shows the linewidth versus current for all 10 channels. The cavity length of each laser is around 400 μm. The figure shows that all lasers have the same trend; the linewidth becomes lower by injecting more carriers in the system. It is also clearly seen that the lasers in the shorter wavelength have a higher linewidth. This is due to high mode competition in that region caused by FSR which was demonstrated before.

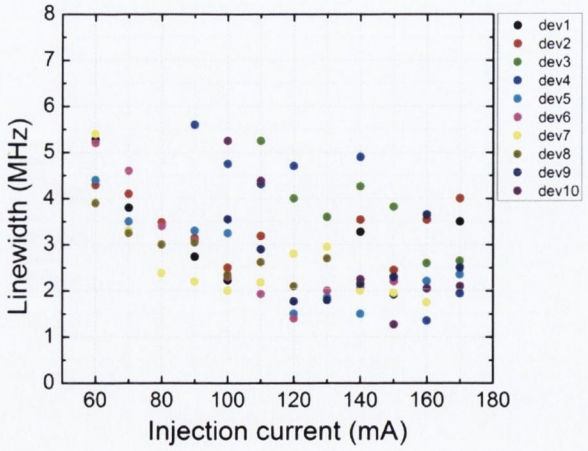

Fig. 6.15 The linewidth of 10-channel laser array vs. injection current.

The linewdith for all 10 channels is between 1.5 and 3 MHz at high currents as shown in Fig. 6.16. In this figure the lasers are driven at current about 150 mA.

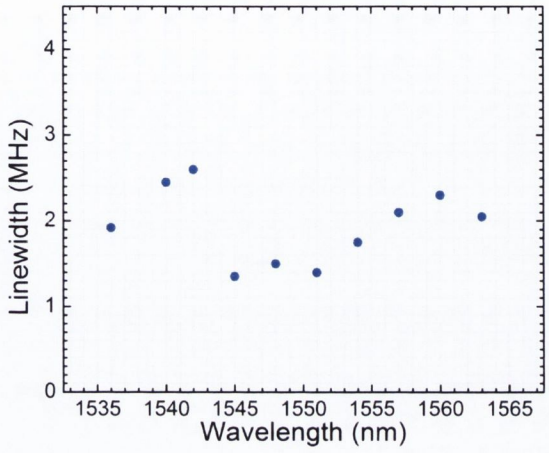

Fig. 6.16 The linewidth for all channels at 150 mA of injection current at 20°C. SOA is unbiased.

6.3. 12-channel laser array

In Fig. 6.12 we saw the drop in the SMSR for lasers in the shorter wavelength range. This was caused because of the mode which is one FSR longer, where the FSR of our grating is about 40 nm. To suppress these reflection peaks further, we used three different slot periods as we used for the laser integrated with an EA modulator discussed in section 5.3.3. The slot periods for example, for the central channel 1550 nm (dev 6) are 8.51, 9.96 and 11.4 μm. The microscope image of these slots is shown in Fig. 6.17.

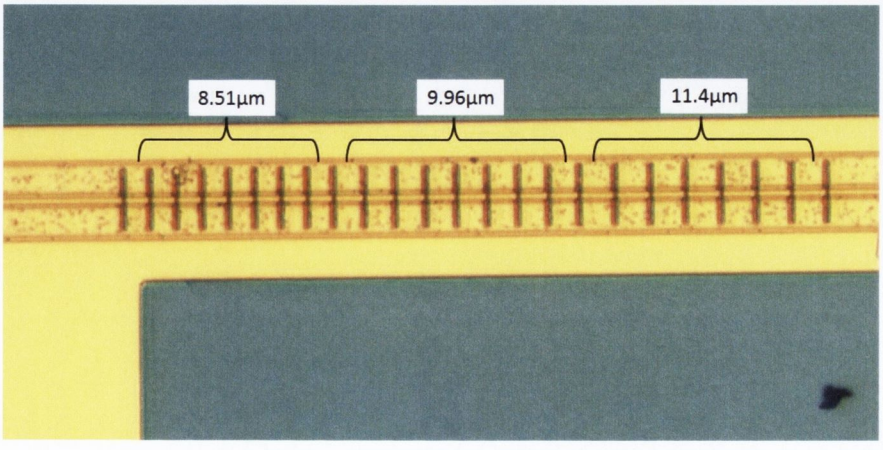

Fig. 6.17 The microscope image of non-periodically spaced slots for device 6.

For other channels the slot periods are those as shown in Table 6.1.

Devices	Slot periods (μm)		
1	8.51	9.84	11.4
2	8.51	9.86	11.4
3	8.51	9.9	11.4
4	8.51	9.92	11.4
5	8.51	9.94	11.4
6	8.51	9.96	11.4
7	8.51	9.98	11.4
8	8.51	10	11.4
9	8.51	10.02	11.4
10	8.51	10.04	11.4
11	8.51	10.06	11.4
12	8.51	10.08	11.4

Table 6.1 Three different slot periods for different devices in the 12-channel laser array.

It was mentioned above that our goal is to cover the full C-band which is 35 nm of wavelength tuning. The 10-channel laser array achieved a range of 31 nm and so we added an additional two channels to extend the tuning range. Overall the laser structure is the same as it was for the 10-channel laser array. The fabrication steps are similar to those discussed in section 5.2.2. Each laser in the array consists of laser section and integrated SOA section. The cavity length of each laser is around 400 μm. The wavelength tuning range is extended as we expected as shown in Fig. 6.18. Each laser in the array was set at 100 mA and the temperature of the chip was changed to obtain wavelength tuning. It can be seen that a wavelength quasi-continuous tuning range of about 36 nm is obtained over the 35 degree temperature range. The tuning range covers the wavelength from 1532 to 1568 nm. The total output spectrum is shown in Fig. 6.19.

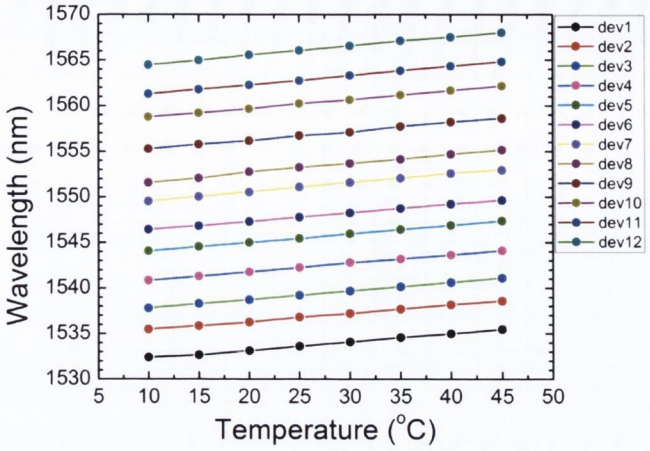

Fig. 6.18 The quasi-continuous wavelength tuning of 12-channel slotted laser array at driving current of 100 mA over the temperature range from 10 to 45°C.

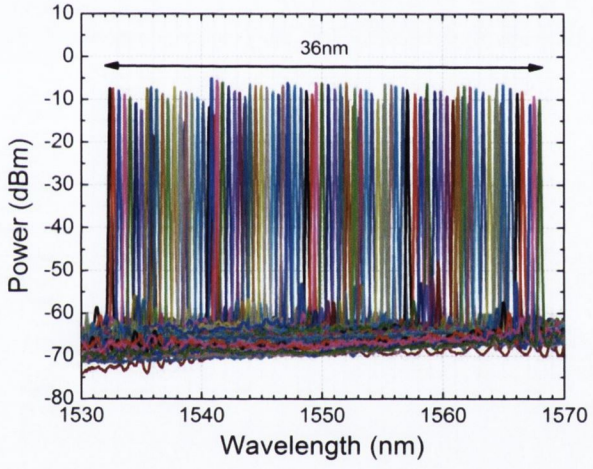

Fig. 6.19 The measured output spectrum of all 96 channels.

The SMSR for all channels during temperature change remains more than 50 dB as shown in Fig. 6.20. It is clearly seen that an improvement in SMSR in comparison with the 10-channel laser array has occurred. Non-periodically spaced slots indeed suppress the undesirable modes caused by the FSR period and the SMSR for lasers at the shorter wavelength is increased.

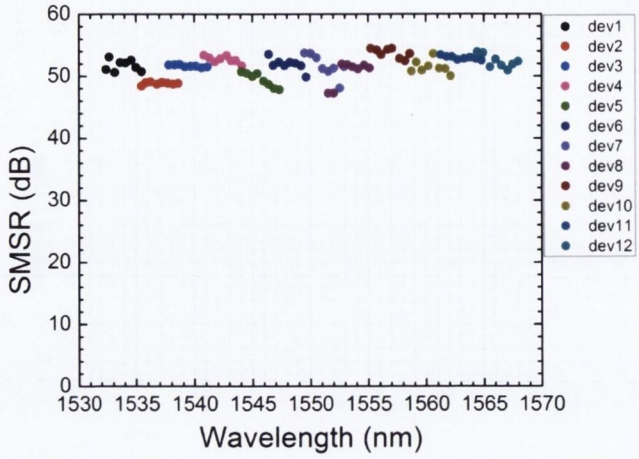

Fig. 6.20 Measured SMSR vs. wavelength for all 96 channels.

The measured $L-I$ curve shows the threshold current to be from 25 to 31 mA for all lasers at room temperature. The slope efficiency is around 0.06 mW/mA. This is shown in Fig. 6.21. The threshold current is higher and the slope efficiency is much lower than in previous run of lasers, however this is due to a fabrication process problem. The wafer has been damaged during the thinning process. We have calculated the waveguide loss using FSE method described in previous chapters. The estimated loss was 28 cm^{-1} which is higher than our previous run where the waveguide loss was 22 cm^{-1}

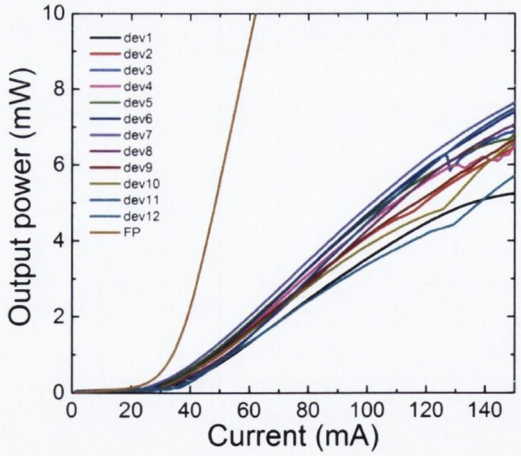

Fig. 6.21 Measured light-current $(L-I)$ curve of 12-channel laser array.

6.3.1. The linewidth characterization

The linewidth of the laser array with non-periodically spaced slots is similar to the laser with the equally spaced slots. The linewidth remains around 3 MHz for all channels at high currents as shown in Fig. 6.22. These lasers have cavity length of around 400 μm.

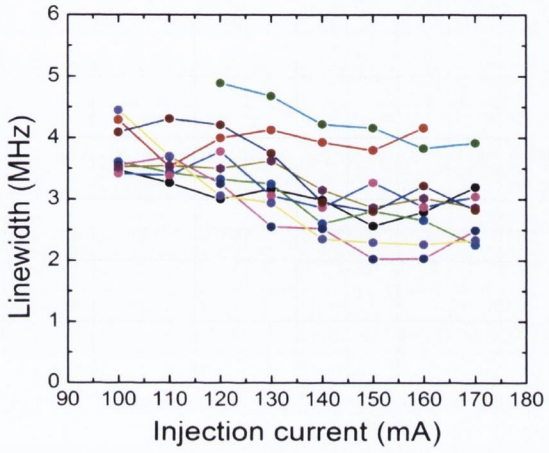

Fig. 6.22 The linewidth as a function of injected current for a laser array with different slot periods with cavity length of 400 μm.

In this run we characterized lasers with a longer cavity length, e.g. 700 μm and 1000 μm to see how the linewidth might be improved. The lasers with different cavity length are shown in Fig. 6.23. We kept the length of the slotted region the same and extended only the non-slotted part.

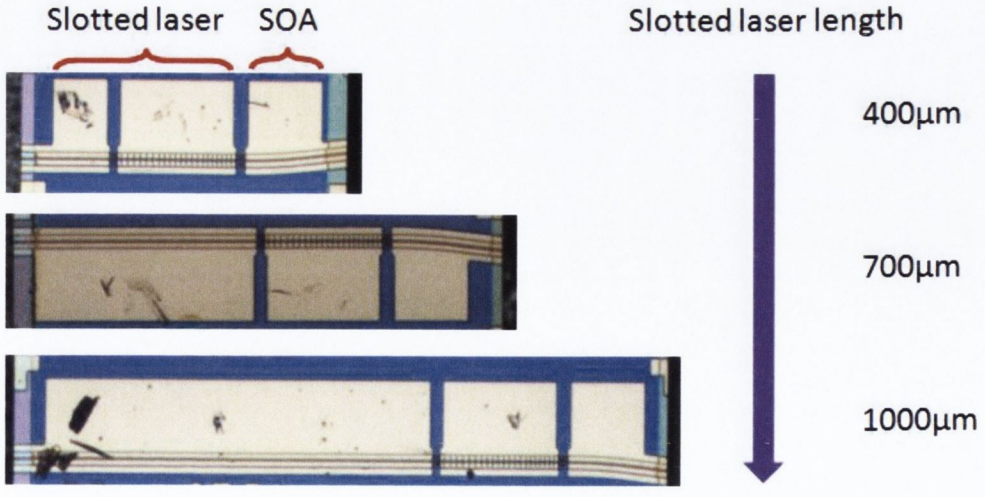

Fig. 6.23 The microscope image of individual lasers with different cavity lengths of 400, 700 and 1000 μm.

First, the 700 μm laser array was characterized. The threshold current for all lasers is around 30 mA as shown in Fig. 6.24.

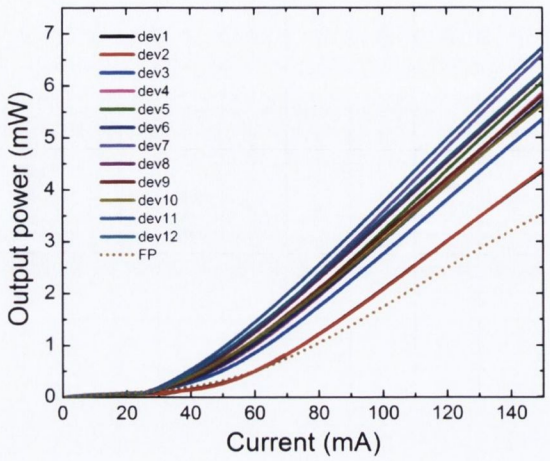

Fig. 6.24 Measured light-current ($L-I$) curve for a 12-channel laser array with cavity length of 700 μm at room temperature under CW condition.

The SMSR for all lasers is around 45 dB which is bit lower than in 400 μm lasers because in the longer lasers the mode spacing is smaller than in shorter lasers and hence the adjacent modes are positioned closer to the lasing peak. This means that the adjacent modes will rise with the main lasing wavelength, resulting in mode competition and hence lower SMSR as shown in Fig. 6.25. The front and back sections of the lasers were connected and biased together with a total current of 100 mA. The mode spacing for the laser with 700 μm cavity length is 0.61 nm. All lasers show stable single mode operation during temperature tuning. The wavelength tuning of 37 nm was obtained over a temperature range from 10 to 45°C.

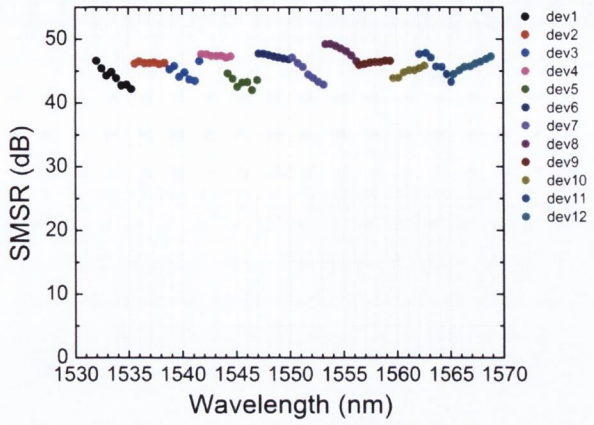

Fig. 6.25 Measured SMSR vs. wavelength for the 12-channel laser array with a cavity length of 700 μm.

We measured the linewidth for 700 μm as a function of the laser diode current. The current is given through the low noise current source. The SOA section is unbiased and the temperature of the chip was set to 20°C. Fig. 6.26 shows the linewidth as a function of injection current for 700 μm and 400 μm lasers in the same graph. As was mentioned and demonstrated in the previous chapter, as the cavity length increases, the linewidth decreases. The linewidth for 700 μm laser is around 700 kHz for all 12 channels at 190 mA injection current. It is also seen that periodic change in linewidth in the longer lasers is smaller in comparison with shorter lasers. This can be explained due to external feedback from the end of the SOA section. Although, the SOA section is angled to 7^{o} from the normal of the facet, there is still some fraction of light that will be reflected back to the cavity and influence the linewidth variation. The external feedback influence on linewidth variation has been reported for DFB laser arrays [19], [20]. It has been demonstrated that the external feedback is inversely proportional to the laser cavity length [19]. Therefore, longer lasers decrease the linewidth variation. Fig. 6.27 shows the summary linewidth for all channels at high currents (around 180 mA) for lasers with effective cavity length of 400 μm and 700 μm.

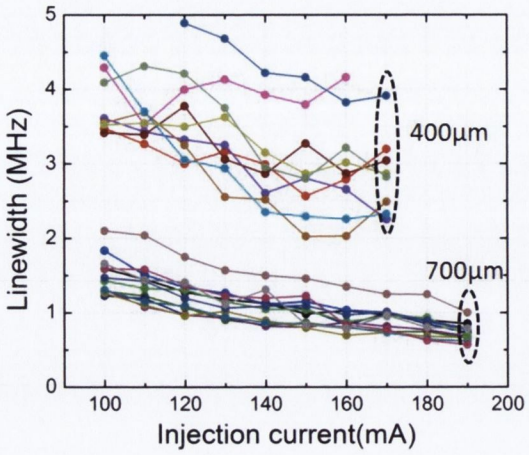

Fig. 6.26 Measured linewidth as a function of injection current for laser arrays with cavity length of 400 μm and 700 μm.

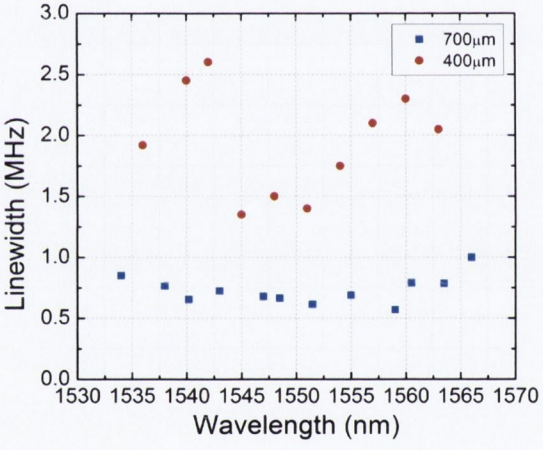

Fig. 6.27 The measured linewidth for different channels of laser array at 190 mA for lasers with effective cavity length of 400 μm and 700 μm.

It was mentioned above the lasers with longer cavity length have adjacent modes closer to the lasing mode and hence this will affect the SMSR. The laser array with cavity length of 1000 μm has an SMSR for all channels of around 40 dB as shown in Fig. 6.28. The mode spacing in 1000 μm lasers is now just 0.39 nm. The linewidth for all channels is less than 500 kHz at 190 mA as demonstrated in Fig. 6.29. The tuning range is around 36 nm over 30°C of temperature tuning.

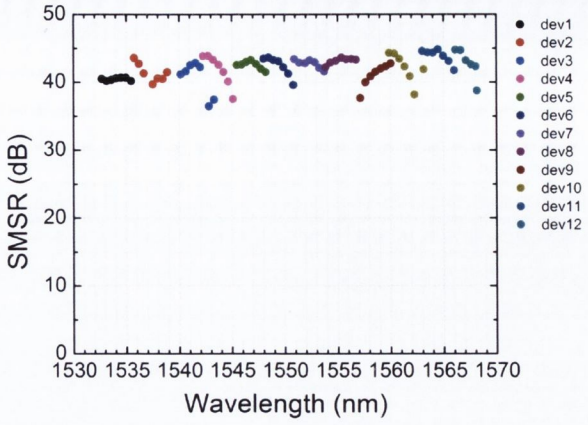

Fig. 6.28 Measured SMSR as a function of wavelength for laser array with cavity length of 1000 μm.

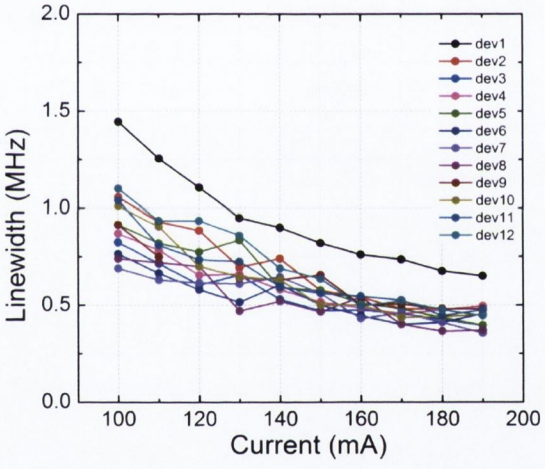

Fig. 6.29 Measured linewidth as a function of injection current for laser arrays with cavity length of 1000 μm.

Considering the results presented above Fig. 6.30 and Fig. 6.31 show the comparison in SMSR and linewidth of all three different cavity lengths. Fig. 6.30 clearly shows that the SMSR is lower as cavity length gets longer. So for lasers with 400 μm cavity length the SMSR is more than 50 dB, for 700 μm the SMSR is around 45 dB and for 1000 μm the SMSR is around 40 dB. In case of the linewidth the situation is reversed. The linewidth gets narrower with the cavity length as shown in Fig. 6.31 and reaches a value below 500 kHz for 1000 μm lasers. However, there are some negative sides of long lasers. A very long laser cavity will result in high laser threshold current and low SMSR. Therefore, there is a trade-off between reducing the linewidth and keeping low threshold current with high enough SMSR. In section 5.4.2 we have shown the linewidth variation for different slot widths. The overall

trend was the same for different slot widths but the values were different. We are now studying how the slot parameters along with the cavity length will affect the linewidth. In particularly, how the slot depth will change the linewidth. We have already demonstrated a model that characterizes the linewidth as a function of slot depth [21]. For an ideal case, a laser cavity length must be 1.5 mm long. The linewidth of the laser decreases nonlinearly as the slot depth increases due to increase in reflection coefficient and reaches a value below 400 kHz. We believe that by optimizing the slot parameters in terms of width and depth, we can design the slotted laser with a predetermined narrow linewidth.

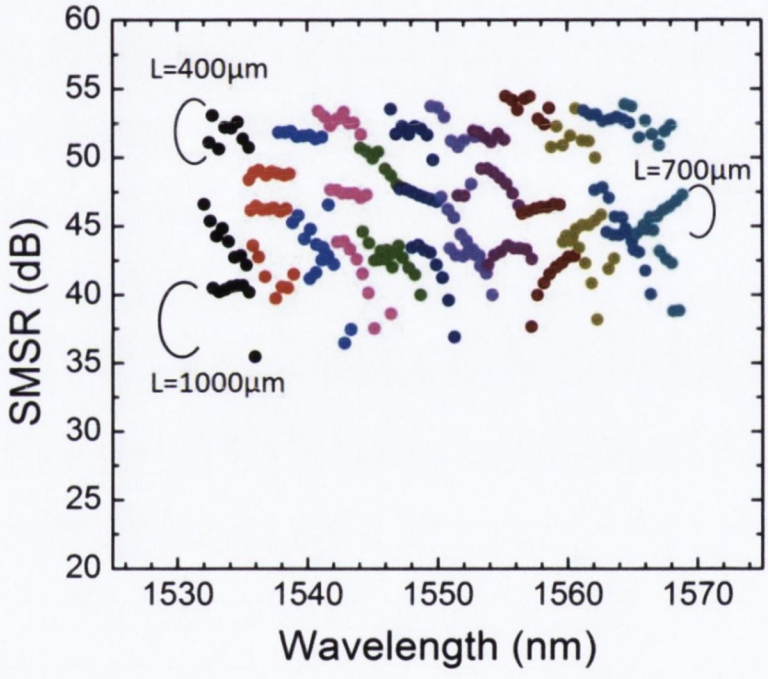

Fig. 6.30 Measured SMSR as a function of wavelength for different cavity lengths, e.g. 400 μm, 700 μm and 1000 μm.

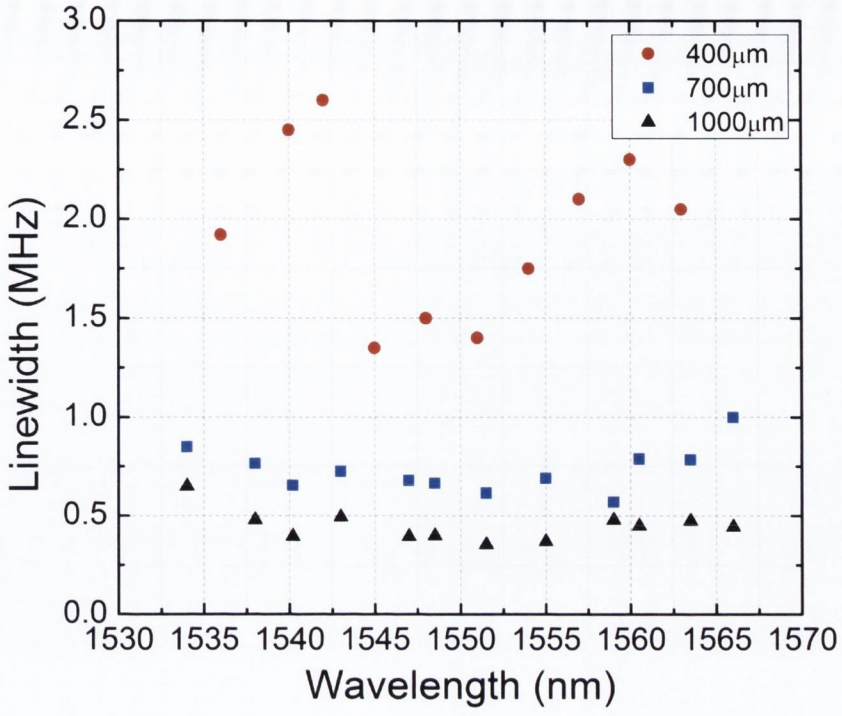

Fig. 6.31 Measured linewidth for different channels of the laser array at 190 mA for lasers with cavity length of 400 μm, 700 μm and 1000 μm.

6.4. Thermal crosstalk

The high-speed and high-accuracy wavelength switching of tunable lasers are important features in DWDM systems. High-speed wavelength switching is achieved in SGDBR lasers and super structure grating (SSG) DBR lasers where wavelength tuning can be obtained by current injection [1] [22]. However, such lasers suffer from undesirable slow frequency shift caused by thermal drift which resulted from heating due to the current injection. On the other hand, stable wavelength tuning with high accuracy can be obtained in tunable laser arrays without any mode hopping although the switching is now being dominated by thermal effects. Nevertheless, in a closely spaced laser array thermal crosstalk between the lasers can still be an issue. Generally, the output wavelength of a selected laser in the laser array is not affected by the neighboring laser since in general one laser operates at a time. However, once another laser is activated, the heat generated by the adjacent laser will drift to the selected laser and hence will de-tune the laser. This effect is also called localized heating impact. In terms of packaging and size of the chip, the lasers in the laser array

should be spaced close to each other, thus localized heating impact will be higher. In the present array, our devices are very far apart (310 μm). With the localized heating impact there is an issue with thermal properties of the material. It is well known that poor thermal management can lead to low laser efficiency. Poor heat dissipation at high currents will result in low output power and poor laser performance. According to this the thermal properties of materials should be investigated and managed. The thermal conductivity of InP material is not high as compared to Si [23]. Hence the thermal resistance in InP materials will be higher which will prevent efficient heat dissipation. So in this section we will discuss the thermal properties of our InP-based tunable laser array. First, the overall the temperature characteristics will be given. Then the effect of localized heating impact or thermal crosstalk and the last test will be the increase in the active region temperature as a function of input power, or the thermal impedance.

The first step in thermal characterization of the laser array is to measure the overall characteristic temperature. The characteristic temperature can be described through (6.2),

$$I_{th} = I_0 e^{T/T_0}, \tag{6.2}$$

where T is the laser temperature and T_0 is the characteristic temperature. It is seen that the threshold current of the laser will increase exponentially with the temperature. To define T_0 we measured the $L - I$ curve at different temperatures. We chose the central channel in the 10-channel laser array, device 5. The temperature was changed between 15 to 65°C using the TEC. Fig. 6.32 shows $L - I$ curve at different temperatures. The threshold current at 15°C and 65°C is around 16 mA and 33 mA, respectively. According to this measurements and equation (6.2), we found T_0 to be around 69.4 K. In [24], it is stated that for good near-infrared (-850 μm) GaAs/AlGaAs DH lasers, the observed T_0 is around 120 K. For quantum-well GaAs/AlGaAs the values are between 150 and 180 K. And for 1.33-1.55 μm InGaAsP/InP lasers T_0 is around 50 to 70 K. Such low T_0 is explained due to Auger recombination and current leakage [24]. Thereby, the characteristic temperature of our lasers is quite good even though, we have used standard commercial wafer without any optimization in terms of thermal aspect. Table 6.2 shows the thermal conductivity for each layer of our wafer.

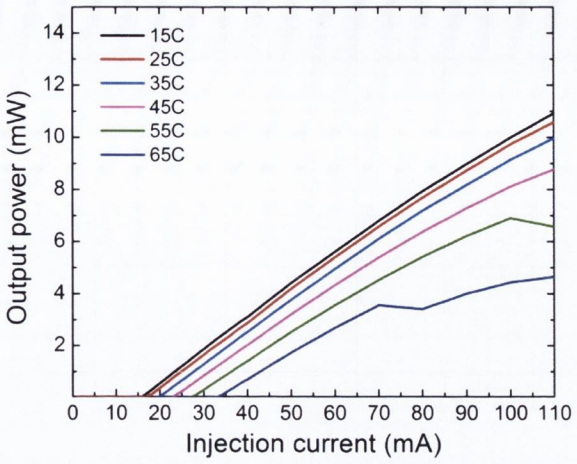

Fig. 6.32 Measured $L - I$ curve for device 5 at temperatures between 15 to 65°C.

Material	Thermal Conductivity (W/m-K)	Specific Heat (J/kg-K)	Thickness (μm)
InGaAs	5	300	0.2
InGaAs0.62P	6.735	300	0.05
InGaAs0.33P	23.2025	300	0.02
InP	68	310	0.8 (N); 1.65 (P)
P-Contact-Metal	208.34	178.24	0.425
N-Contact-Metal	317	129	0.675
SiO2	1.4	1000	0.3
Solder	20	2180	10
AIN	175	600	620
MQW	5	380	0.34

Table 6.2 Thermal specifications of the standard commercial IQE wafer.

The second step in thermal characterization is the thermal crosstalk effect. The thermal crosstalk between the devices is measured by measuring the change in characteristics of particular device with change in current through the neighboring devices. In our case we chose device 5 as the particular device and changed the current in neighboring lasers. The light from device 5 was collected through a lensed fiber and the spectrum was recorded using an OSA. The schematic view of the 10-channel laser array is again shown in Fig. 6.33.

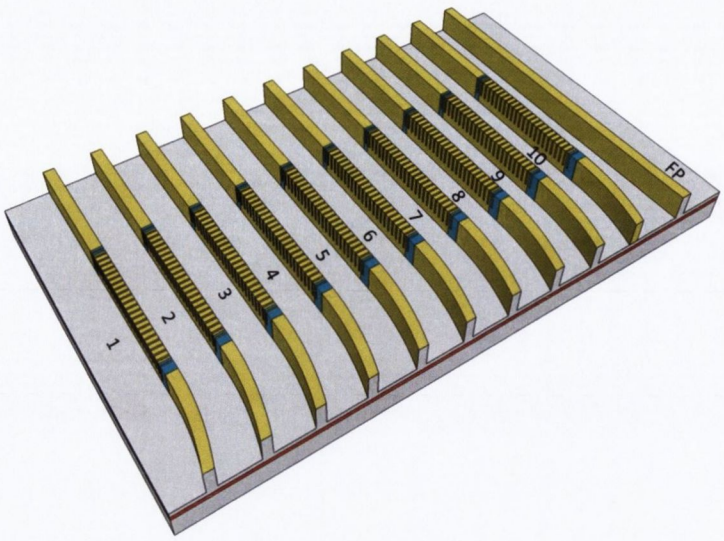

Fig. 6.33 3-D schematic structure of slotted 10-channel laser array.

Fig. 6.34 shows the change in output spectrum of device 5 as the current in device 4 varied. The lasing peak of device 5 is at 1546.89 nm and the current in device 4 was varied from 0 to 100 mA with step of 20 mA. The chip temperature was set at 20°C. It is clearly seen that when neighbouring laser is turned "on" the wavelength of device 5 is red shifted due to the heat generation. There is no thermal or electrical isolation between the lasers therefore the heat from the neighboring lasers will drift to device 5 and shift the wavelength peak to the longer side. So when device 4 is set at 100 mA the wavelength of device 5 is red shifted by 0.43 nm along with a slight decrease in the SMSR.

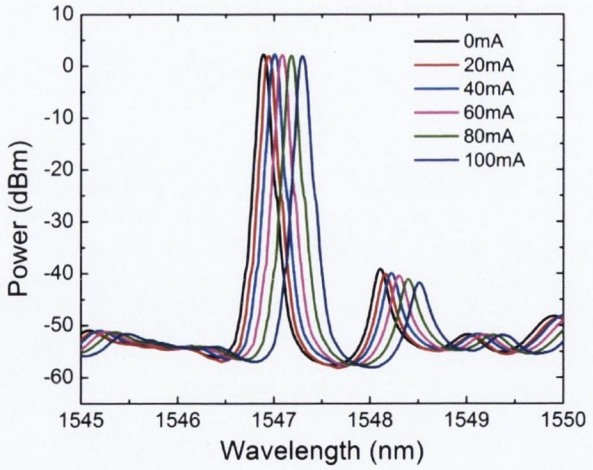

Fig. 6.34 Measured output spectrum of device 5 with the effect of neighbouring device 4.

The next step was to see how other neighboring lasers will affect device 5. The distance between the devices is around 310 μm as depicted in Fig. 6.35.

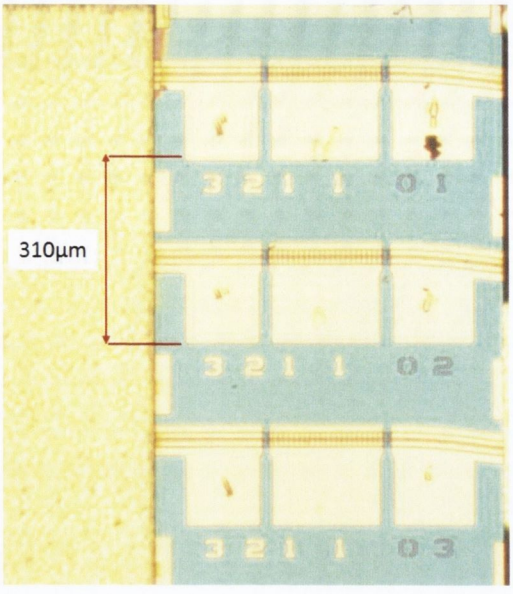

Fig. 6.35 The microscope image (top view) of three devices.

In Table 6.3 the distances of different devices from device 5 is shown.

Device	Distance (μm)
1	1240
2	930
3	620
4	310
6	310
7	620
8	930
9	1240
10	1560

Table 6.3 Distances of neighboring lasers from device 5.

According to Table 6.3 the closest lasers to device 5 should have a bigger thermal crosstalk effect in comparison with the devices which are far away. We measured how other devices affect device 5 when they are turned on. The wavelength shift of device 5 is shown in Fig. 6.36. The x axis represents different channels with specific wavelength. The y axis represents wavelength peak change of device 5. So when device 1 ($\lambda_0 = 1536\,nm$) is turned on (driven at 100 mA), the wavelength peak of device 5 is shifted by 0.3 nm. As mentioned above the lasing peak of device 5 is at 1546.89 nm hence the lasing peak of device 5 is 1547.19 nm when device 1 is turned on. It can be seen from the figure that the

closest lasers have the greater impact on device 5, so device 4 and device 6 produce a wavelength shift of 0.43 nm. This might be due to different thermal properties along the laser array. However when the lasers in the end such as device 9 and 10 are on the wavelength shift increased even though they are placed far away from device 5. This effect has been observed in [25], [26] and might be because of the temperature rise in the heat sink. How it was mentioned above we used copper heat sink. In [25] authors calculated the thermal crosstalk neglecting the heat sink temperature and found that the thermal crosstalk is negligibly small for distant lasers. They demonstrated that the heat sink with higher thermal conductivity, in their case a diamond heat sink (20 W/(cm °C)) will reduce the thermal crosstalk to about 1/3 in comparison with silicon heat sink (1.5 W/(cm °C)).

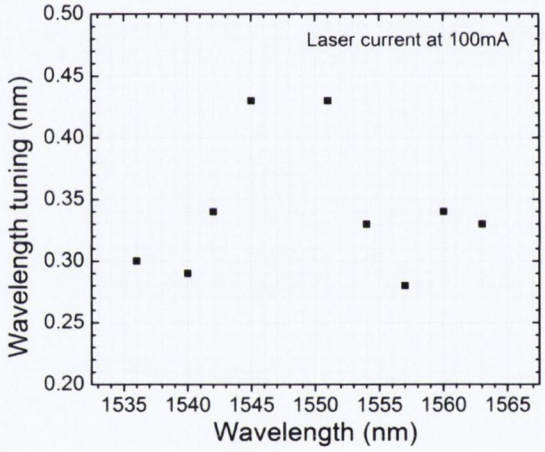

Fig. 6.36 Thermal crosstalk effect of neighbouring lasers to device 5.

The temperature rise in device 5 has also been measured as a function of dissipated electrical power of neighboring devices. The temperature rise is calculated by measuring the wavelength shift and then determining the corresponding temperature rise from the slope which is shown in Fig. 6.37. The tuning scope is about 0.11 nm/^{o}C, a standard value for telecommunication semiconductor lasers.

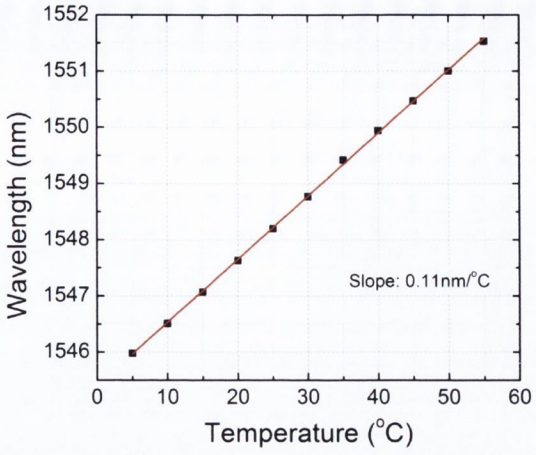

Fig. 6.37 Wavelength dependence on chip temperature of device 5.

According to Figs. 6.36 and 6.37 we measured the temperature rise in device 5 with changing injection current in neighboring lasers which is shown in Fig. 6.38 (left) and (right). Fig. 6.38 (left) shows the temperature rise in device 5 when the lasers from 1 to 4 are turned on, Fig. 6.38 (right) shows when the lasers from 6 to 10 are turned on. From the figures it is seen that at high currents the temperature in device 5 rises from 4 to 8°C according to which neighboring laser is turned on.

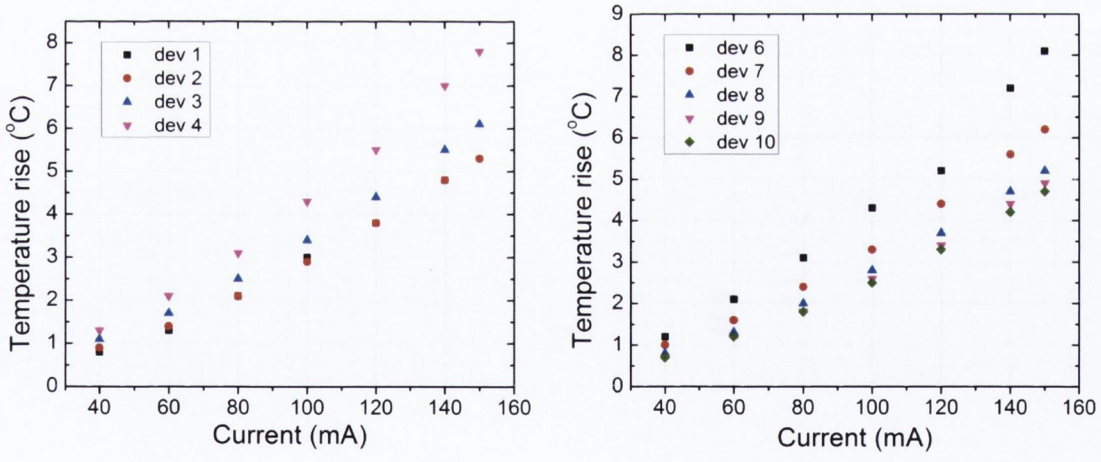

Fig. 6.38 Temperature rise in device 5 vs. Injection current in neighboring lasers: (Left) from device 1 to device 4. (Right) From device 6 to device 10.

The last step in thermal characterization of the slotted laser array is the thermal impedance. The thermal impedance is a parameter which evaluates the temperature rise in the active region as a function of dissipating electrical power. In InP-based lasers, the heat

generated in the active region tends to remain there due to the high thermal impedance. The temperature rise in [24] is given as

$$\Delta T = P_D Z_T \tag{6.3}$$

where Z_T is the thermal impedance and P_D is the dissipated power which can be found by

$$P_D = P_{in} - P_o, \tag{6.4}$$

where P_{in} is the electrical power supplied to the laser and can be expressed as

$$P_{in} = I^2 R_s + IV_d + IV_s. \tag{6.5}$$

P_0 is the optical power out of the laser and expressed as

$$P_o = \eta_i \left(\frac{\alpha_m}{\langle \alpha_i \rangle + \alpha_m}\right) \frac{h\vartheta}{q} (I - I_{th}). \tag{6.6}$$

The details of derivation of (6.5) and (6.6) can be found in [24].

To measure the thermal impedance of our lasers we used a combination of two experiments which are described in [27]. The first experiment was used to estimate the wavelength shift of the laser as a function of active region temperature or the chip temperature in our case $d\lambda/dT$. The lasers were driven using a pulsed current source to ensure that there is no parasitic heating from the power dissipation. In the second experiment was performed a continuous wave (CW) source to measure the wavelength shift dependence on applied electrical power $d\lambda/dP$. The thermal impedance is the ratio of measured $d\lambda/dT$ and $d\lambda/dP$ as shown in (6.7) and it is similar to (6.3)

$$Z_t = \frac{d\lambda/dP}{d\lambda/dT}. \tag{6.7}$$

In the first experiment for measurement of the wavelength shift of the laser as a function of temperature we used pulsed current source to drive the laser. The pulse width set to be 1 μs, the duty cycle is 0.1% and the current set at 100 mA. The temperature of the chip was varied from 17 to 25°C with the step of 2°C and we recorded the shift in the wavelength

using OSA. The resolution of the OSA was set at 0.06 nm with sensitivity of -75 dBm. In Fig. 6.39 the wavelength shift as a function of chip temperature for device 5 is shown. The behavior is linear with tuning scope of 0.094 nm/°C.

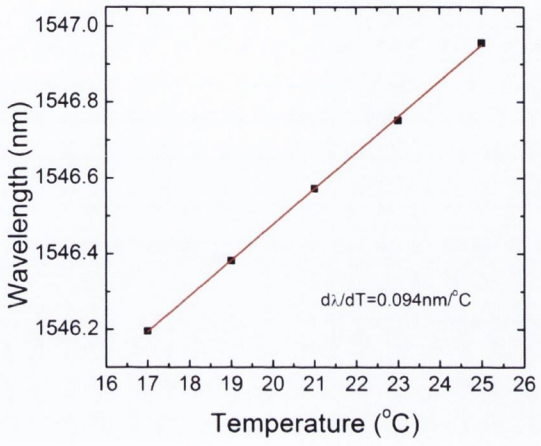

Fig. 6.39. Wavelength shift of slotted laser as a function of chip temperature under pulsed condition for device 5.

For the second experiment to measure the wavelength shift as a function of dissipated electrical power we used a continuous wave (CW) condition at a room temperature of 20°C. We set the chip temperature at constant 20°C and supplied current to the laser using a standard current source, in our case we used a Keithley 2400-C source meter. We recorded again the wavelength shift of the lasing peak but this time as a function of applied electrical power. Fig. 6.40 shows the wavelength dependence on input power. The tuning scope is 7.069 nm/W as shown in Fig. 6.40. Thus we found $d\lambda/dP = 7.069\ nm/W$.

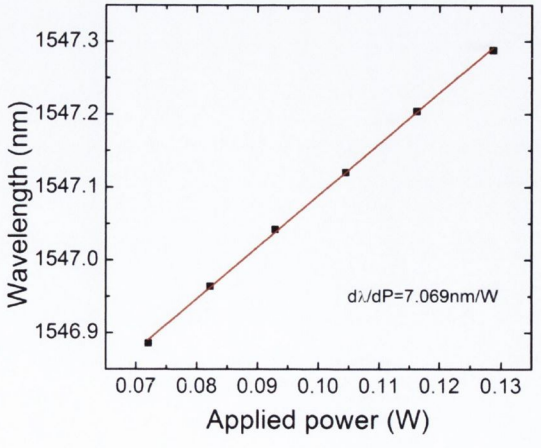

Fig. 6.40 Wavelength shift as a function of dissipated electrical power under CW condition.

Combining the results measured above we extracted the thermal impedance of device 5 to be $Z_T = 74.8\,°C/W$. We applied these measurements to the rest of lasers. Table 6.4 shows the thermal impedance for all devices in the laser array except for device 6 which was damaged during the experiments. From Table 6.4 it is clear that the thermal impedance for all lasers is uniform and it remains around 75°C/W. For comparison, the thermal impedance of a FP laser on the same sub-mount is 89.1 °C/W.

Device	Thermal impedance (Z_T) (°C/W)
1	74.6
2	76.4
3	79
4	76.4
5	74.8
6	-
7	68.9
8	72.7
9	78.3
10	77.5

Table 6.4 Thermal impedance for various devices in the 10-channel laser array.

It is obvious that the thermal impedance is quite high for our lasers. This will degrade the laser performance due to bad heat dissipation. Therefore, the laser structure and material structure must be optimized to efficiently extract the generated heat. Generally, the heat in typical laser structures is dissipated via p-side cladding layer. Thereby, the thermal resistance (conductivity) of the p-cladding layer should be low (high). It is well known that the thermal conductivity of aluminum containing materials is higher than phosphide containing materials. In [28], the thermal conductivity of AlGaAs material is calculated to be 22 W/m-K while for our materials according to Table 6.2, the thermal conductivity is around 6 W/m-K. In addition, the linewidth enhancement factor for Al containing materials is lower than P system [29]. Therefore, the material structure should be optimized. Another way of extracting the heat from the upper p-side part of the laser is to increase the thickness of the top metallization part. Essentially, it is the simplest way. It has been reported that by making it thicker, the thermal resistance can be reduced by ~21% and for very thick layers such as 3-μm and 5-μm, the thermal resistance reduced by ~24% [30].

It has been also reported that the thermal resistance is dependent on cavity length. By making the cavity longer, it is possible to reduce the thermal resistance because the heat dissipates well in large areas [31], [32]. In [31], researchers proposed another way of extracting the heat. The idea is to mount a thermally conductive heat-bypass structure, in their case they used heat-pass-wire over the laser chip and connected it with submount. So the heat from the top of the laser chip will spread through this bypass structure into the submount. They demonstrated the reduction in thermal resistance by ~50%.

6.5. Conclusion

We have developed wavelength tunable slotted single mode laser arrays for WDM and coherent communication systems. Two types of slotted laser arrays were presented in this chapter. First, a 10-channel laser array with periodically spaced slots was demonstrated. Wavelength tuning of 31 nm was achieved with SMSR more than 35 dB for all channels. We observed a drop in the SMSR which was due to the modes which are one free spectral range away from the gain peak. To suppress these modes the new design was developed using non-periodically spaced slots. In the new design we implemented three different slot periods in the laser structure to suppress these undesirable modes. From the experiments it was found that the SMSR was improved much and remained more than 50 dB for all channels. Also, in the new design two more additional channels were added to the laser array to increase the wavelength tunability. The wavelength tuning of 36 nm was obtained which means that the slotted laser array covers the full C-band.

The spectral linewidth of both types of laser arrays were investigated. The experiments show that the linewidth varies between 2 and 4 MHz for short cavity lasers. The broad spectral linewidth has negative consequences in coherent communication systems. Therefore, the long cavity length laser arrays were fabricated to improve the linewidth. The laser array with cavity length of 1 mm approached a value below 500 kHz for all channels. This makes these lasers suitable for coherent communication systems. Also, it was observed that the long cavity lasers are less sensitive to the linewidth variation due to the effect of external feedback.

The thermal properties have also been investigated. As was seen from the experiments the localized heating impact will affect the laser wavelength and shift it to the longer wavelengths. This might be an important issue in optical communications where the main requirement is the stable single mode operation and emission at exact same wavelength as specified by ITU-T standards. Also from the thermal analysis we have estimated the thermal impedance of our lasers which is around 75 °C/W for all lasers in the array. This value is higher than for example Al containing materials. Therefore, the material and laser structure should be optimized in terms of thermal aspects as was discussed above.

References

[1] V. Jayaraman, Z. M. Chuang and L. A. and Coldren, "Theory, Design, and Performance of extended tuning range semiconductor lasers with sampled gratings," *IEEE J. Quantum Electronics,* vol. 29, no. 6, pp. 1824-1834, 1993.

[2] M. Oberg, S. Nilsson, K. Streubel, J. Wallin, L. Backborn and T. Klinga, "74 nm wavelength tuning range of an InGaAsP/InP vertical grating assisted codirectional laser with rear sampled grating reflector," *IEEE Photonics Technology Letters,* vol. 5, pp. 735-738, 1993.

[3] B. Pezeshki, E. Vail, J. Kubicky, G. Yoffe, S. Zou, J. Heanue, P. Epp, S. Rishton, D. Ton, B. Faraji, M. Emanuel, X. Hong, M. Sherback, V. Agrawal, C. Chipman and T. Razazan, "20-mW Widely Tunable Laser Module Using DFB Array and MEMS Selection," *IEEE Photonic Technology Letters,* vol. 14, no. 10, pp. 1547-1459, 2002.

[4] J. De Merlier, K. Mizutani, S. Sudo, K. Naniwae, Y. Furushima, S. Sato, K. Sato and K. Kudo, "Full C-Band External Cavity Wavelength Tunable Laser Using a Liquid-Crystal-Based Tunable Mirror," *IEEE Photonics Technology Letters,* vol. 17, no. 3, pp. 681-683, 2005.

[5] K. J. Knoop, D. Vakhshoori, P. D. Wang, M. Azimi, M. Jiang, P. Chen, P. Matsui, K. McCallion, A. Baliga, F. Sakhitab, M. Letsch, B. Johnson, R. Huang, A. Jean, B. DeLargy, C. Pinzone, F. Fan, J. Liu, C. Lu, J. Zhou, H. Zhu and R. Gurjar, "High power MEMs-tunable vertical-cavity surface emitting lasers," *Proc. Advanced Semiconductor Lasers, Dig. LEOS Summer Topical Meet., Copper Mountain,* pp. 31-32, 2001.

[6] N. Natakeyama, K. Naniwae, K. Kudo, N. Suzuki, S. Sudo, S. Ae, Y. Muroya, K. Yashiki, S. Satoh, T. Morimoto, K. Mori and T. Sasaki, "Wavelength -Selectable microarray light sources for S-, C-, and L-band WDM systems," *IEEE Photonic Technology Letters,* vol. 15, pp. 903-905, 2003.

[7] H. Oohashi, Y. Shibata, H. Ishii, Y. Kawaguchi, Y. Kondo, Y. Yoshikuni and Y. Tohmori, "46.9-nm wavelength-selectable arrayed DFB lasers with integrated MMI coupler and SOA," *Proc. Induim Phosphide Relat. Mater.,* pp. 575-578, 2001.

[8] H. Ishii, K. Kasaya, H. Oohashi, Y. Shibata, H. Yasaka and K. Okamoto, "Widely wavelength-tunable DFB laser array integrated with funnel combiner," *IEEE Journal of Selected Topics in Quantum Electronics,* vol. 13, no. 5, pp. 1089-1094, 2007.

[9] J. E. Simsarian, M. C. Larson, H. E. Garrett, H. Xu and T. A. Strand, "Less than 5-ns wavelength switching with an SG-DBR laser," *IEEE Photonics Technology Letters,* vol. 18, no. 4, pp. 565-567, 2006.

[10] T. Kaneko, Y. Yamauchi, H. Tanaka, T. Machida, T. Ishikawa, T. Fujii and H. Shoji, "High-power and Low Phase Noise Full-band Tunable LD for Coherent Applications," *Proc. of Opt. Fiber Commun. Conf., San Diego,* 2010.

[11] A. Sivananthan, H.-C. Park, M. Lu, J. S. Parker, E. Bloch, L. A. Johansson, M. J. Rodwell and L. A. Coldren, "Monolithic lienwidth narrowing of a tunable SG-DBR laser," in *Optical Fiber Communications Conference* , Anaheim, California United States, 2013.

[12] H. Ishii, H. Oohashi, K. Kasaya, K. Tsuzuki and Y. Tohmori, "High-power (40mW) L-band tunable DFB laser array module using current tuning," in *Optics Fiber Communication Conference*, Anaheim, CA, 2005.

[13] H. Ishii, K. Kasaya and H. Ooshashi, "Narrow spectral linewidth operation (<160kHz) in widely tunable distributed feedback lasers," *Electronics Letters,* vol. 46, no. 10, 2010.

[14] K. Tsuzuki, Y. Shibata, N. Kikuchi, M. Ishikawa, T. Yasui, H. Ishii and H. Yasaka, "Full C-band tunable DFB laser array copackaged with InP Mach-Zehnder modulator for DWDM optical communication systems," *IEEE Journal of Selected Topics in Quantum Electronics,* vol. 15, no. 3, pp. 521-527, 2009.

[15] T. Fujisawa, S. Kanazawa, K. Takahata, W. Kobayashi, T. Tadokoro, H. Ishii and F. Kano, "1.3-μm, 4 × 25-Gbit/s, EADFB laser array module with large-output-power and low-driving-voltage for energy-efficient 100GbE transmitter," *Optics Express,* vol. 20, no. 1, pp. 614-620, 2012.

[16] "www.itu.int/home/," [Online].

[17] O. K. Kwon, Y. A. Leem, Y. T. Han, C. W. Lee, K. S. Kim and S. H. Oh, "A 10 × 10 Gb/s DFB laser diode array fabricated using a SAG technique," *Optics Express,* vol. 22, no. 8, pp. 9073-9080, 2014.

[18] T. Kurobe, T. Kimoto, K. Muranushi, T. Mukaihara, M. Ariga, N. Matsuo and A. Kasukawa, "Development of full-band tunable laser," *Furukawa Review,* vol. 33, pp. 1-5, 2008.

[19] H. Ishii, K. Kasaya and H. Oohashi, "Spectral linewidth reduction in widely wavelength tunable

DFB laser array," *IEEE Journal of Quantum Electronics,* vol. 15, no. 3, pp. 214-520, 2009.

[20] T. Kimoto, T. Kurobe, K. Muranushi, T. Mukaihara and A. Kasukawa, "Reduction of spectral-linewidth in high power SOA integrated wavelength selectable laser," *IEEE Journal of Selected Topics in Quantum Electronics,* vol. 11, no. 5, pp. 919-923, 2005.

[21] F. Bello, Q. Lu, A. Abdullaev, M. Nawrocka and J. F. Donegan, "Linewidth and noise characterization for a partially-slotted single mode laser," *IEEE Journal of Quantum Electronics,* vol. 50, no. 9, pp. 755-759, 2014.

[22] Y. Tohmori, Y. Yoshikuni, H. Ishii, F. Kano, T. Tamamura, Y. Kondo and M. Yamamoto, "Broadrange wavelength-tunable superstructure grating (SSG) DBR lasers," *IEEE Journal of Quantum Electronics ,* vol. 29, pp. 1817-1823, 1993.

[23] P. D. Maycock, "Thermal conductivity of silicon, germanium, III-V compounds and III-V alloys," *Solid-State Electronics,* vol. 10, pp. 161-168, 1967.

[24] L. A. Coldren and S. W. Corzine, Diode lasers and photonic integrated circuits, New-Yorl: John Wiley & Sons, Inc., 1995.

[25] K. Sato and M. Murakami, "Experimental investigation of thermal crosstalk in a distributed feedback laser array," *IEEE Photonic Tehcnology Letters,* vol. 3, no. 6, pp. 501-503, 1991.

[26] B. Klepser and H. Hillmer, "Investigations of thermal crosstalk in laser arrays for WDM applications," *Journal of Lightwave Technology,* vol. 16, no. 10, pp. 1888-1894, 1998.

[27] M. N. Sysak, D. Liang, R. Jones, G. Kurczveil, M. Piels, M. Fiorentino, R. G. Beausoleil and J. E. Bowers, "Hybrid silicon laser technology: a thermal perspective," *IEEE Journal of Selected Topics in Quantum Electronics,* vol. 17, no. 6, pp. 1490-1498, 2011.

[28] M. Peters, V. Rossin, M. Everett and E. Zucker, "High-power, high-efficiency laser diodes at JDSU," in *Proceedings SPIE 6456, High-Power Diode Laser Technology and Applications V,* San Jose, CA, 2007.

[29] D. Byrne, W. H. Guo, R. Phelan, Q. Lu, J. F. Donegan and B. Corbett, "Measurement of linewidth enhancement factor for InGaAlAs laser diode by Fourier series expansion method," *Electronics Letters,* vol. 43, no. 21, p. 1145, 2007.

[30] X. Liu, M. H. Hu, C. G. Caneau, R. Bhat and C. E. Zah, "Thermal management strategies for high power semiconductor pump lasers," *IEEE Transactions on components and packaging technologies,* vol. 29, no. 2, pp. 268-276, 2006.

[31] S. Murata, H. Nakada and T. Abe, "Theoretical and experimental evaluation of the effect of adding a heat-bypass structure to a laser diode array," *Japanese Journal of Applied Physics,* vol. 32, no. 3A, pp. 1112-1119, 1993.

[32] S. S. Saini, S. H. Cho and M. Dagenais, "Thermal considerations in high power semiconductor laser and semiconductor optical amplifiers," in *Proceedings SPIE 6478, Photonics Packaging, Integration, and Interconnects VII*, San Jose, CA, 2007.

Chapter 7 – Conclusion and outlook

7.1. Conclusion

A novel single-mode laser diode based on high order gratings (slots) suitable for monolithic integration has been presented. The laser platform exhibits simple fabrication process and operates with high SMSR and narrow linewidth making it suitable for coherent communications and WDM systems.

The single mode operation is achieved by etching distributed slots into the ridge of the laser diode. Therefore, there is no need to grow additional material as in case of DFB and DBR lasers. The slot parameters were optimized using the scattering matrix method. From the simulations the optimized slots parameters predicted a low threshold current and high SMSR. The first run of fabricated devices exhibit a threshold current of around 30 mA and a slope efficiency of 0.11 mW/mA. The SMSR was around 50 dB and the temperature tuning was over 4 nm in a 40°C of temperature change without mode hopping and high SMSR. However, the threshold current and the slope efficiency are lower than commercially available devices. To improve these parameters, AR and HR coatings were applied decreasing the threshold current to 19 mA and increasing the slope efficiency up to 0.17 mW/mA. But these values are still lower than, for instance, standard DFB lasers. The reason is the relatively high loss from the high order gratings (37^{th}). The high order gratings have advantages in terms of easy fabrication but with the sacrifice of slope efficiency and threshold current. In addition, some fabrication issues discussed in Chapter 5 were the reason of high loss. Further work will be in trying to reduce the losses from the slots and therefore design optimization is needed. In terms of fabrication tolerances, we believe that

by using a proper etching stop layer we can control the depth of the slots and probably it will improve the performance further.

We have demonstrated that these lasers can be monolithically integrated with other photonic components on the same chip. First, a laser was integrated with an SOA resulting in output power of more than 45 mW which is quite a high value. Next the laser was integrated with an EA modulator using an identical active layer (IAL) method where the laser and EA modulator have the same quantum well structure. For this design we changed the slot parameters and we introduced the concept of non-periodically spaced slots. In this design we used three different slot periods to suppress the undesirable side modes and shift the laser wavelength to the longer wavelength. From the experiments we obtained 20 nm of positive wavelength shift from the gain peak with SMSR more than 50 dB. An extinction ratio of 10 dB was achieved when the modulator was biased at -2.2 V. The extinction ratio is also lower than commercial devices and it should be improved in future.

The linewidth was measured using the delayed self-heterodyne method. The intrinsic linewidth has been measured to be around 2-4 MHz for short cavity lasers and it follows a 1/P trend. As was expected for longer lasers, the linewidth is lower. The linewidth remains the same with the temperature change but gets broader when the temperature is very high. This is due to increased heat generation and poor heat dissipation which leads to increased spontaneous emission. We also have checked how slot parameters will affect to the linewidth. Different slot widths were chosen to do this. Overall the 1/P trend was the same for all lasers but the linewidth varies between 1.5 and 3 MHz. However, we need to have a large set of lasers with different slot width and depth so we can obtain clear picture of the affect on linewidth.

In Chapter 6 we presented a tunable laser array based on slotted single mode lasers. We have developed two types of laser arrays. First was a 10-channel laser array with tuning range of around 31 nm. We have demonstrated that all channels exhibit single mode operation with SMSR more than 35 dB. All 10 lasers in the array have a threshold current between 19 and 21 mA. The linewidth remains around 2-4 MHz as for a single slotted laser. Then to increase the tuning range we presented a 12-channel laser array. For this array the tuning range covered the whole C-band and exceeded 35 nm. To increase the SMSR in the blue regions we introduced non-periodically spaced slots as we did for the slotted laser integrated with an EA modulator to suppress undesirable modes. As was expected, the

SMSR improved and remained around 50 dB for all channels. The linewidth of non-periodically spaced slotted laser array was the same as for the normal slotted laser array and measured to be around 2-4 MHz. We have measured 700 μm and 1000 μm lasers to see how the linewidth will improve. For 1000 μm lasers we achieved the linewidth below 500 kHz which is the main requirements in coherent communication systems.

The last characterization was the thermal characterization of slotted laser arrays. It has been found that the thermal crosstalk is a serious issue in our lasers. We have measured that the activated neighboring lasers will change the wavelength of operated laser. The closest located laser will change the wavelength of operating laser to more than 0.4 nm which corresponds to 4°C of temperature rise. The thermal impedance for all slotted lasers is uniform and around 75°C/W which is high value. This might be the main reason for poor heat dissipation in the system. Therefore, the material design should be optimized to improve thermal characteristics.

Overall, we presented slotted single mode lasers and slotted laser arrays with simple fabrication and potential to use standard photolithography which will reduce the cost and time. Hence, we believe that these lasers are potential candidates as a light source in coherent communication and WDM systems.

7.2. Outlook

The demonstrated 12-channel laser array almost meets the requirements for coherent optical communication systems. The next step in these lasers will be to integrate all lasers in the array with a multiplexer to send all channels into one fiber. For this purpose, a multi-mode interference (MMI) coupler may be used. The MMI couplers are very compact photonic components and can be easily designed. The schematic design of such structure is shown in Fig. 7.1. This was designed by our former post doc Dr. Qiaoyin Lu.

The structure in Fig. 7.1 consists of three parts: a slotted laser array part, a coupler part with passive waveguides and MMI coupler to combine all wavelengths, and a curved semiconductor optical amplifier (SOA) section.

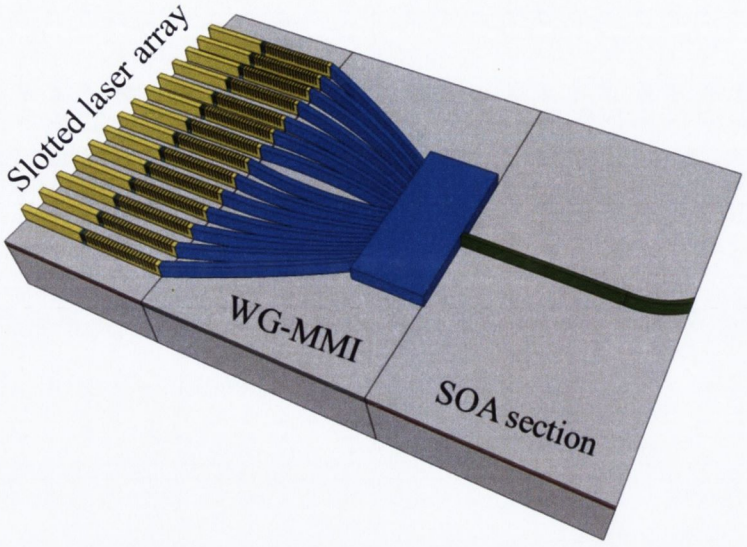

Fig. 7.1 Schematic structure of 12-channel laser array integrated with multi-mode interference coupler (MMI).